

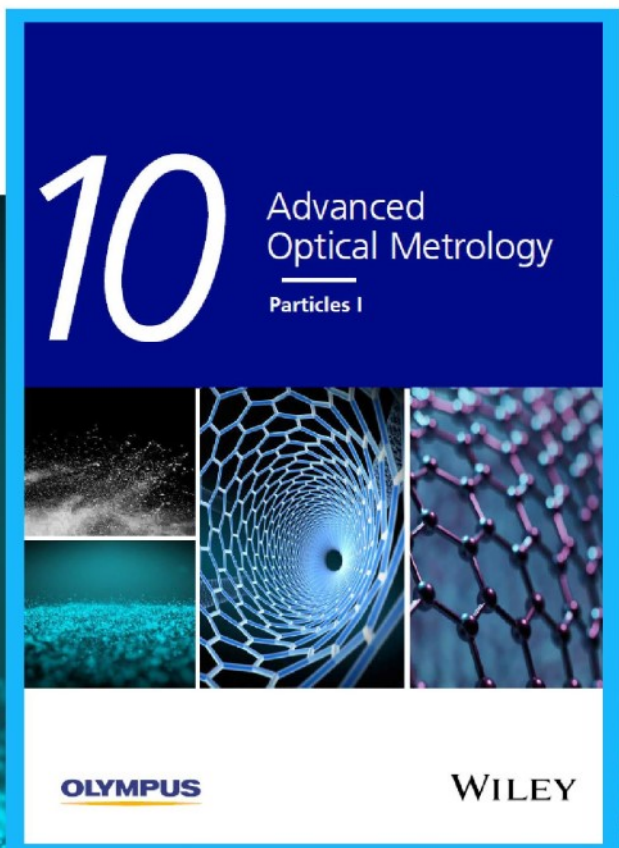


# Particles I

Access the latest eBook →

Particles: Unique Properties,  
Uncountable Applications

**Read the latest eBook and  
better your knowledge with  
highlights from the recent  
studies on the design and  
characterization of micro-  
and nanoparticles for  
different application areas.**



**Access Now**

This eBook is sponsored by

**OLYMPUS**

**WILEY**

# Insights on Flexible Zinc-Ion Batteries from Lab Research to Commercialization

Haobo Dong, Jianwei Li, Jian Guo, Feili Lai, Fangjia Zhao, Yiding Jiao, Dan J. L. Brett, Tianxi Liu, Guanjie He,\* and Ivan P. Parkin\*

Owing to the development of aqueous rechargeable zinc-ion batteries (ZIBs), flexible ZIBs are deemed as potential candidates to power wearable electronics. ZIBs with solid-state polymer electrolytes can not only maintain additional load-bearing properties, but exhibit enhanced electrochemical properties by preventing dendrite formation and inhibiting cathode dissolution. Substantial efforts have been applied to polymer electrolytes by developing solid polymer electrolytes, hydrogel polymer electrolytes, and hybrid polymer electrolytes; however, the research of polymer electrolytes for ZIBs is still immature. Herein, the recent progress in polymer electrolytes is summarized by category for flexible ZIBs, especially hydrogel electrolytes, including their synthesis and characterization. Aiming to provide an insight from lab research to commercialization, the relevant challenges, device configurations, and life cycle analysis are consolidated. As flexible batteries, the majority of polymer electrolytes exploited so far only emphasizes the electrochemical performance but the mechanical behavior and interactions with the electrode materials have hardly been considered. Hence, strategies of combining softness and strength and the integration with electrodes are discussed for flexible ZIBs. A ranking index, combining both electrochemical and mechanical properties, is introduced. Future research directions are also covered to guide research toward the commercialization of flexible ZIBs.

fields such as healthcare, automotive, and aviation. Among them, flexible and wearable electronics exhibit a growing interest such as implantable medical devices,<sup>[1]</sup> wearable health monitoring systems,<sup>[1,2]</sup> flexible displays,<sup>[3]</sup> and smart clothes.<sup>[4]</sup> Conventional devices utilizing rigid and relatively unsafe lithium-ion batteries (LIBs) as the power supply cannot satisfy the future requirements of biocompatible and flexible features. Moreover, the bottleneck of flexible LIBs, such as the high cost, safety issues and intricate manufacturing requirements restrict the commercialization of flexible LIBs. As promising alternatives, aqueous zinc-ion batteries (AZIBs) have attracted a significant attention. They are regarded as competitive candidates for flexible devices owing to the high volumetric capacity (5855 mAh cm<sup>-3</sup>) of the zinc metal and its facile fabrication process. Meanwhile, the superior cost advantage, \$25/kWh<sup>[5]</sup> for AZIBs comparing to \$135/kWh<sup>[6,7]</sup> for LIBs, is beneficial to applying AZIBs in different scales of devices.

Aqueous zinc ion batteries (AZIBs) currently suffer from unfavorable water-induced side reactions that result in zinc dendrite formation, dissolution of cathode materials and the formation of byproducts on cathodes, thus causing a fast capacity fade. Owing to the water electrolysis (stable

## 1. Introduction

With the growth in big data, there is an increasing demand in electronic devices for capturing real-time data in various

H. Dong, Dr. J. Li, Dr. J. Guo, F. Zhao, Y. Jiao, Dr. G. He, Prof. I. P. Parkin  
Christopher Ingold Laboratory  
Department of Chemistry  
University College London  
20 Gordon, London WC1H 0AJ, UK  
E-mail: g.he@ucl.ac.uk; i.p.parkin@ucl.ac.uk

Dr. F. Lai  
Department of Chemistry  
KU Leuven Celestijnenlaan 200F, Leuven 3001, Belgium

 The ORCID identification number(s) for the author(s) of this article can be found under <https://doi.org/10.1002/adma.202007548>.

© 2021 The Authors. Advanced Materials published by Wiley-VCH GmbH. This is an open access article under the terms of the Creative Commons Attribution License, which permits use, distribution and reproduction in any medium, provided the original work is properly cited.

DOI: 10.1002/adma.202007548

Prof. D. J. L. Brett, Dr. G. He  
Electrochemical Innovation Lab  
Department of Chemical Engineering  
University College London  
20 Gordon Street, London WC1H 0AJ, UK

Prof. D. J. L. Brett  
The Faraday Institution  
Quad One  
Becquerel Avenue, Harwell Campus, London OX11 0RA, UK

Prof. T. Liu  
School of Chemical and Material Engineering  
Jiangnan University  
No. 1800, Lihu Avenue, Wuxi 214122, China

Dr. G. He  
School of Chemistry  
University of Lincoln  
Brayford Pool, Lincoln LN6 7TS, UK

potential window of water is 1.23 V) as shown in the following equation, the operational potential is restricted to achieve a wide range.



Polymer/hydrogel electrolytes such as poly(vinyl alcohol) (PVA) and polyacrylamide (PAM) are essential for solving these issues due to the reduced water content contained in the electrolyte. Introducing the solid–solid interface between electrodes and the electrolyte instead of the solid–liquid interface can suppress the growth of zinc dendrites and the dissolution of cathode materials. Meanwhile, the stable solid–solid interface also improves the electrochemical stability by reducing water-induced side reactions at the interface during charge and discharge processes. Besides, due to the characteristics of the polymer/hydrogel electrolyte, polymer ZIBs exhibit additional functionalities such as self-healing, elasticity, anti-freezing and thermal-response properties. Although there has recently been tremendous development in polymer/hydrogel electrolytes for ZIBs, there are still several challenges facing state-of-the-art polymer electrolytes, which can be summarized as follows:

1. Ionic conductivities for polymer/hydrogel electrolytes are in the range of  $10^{-4}$  to  $10^{-1}$  S  $\text{cm}^{-1}$ , which is lower than that of the AZIBs ( $\approx 1$  S  $\text{cm}^{-1}$ ).
2. Aging effects of polymer/hydrogel electrolytes hinder use in practical applications.
3. The mechanism for charge storage at the solid–solid interface is unclear, which restricts the design and optimization of the polymer electrolyte.

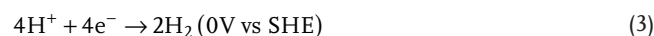
Until now, the research of polymer electrolytes for flexible ZIBs is still in its infancy. where the in-depth understanding of polymer/hydrogel electrolytes on the electrochemical performance is still absent. Niu<sup>[8]</sup> and co-workers<sup>[9,10]</sup> have summarized the mechanisms in AZIBs in detail, while Xia et al.<sup>[11]</sup> have reviewed the mechanism and challenges with a specific focus on polymer electrolytes for ZIBs which provided an overview of the research progress. Different from previous reviews, in this work, a specific view from lab-based research to commercialization is mainly provided. Apart from the summary of operating mechanisms, cathode materials and recent progress in polymer electrolytes according to categories of pristine hydrogel electrolytes (HPEs), solid polymer electrolytes (SPEs) and hybrid polymer electrolytes (HBPEs), device fabrication strategies and life-cycle assessments are covered in this review. Especially for hydrogel electrolytes, electrolytes are systematically categorized into natural biomass hydrogel, synthetic porous hydrogels and oxide hydrogels. There is a detail clustering for biomass hydrogels, which contains polysaccharides gels and protein-based gels. Moreover, a new ranking index is introduced as the determination parameter indicating the feasibility to commercialization on account of mechanical and electrochemical properties. With a discussion of application scenarios for flexible ZIBs, future research directions and optimization strategies are proposed at the end of the review accordingly.

## 2. Energy Storage Mechanism of AZIBs

AZIBs are “rocking chair” batteries which require a reversible transmission of  $\text{Zn}^{2+}$  ions between cathodes and anodes. Typically, zinc stripping/plating happens on the anode with a standard hydrogen electrode (SHE) potential of  $-0.76$  V, where anodic zinc oxidized to  $\text{Zn}^{2+}$  ions strip from the anode to the electrolyte during the discharge process, while  $\text{Zn}^{2+}$  ions from the electrolyte reduced to Zn plate on the anode during the charging process. However, the uneven electrodeposition of the zinc on the anode induces the formation of zinc dendrites that finally caused a short circuit and a low Coulombic efficiency. As shown in the Pourbaix diagram for zinc (Figure 1a), potentials for the hydrogen evolution reaction (HER) and oxygen evolution reaction (OER) are pH-dependent, which dictates the stable potential window for AZIBs. There are few reduced zinc byproducts in alkaline solution, whereas for acidic solution  $\text{Zn}^{2+}$  ions are the major charge carrier. In mild acid aqueous electrolyte, the OER is likely to occur on the cathode:



while the HER occurs on the zinc anode:



Therefore, to initiate a reversible intercalation/de-intercalation process of  $\text{Zn}^{2+}$  ions, the suitable potential window should be determined to avoid HER and OER for various cathode materials. Until now, various types of cathode materials reported can be classified into five groups consisting of: manganese-based oxides (Mn-based); vanadium-based oxides (V-based); Prussian blue analogues (PBAs); organic materials and other active materials such as  $\text{VSe}_2$ <sup>[15]</sup> and  $\text{Zn}_{0.4}\text{VOPO}_4$ .<sup>[16]</sup> For inorganic cathode materials especially the water-soluble PBAs, structural transformation and the disproportionation reaction upon cycling cause the issues of active material dissolution, which can have a great impact on the capacity decay. Although the energy storage mechanism for AZIBs is elusive, a common agreement for the  $\text{Zn}^{2+}$  storage in cathode materials is as shown in Figure 1b–d and can be briefly summarized as i)  $\text{Zn}^{2+}$  intercalation/deintercalation, ii)  $\text{Zn}^{2+}$  and  $\text{H}^+$  co-insertion, iii) chemical conversion reaction, and iv) coordination/incoordination reaction.

### i. $\text{Zn}^{2+}$ intercalation/deintercalation

Zinc insertion/extraction, the principal mechanism, was firstly reported by Kang et al.,<sup>[17]</sup> where  $\text{ZnMn}_2\text{O}_4$  was detected at the discharge state for tunnel-type  $\alpha$ - $\text{MnO}_2$ . Further study convinced that  $\text{Zn}^{2+}$  ions intercalate and deintercalate into all layered and tunnel frameworks, for all Mn-based materials used:  $\beta$ - $\text{MnO}_2$ ,<sup>[18]</sup>  $\delta$ - $\text{MnO}_2$ ,<sup>[18]</sup>  $\text{Na}_{0.95}\text{MnO}_2$ ,<sup>[19]</sup>  $\text{MgMn}_2\text{O}_4$ ,<sup>[20]</sup>  $\text{ZnMn}_2\text{O}_4$ ,<sup>[21]</sup> V-based materials:  $\text{V}_2\text{O}_5$ ,<sup>[12,22]</sup>  $\text{Zn}_{0.3}\text{V}_2\text{O}_5$ ,<sup>[23]</sup>  $\text{Ni}_{0.25}\text{V}_2\text{O}_5$ ,<sup>[24]</sup>  $\text{NaV}_3\text{O}_8$ ,<sup>[25]</sup> or PBAs:  $\text{ZnHCF}$ ,<sup>[26,27]</sup>  $\text{CuHCF}$ ,<sup>[28]</sup> and  $\text{CoFe}(\text{CN})_6$ .<sup>[13]</sup>

### ii. $\text{Zn}^{2+}$ and $\text{H}^+$ co-insertion

Besides  $\text{Zn}^{2+}$  insertion,  $\text{H}^+$  insertion verified by discharge galvanostatic intermittent titration technique (GITT) of  $\alpha$ - $\text{MnO}_2$ <sup>[29]</sup> happens before  $\text{Zn}^{2+}$  insertion, in which  $\text{H}^+$  intercalates into the cathode material at a low voltage plateau

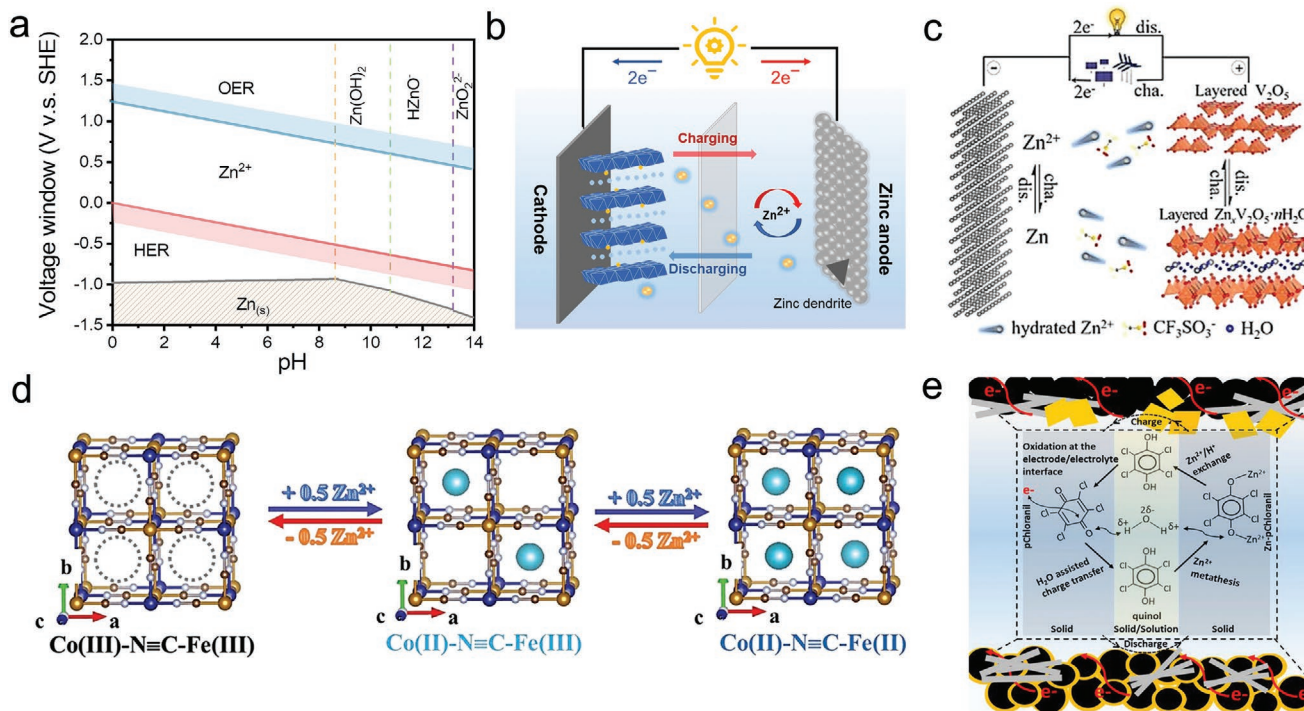


**Figure 1.** a) The Pourbaix diagram of Zn anodes in aqueous solution. b) Schematic of the  $\text{Zn}^{2+}$  insertion/extraction mechanism for the Zn/ $\delta\text{-MnO}_2$  battery. c) Schematics of the  $\text{Zn}^{2+}$  insertion/extraction mechanism for a Zn/ $\text{V}_2\text{O}_5$  battery. d) Illustration of  $\text{Zn}^{2+}$  intercalation/deintercalation mechanism for a Prussian blue analogue material  $\text{CoFe}(\text{CN})_6$ . e) Schematics of water-assisted phase transfer mechanism of  $\text{Zn}^{2+}/\text{H}^+$  storage in an organic cathode material p-chloranil. c) Reproduced with permission.<sup>[12]</sup> Copyright 2018, American Chemical Society. d) Reproduced with permission.<sup>[13]</sup> Copyright 2019, Wiley-VCH. e) Reproduced with permission.<sup>[14]</sup> Copyright 2018, American Chemical Society.

(0.08 V) compared to a greater voltage (0.6 V) for  $\text{Zn}^{2+}$ . Owing to the small radius of  $\text{H}^+$  and weak electrostatic interactions to the host materials,  $\text{H}^+$  insertion is faster than  $\text{Zn}^{2+}$  insertion. Similarly, co-insertion of  $\text{Zn}^{2+}$  and  $\text{H}^+$  was also elucidated for vanadium oxide,  $\text{NaV}_3\text{O}_8 \cdot 1.5\text{H}_2\text{O}$ .<sup>[25]</sup> We have also detected proton and zinc ion co-intercalation for  $\delta\text{-Ni}_{0.25}\text{V}_2\text{O}_5$ , while  $\text{Zn}^{2+}$  intercalation mechanism is the main domination.<sup>[24]</sup> However,  $\text{Zn}^{2+}$  and  $\text{H}^+$  co-insertion are not unique for V-based materials, we also observed the co-insertion for manganese oxides,  $\text{K}_{0.28}\text{MnO}_2$ .<sup>[30]</sup>  $\text{Zn}^{2+}$  and  $\text{H}_2\text{O}$  co-insertion was also identified for  $\text{V}_2\text{O}_5$ <sup>[12]</sup> and  $\text{H}_2\text{V}_3\text{O}_8$ <sup>[31]</sup> cathodes, where hydrated  $\text{Zn}^{2+}$  intercalate into the layer crystalline structure expanding the interlayer space. Hu et al.<sup>[32]</sup> also revealed  $\text{Zn}^{2+}$  and  $\text{H}^+$  co-intercalations for spinel oxide nanodots  $\text{Mn}_3\text{O}_4$ .

### iii. Chemical conversion reaction

For Mn-based cathode materials, the chemical conversion of  $\alpha\text{-MnO}_2$  to  $\text{MnOOH}$  in  $\text{ZnSO}_4$  solution was detected,<sup>[33]</sup> for which  $\text{MnO}_2$  reacts with  $\text{H}^+$  to generate  $\text{MnOOH}$ , changing the average valence states from +4 to +3 during the discharge process.

### iv. Coordination/incoordination reaction

The coordination/incoordination reaction is the mechanism to store  $\text{Zn}^{2+}$  for organic cathode materials such as quinone-based compounds calix[4]quinone,<sup>[34]</sup> pyrene-4,5,9,10-tetraone (PTO) and p-chloranil.<sup>[14]</sup> As shown in Figure 1d, electronegative oxygen atoms on the organic compounds are employed as active sites storing  $\text{Zn}^{2+}$  via the coordination reaction.

Until now, most of the zinc salts used in electrolytes are sulfates and sulfonates. Especially for sulfates, byproducts such as

$\text{ZnSO}_4[\text{Zn}(\text{OH})_2]_3 \cdot x\text{H}_2\text{O}$  are likely to form; the pros and cons of these byproducts are still under debate. Acetate-based salts have been investigated recently showing a two-electron redox mechanism<sup>[35]</sup> for Mn-based cathode instead of a single-electron transmission, where the Mn deposition/dissolution mechanism was attained delivering a superior capacity with  $556 \text{ mAh g}^{-1}$ . The mechanisms and challenges faced for ZIBs are still under investigation. The alleviation of side reactions, such as the zinc dendrite formation and the cathode dissolution, additives in electrolyte,<sup>[36]</sup> water-in-salt solutions,<sup>[37]</sup> polymer electrolytes,<sup>[38]</sup> and electrode coating<sup>[39]</sup> methods have been explored. Although the strategies to avoid current issues for AZIBs are still facing challenges, polymer electrolytes applied into ZIBs are not only essential to tackle these barriers but also to exhibit additional mechanical properties.

## 3. Recent Progress of Polymer Electrolyte for ZIBs

Before the foundation of mild acid Zn/ $\text{MnO}_2$  batteries,<sup>[56]</sup> polymer electrolytes for acidic ZIBs have been developed for nearly two decades, as shown in Figure 2a; however, tremendous breakthroughs are owed to the exploitation of AZIBs by Kang and co-workers in 2012.<sup>[17,18,57]</sup> Similar to the development of LIBs, organic solid polymers were pioneering to be utilized in ZIBs as the electrolyte host materials such as poly(ethylene oxide) (PEO),<sup>[54]</sup> poly(vinylidene fluoride) (PVDF),<sup>[52]</sup> and polyacrylonitrile (PAN),<sup>[58]</sup> exhibiting ionic conductivities in the

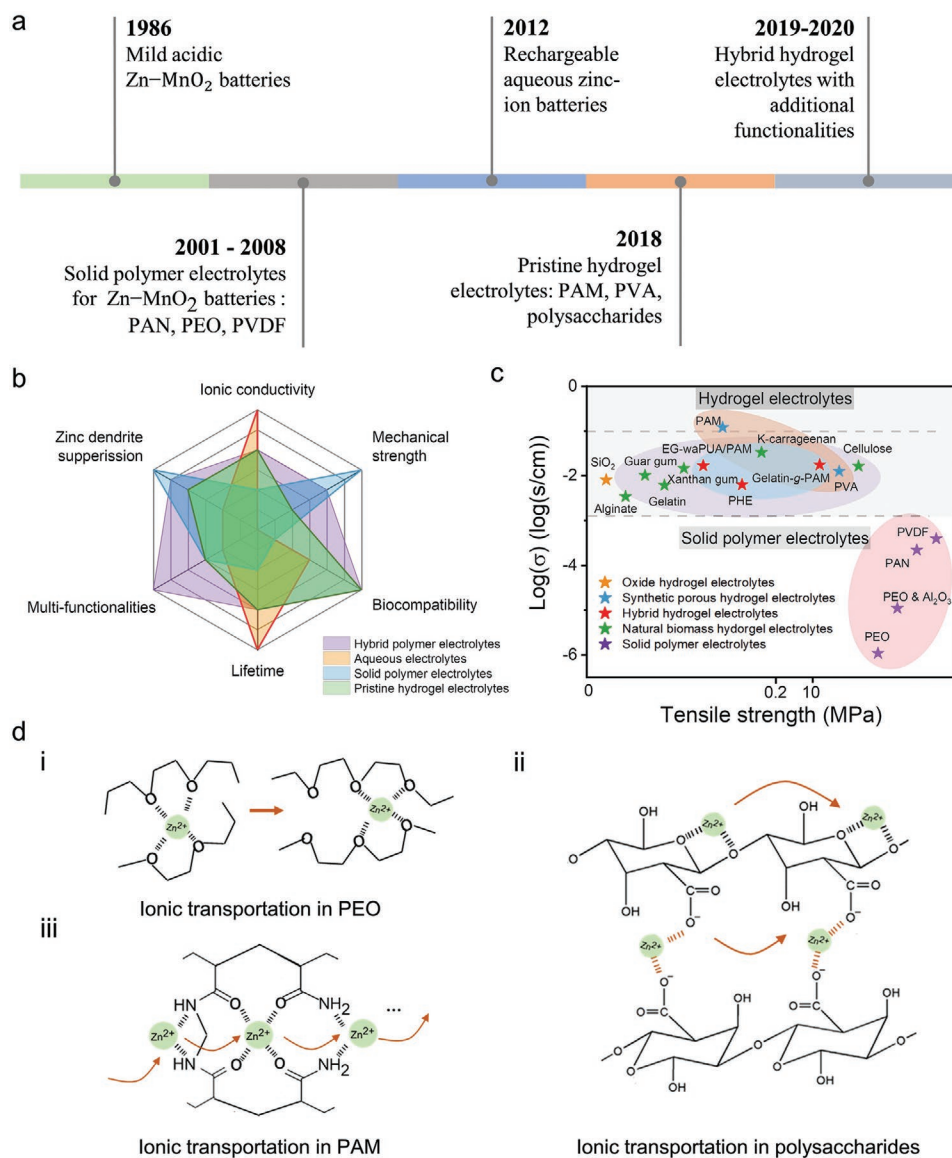


**Figure 2.** a) The development history of polymer electrolytes for RZIBs. b) A radar diagram of multi-angle comparison of aqueous electrolytes, solid polymer electrolytes, pristine hydrogel electrolytes and hybrid electrolytes. c) Summary of the recently reported polymer electrolytes in relation to empirical magnitude of tensile strength. (Fumed silica,<sup>[40]</sup> PVA,<sup>[41]</sup> PAM,<sup>[42]</sup> Gelatin-g-PAM,<sup>[38]</sup> EG-waPUA/PAM,<sup>[43]</sup> PHE,<sup>[44]</sup> PNA,<sup>[45]</sup> gelatin,<sup>[46]</sup> xanthan gum,<sup>[47]</sup> guar gum,<sup>[48]</sup> alginate,<sup>[49]</sup> cellulose,<sup>[50]</sup> κ-carrageenan,<sup>[51]</sup> PVDF,<sup>[52]</sup> PAN,<sup>[53]</sup> PEO,<sup>[54]</sup> PEO&Al<sub>2</sub>O<sub>3</sub><sup>[55]</sup>). d) Schematic diagrams of the ionic transportation in: i) solid polymer electrolyte, ii) polysaccharides hydrogels, and iii) PAM hydrogel electrolytes.

range of  $10^{-6}$  to  $10^{-4}$  S  $\text{cm}^{-1}$  (Figure 2c). Afterward, by introducing hydrogel as the host, hydrogel electrolytes such as polysaccharides and polyacrylamide (PAM) based polymer electrolytes exhibit high ionic conductivity from  $10^{-3}$  to  $10^{-1}$  S  $\text{cm}^{-1}$ . Until now, polymer electrolytes for ZIBs can be classified into three categories: solid polymer electrolytes (SPEs), pristine hydrogel electrolytes (HPEs) and hybrid polymer electrolytes (HBPEs). Owing to side effects from the water content described in the previous section, there is a common agreement that the classification standard of polymer electrolytes for ZIBs are determined by the presence of the water content in polymer electrolytes. Compared to aqueous electrolytes, polymer electrolytes are beneficial to avoid zinc dendrite formation and alleviate cathode dissolution. The additional functionalities of

the polymers eliminate the parasite weight occupation from the separator and enhance the mechanical performance. As demonstrated in the radar diagram (Figure 2b), SPEs possess superior mechanical strength compared to HPEs, whereas hydrogel electrolytes favor a competitive ionic conductivity compared to aqueous electrolytes. Regarding zinc dendrite formation, solid polymer electrolyte is expected to exhibit the greatest zinc dendrite inhibition because of its stable structure, whereas owing to the water content in the hydrogel, hydrogel electrolytes exhibit a lower ability to prevent dendrite formation. By integrating both advantages, HBPEs providing the best compromise among these perspectives are essential for further commercialization which not only delivers high ionic conductivities but also exhibits competitive multifunctionalities

and mechanical behaviors. As shown in Figure 2c, a clustering model on the basis of ionic conductivity and tensile strength clearly elucidates the differences for reported polymer electrolytes. Polymer electrolytes reported are separated into two parts: solid polymer electrolytes and hydrogel electrolytes, where a comprehensive clustering is provided for hydrogel electrolytes. Natural biomass hydrogel electrolytes are those obtained naturally from plants and animals, such as polysaccharides and protein-based gels, while synthetic porous hydrogel electrolytes are referred to polyelectrolytes developed based on acrylamide and vinyl acetate containing porous structures. For oxide hydrogels, although there are only silica gels utilized into ZIBs so far, other oxide hydrogels such as metal oxides reviewed in the following section could also be the potential hydrogel electrolytes. Due to the fact that only a few polymer electrolytes have been tested in tensile experiments, most tensile strengths in this model are empirical values. It is expected that further experimental standard for polymer electrolytes could be devoted to requiring the mechanical property evaluation alongside with the electrochemical tests.

Regarding the ionic transportation mechanism in polymer electrolytes, there is a common agreement that  $Zn^{2+}$  ions transmit to the neighboring site of free electron donors by segmental motions, similar to the studies of polymer electrolytes for LIBs. There has been the extensive study of ionic transportation mechanisms in polymer electrolytes in lithium-ion batteries, where there is a common agreement that  $Li^+$  ions transmit to the neighboring site of free electron donors by segmental motions. Most of the polymer electrolytes are semi-crystalline polymers consisting of crystalline and amorphous phases. Goodenough et al.<sup>[59]</sup> have revealed that the existence of a high crystalline fraction prevented the movement of small chain segments in poly(ethylene oxide) (PEO) polymers and that the ion conduction mainly occurred in the amorphous region. Hence the polymers with low glassy transition temperature ( $T_g$ ), exhibiting more amorphous regions, are proposed to be suitable hosts as polymer electrolytes. Meyer<sup>[60]</sup> and Smith<sup>[61]</sup> have investigated the  $Li^+$  transportation mechanism in PEO polymer electrolyte by molecular dynamics simulations.  $Li^+$  ions are complexed to PEO chains via coordination bonding through oxygen polar sites. The mobility of  $Li^+$  ions is related to the motion of the segments of the PEO chain where the free volume in the amorphous region induces the segmental chain rotation and hence enables the  $Li^+$  ions to hop from one coordination site to another. However, Tunstall et al. reported that the ionic conductivity in static, ordered environments of the crystalline phase can be greater than that in the equivalent amorphous material above  $T_g$ ,<sup>[62]</sup> while the opposite results revealed by Henderson et al.<sup>[63]</sup> contradicted with the ion transportation in the crystalline phase. Although there is still a debate, segmental motion is the common agreement so far and the ionic conductivity follows two dominant conduction mechanisms: the Vogel–Tamman–Fulcher (VTF) type and the Arrhenius type.<sup>[64–66]</sup> Therefore, ionic conduction in polymer electrolyte can be summarized as follows: cations in the polymer complexes are located at coordination sites (e.g.,  $-O-$  for PEO, and  $-CN$  for PAN). The amorphous region provides the free volume for local segmental motion where the cations migrate from one site to the neighboring site under the effect

of an electric field.<sup>[67]</sup> Similarly, for zinc-ion batteries,  $Zn^{2+}$  ions are also believed to transmit via the segmental motion in the polymer electrolytes. Figure 2d-i–iii show schematic diagrams illustrating ionic transportation in SPEs, HPEs and HBPEs respectively. For SPEs such as PEO and PVA, which consist of  $-O-$  and  $-OH$  chains displayed in Figure 2d-i,  $Zn^{2+}$  ions are likely to form coordinate bonding with  $-O-$  polar sites in the polymer complexes. Under an electric field,  $Zn^{2+}$  ions hop from one site to another during the charge/discharge process. Similarly, for biomass hydrogels,  $Zn^{2+}$  ions will form coordinate interactions to the  $C-O-C$  and  $COO^-$  groups by ionic dipole interaction and coulombic attraction force respectively<sup>[68]</sup> followed by the interchain hopping mechanism owing to segmental motion (Figure 2d-ii). While for hydrogel synthesized with PAM (Figure 2d-iii),  $Zn^{2+}$  ions are possible complexing of metal ions at the carbonyl oxygen and nitrogen in  $C=O$  and  $-NH_2$  respectively.<sup>[69,70]</sup> HBPEs are supposed to work using all these possible pathways. However, there is still a lack of exploitation in ionic transportation mechanism for polymer electrolytes in zinc-ion batteries, especially for HBPEs where there is merely no detailed study.

#### 4. Solid Polymer Electrolytes

Inspired by the solid polymer electrolyte developed for LIBs, polymer electrolytes for ZIBs are synthesized by dissolving zinc salts into polymer frameworks, such as PEO, PAN and PVDF forming the polymer-salt complexes. Regarding energy storage mechanism, SPEs for ZIBs are in the same mechanism as LIBs by which  $Zn^{2+}$  is stored in the framework with the free donor of the oxygen atoms and transferred through the polymer electrolytes by segmental motion.<sup>[62,71]</sup> Pucic et al.<sup>[54]</sup> have investigated the variation of ionic conductivity with temperature for PEO- $ZnCl_2$  complexes showing that ionic conductivities of SPEs are temperature sensitive and exhibit a high ionic conductivity of  $10^{-3} S cm^{-1}$  at 100 °C, whereas only  $10^{-6} S cm^{-1}$  at standard conditions. Changing the zinc salt from  $ZnCl_2$  to  $Zn(CF_3SO_3)_2$  and  $ZnBr_2$ ,<sup>[72]</sup> ionic conductivities are still in the same magnitude of  $10^{-6} S cm^{-1}$  at room temperature. The extreme utilization conditions are not robust for general application scenarios and also increase the risk of explosion. Hence, to further improve the ionic conductivity, additives such as propylene carbonate (PC) and  $Al_2O_3$  have been applied as plasticizers and nanofillers respectively to expand the free volume for  $Zn^{2+}$  segmental motion in polymer electrolytes. Although the ionic conductivities for SPEs are less than HPEs, water molecules in the hydrogel are likely to induce side reactions such as the HER and dendrite growth. Therefore, SPEs have returned to the focus of the research agenda. Apart from conventional SPEs consisting of zinc salts and additives, ionic liquids were utilized in ZIBs. Zhi et al.<sup>[73]</sup> have developed a hydrogen-free and dendrite-free SPEs by dissolving 1-ethyl-3-methyl-imidazolium tetrafluoroborate ([EMIM]BF<sub>4</sub>) ionic liquid with a supporting zinc salt, 2 M zinc tetrafluoroborate ( $Zn(BF_4)_2$ ) into the polymer host PVDF. The polymer film exhibits a high ionic conductivity of  $16.9 \times 10^{-3} S cm^{-1}$  which also prevents dendrite and HER reactions. We also observed the smooth morphology of the zinc anode after cycling for solid polymer ZIBs.<sup>[74]</sup>

## 5. Hydrogel Polymer Electrolyte

HPEs can be categorized into three clusters: natural biomass gel electrolytes; synthetic porous hydrogel electrolytes such as PAM and PVA, and oxide hydrogel electrolytes. Compared to solid polymer electrolytes, the features of water absorption for HPEs exploits the superiority of rechargeable AZIBs, exhibiting a high ionic conductivity in the range from  $10^{-3}$  to  $10^{-1}$  S  $\text{cm}^{-1}$ . However, because of the presence of water molecules in the hydrogel frameworks, undesirable byproducts such as  $\text{Zn}(\text{OH})_2$  and  $\text{ZnO}$  and the HER side reaction will significantly reduce the stability of ZIBs. This section consists of a comprehensive review for hydrogel electrolytes, and the effects of the water content of the electrolytes are discussed in Sections 9.3 and 9.4 regarding the interfacial interactions.

### 5.1. Natural Biomass Hydrogel Electrolytes

Most of the natural biomass gels are polysaccharides produced commercially from plants, animals and micro-organisms. Polysaccharides and protein gelation may be pursued by a variety of routes, but generally, gel networks are mostly formed together by electrostatic, hydrogen bonding, hydrophilic, van der Waals interactions, or a combination thereof with the hydrophilic groups in the chain structure such as  $-\text{OH}$ ,  $-\text{COO}$ ,  $-\text{NH}_4$ ,  $-\text{CO}-\text{NH}-$ , and peptide bonds.<sup>[75,76]</sup>

#### 5.1.1. Polysaccharide Gel Electrolytes

Polysaccharide gels, often utilized as food thickening agents,<sup>[72]</sup> have advantages in ZIBs owing to their high water affinity. Meanwhile, excellent biocompatibility is beneficial for skin and implantable electronics. Most polysaccharides, such as gum, carrageen, starch and cellulose, are under the process of temperature-induced gelation with aqueous solutions, for which the hydrogel formed are often thermoreversible. Zhang<sup>[47]</sup> and Huang<sup>[48]</sup> who have investigated xanthan gum and guar gum respectively revealed the feasibility using gum as the host for electrolytes. Xanthan gum, firstly exploited in the 1950s,<sup>[77]</sup> is a branched polysaccharide derived from bacterial fermentation: *Xanthomonas campestris*. As demonstrated in **Table 1**, xanthan gum consists of a cellulose backbone accompanying with a trisaccharide group composed of mannose ( $\beta$ -1,4), glucuronic acid ( $\beta$ -1,2), and mannose attached to  $\text{D}$ -glucosyl residues.<sup>[77]</sup> Gelation for xanthan hydrogel will be induced by heating the aqueous solution at  $40^\circ\text{C}$ ,<sup>[78]</sup> where water molecules are attracted by hydroxyl groups during the annealing process. Apart from temperature-induced gelation, xanthan gum is also able to form physical networks with bivalent metal ions.  $\text{Zn}^{2+}$  ions in the aqueous solution could form the intramolecular crosslinking by electrostatic interaction with two disaccharide units and O-acetyl and pyruvyl residues at side chains once the stoichiometric equivalence reaches above 100%.<sup>[79]</sup> Xanthan gum electrolyte<sup>[47]</sup> synthesized with 3 M  $\text{ZnSO}_4$  and 0.1 M  $\text{MnSO}_4$ , exhibits a porous structure (**Figure 3a-i**) with high ionic conductivity of  $1.46 \times 10^{-2}$  S  $\text{cm}^{-1}$ . Different from agar, PEO and PVA, xanthan gum exhibits superior compatibility

with sulfate salts with no precipitation. The quasi solid-state electrolyte was assembled with Zn and  $\text{MnO}_2$  delivering a specific capacity of 260 mAh  $\text{g}^{-1}$  at 1 C as shown in **Figure 3a-ii**. Meanwhile, the comparison of SEM images (**Figure 3a-iii**) for the zinc anode after cycling shows the suppression of zinc dendrites by the xanthan gum owing to the slow mass diffusion on the cathode. Similar to xanthan gum, guar gum extracted from guar beans forms a gel with bivalent cations over the pH range of 5–7. Strong acids or alkalis may result in the hydrolysis of the polysaccharides, thus reducing the viscosity. As investigated by Huang et al.,<sup>[48]</sup> although the structure of the guar gum electrolyte is not porous because of the linear chain backbone of  $\beta$ 1,4-linked mannose residues (**Figure 3b-i**), the ionic conductivity is still high and reaches  $1.07 \times 10^{-2}$  S  $\text{cm}^{-1}$ . Meanwhile, the gum electrolyte also exhibits a promising galvanic charge/discharge performance (**Figure 3b-ii**), superior flexibility and anti-flammability. Moreover, Huang et al.<sup>[51]</sup> have developed a kappa-carrageenan based electrolyte, kappa-carrageenan, exhibiting an ionic conductivity in the same magnitude of  $3.32 \times 10^{-2}$  S  $\text{cm}^{-1}$ . Kappa-carrageenan is a cation-selective binding polymer consisting of a linear backbone attached with  $\beta$ -D-galactopyranosyl 4-sulfate and O-4-linked 3,6-anhydro-D-galactopyranosyl residues. Helical gels could form in the presence of cations, such as  $\text{K}^+$ ,  $\text{NH}_4^+$ , in an aqueous solution. However, as shown in **Figure 3b,e-h**, both gum and carrageenan electrolytes suffer from capacity fading, which is approximate 10% after 300 cycles. Similar to the “water-in-salt” strategy to increase the cycling stability, the further investigation was devoted to analyzing the effect of swollen water content to the cycling stability.

Celluloses, such as carboxymethyl cellulose sodium (CMC) and carboxymethyl starch sodium (CMS) are common polysaccharides used as cathode binders providing robustness in mechanical properties.<sup>[80–82]</sup> Zhang et al.<sup>[83]</sup> have synthesized a CMC hydrogel electrolyte coupling with Zn nanosheet array on carbon nanotube fibers (CNTF) and zinc hexacyanoferrate ( $\text{ZnHCF}$ ) composited on a CNT sheet (**Figure 4a**). The extraordinary cable-based flexible battery delivered a high energy density of 195.39 mWh  $\text{cm}^{-3}$  with an outstanding capacity retention of 93.2% after bending 3000 times. Na et al.<sup>[50]</sup> have also developed a cellulose hydrogel ZIBs exhibiting an energy density of 1175 mWh  $\text{g}^{-1}$  as shown in **Figure 4b**, where the cellulose paper is not only used as the separator swelling the electrolyte but used as the cathode host. Absorbing 2 M  $\text{ZnCl}_2$  and 3 M  $\text{NH}_4\text{Cl}$  aqueous solution, the hydrogel electrolyte is able to reach an ionic conductivity of  $1.64 \times 10^{-2}$  S  $\text{cm}^{-1}$ . The as-fabricated battery also maintains superior flexibility where the specific capacity is merely influenced during the bending state (**Figure 4b-iii**).

Starch, the largest source of carbohydrates in the human diet, is a common polysaccharide consisting of linear amylose and a highly branched amylopectin. Gelation happens when starch complexes are heated to the gelation temperature, typically  $80^\circ\text{C}$ . Wang et al.<sup>[84]</sup> have designed a starch gel electrolyte for lithium-ion batteries, where LiTFSI was dissolved into the solution delivering a high ionic conductivity around  $10^{-3}$  S  $\text{cm}^{-1}$  (**Figure 5a**). The prior study promotes the application of starch hydrogel for ZIBs. Zhi et al.<sup>[85]</sup> have developed a hybrid polymer starch-polyacrylamide electrolyte with the

**Table 1.** Summary of polymer electrolytes (“*n*” represents the number of the repeat group, the degree of polymerization).

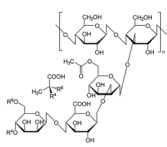
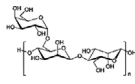
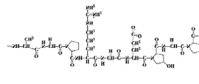
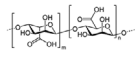
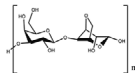
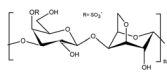
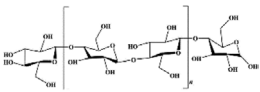
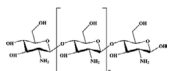
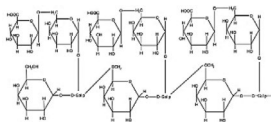
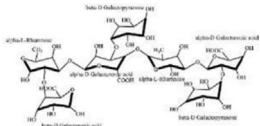
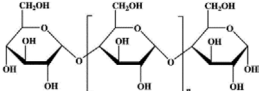
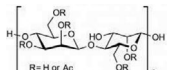
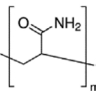
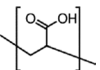
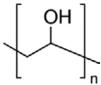
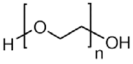
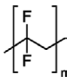
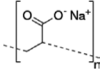
Materials	Structures	Molecular weight [g mol <sup>-1</sup> ]	Ionic conductivities [S cm <sup>-1</sup> ]	Market price and size (CAGR) <sup>a)</sup>	Advantages	Disadvantages	Ref.
Xanthan gum		933.75 × <i>n</i> ( <i>n</i> = 2000–20 000)	1.46 × 10 <sup>-2</sup>	Price: \$1850/T; Size: \$452.8 million by 2022 with a CAGR of 3.25%	<ul style="list-style-type: none"> <li>• No precipitation with sulfate salts</li> <li>• Highly sticky and shapeable</li> <li>• High ionic conductivity</li> <li>• High thermal stability (the same ionic conductivity after 1-year storage at 5 °C)</li> <li>• Dendrite prevention and low self-corrosion of the zinc anode</li> <li>• Low cost</li> </ul>	<ul style="list-style-type: none"> <li>• Low mechanical strength</li> <li>• Quasi-solid state</li> <li>• Limited market size</li> </ul>	[47,77,105,106]
Guar gum <sup>b)</sup>		535.15 × <i>n</i> ( <i>n</i> = 90–1500)	1.07 × 10 <sup>-2</sup>	Price: \$74 400/T; Size: 1.15 billion by 2022 with a CAGR of 7.9%	<ul style="list-style-type: none"> <li>• Highly sticky and shapeable</li> <li>• High ionic conductivity</li> <li>• Dendrite prevention</li> <li>• Anti-flammability</li> </ul>	<ul style="list-style-type: none"> <li>• Low mechanical strength</li> <li>• Quasi-solid state</li> <li>• High cost</li> </ul>	[48,107]
Gelatin <sup>c)</sup>		10 000	6.15 × 10 <sup>-3</sup>	Price: \$3000–5000/T; Size: \$3.6 billion by 2023 with a CAGR of 6.6%	<ul style="list-style-type: none"> <li>• High swelling ratio</li> <li>• High ionic conductivity</li> <li>• Dendrite prevention</li> <li>• Large and stable market size</li> </ul>	<ul style="list-style-type: none"> <li>• Low mechanical strength</li> <li>• Quasi-solid state</li> <li>• Relative high cost</li> </ul>	[46,108]
Alginate <sup>d)</sup>		216.12 × <i>n</i> ( <i>n</i> = 150–2000)	4.32 × 10 <sup>-2</sup>	Price: \$900–5000/T; Size: \$1.02 billion by 2027 with a CAGR of 4.7%	<ul style="list-style-type: none"> <li>• Medium swelling ratio</li> <li>• High ionic conductivity</li> <li>• Dendrite prevention</li> <li>• Large and stable market size</li> <li>• Gelation with bi-cations</li> </ul>	<ul style="list-style-type: none"> <li>• Low mechanical strength</li> <li>• Less stretchability</li> </ul>	[49,109]
Agar		336.33 × <i>n</i> ( <i>n</i> = 400)	—	Price: \$10 000–34 000/T; Size: \$346.85 million by 2025 with CAGR of 4.9%	<ul style="list-style-type: none"> <li>• Medium swelling ratio</li> <li>• Potential dendrite prevention</li> </ul>	<ul style="list-style-type: none"> <li>• Low mechanical strength</li> <li>• Quasi-solid state</li> <li>• Limited market size</li> <li>• High cost</li> <li>• Precipitate with sulfate salts</li> </ul>	[110]
κ-Carrageenan		690.51 × <i>n</i> ( <i>n</i> = 580–810)	3.32 × 10 <sup>-2</sup>	Price: \$4000-15000/T; Size: \$1.2 billion by 2025 with a CAGR of 5.6%.	<ul style="list-style-type: none"> <li>• Flexible</li> <li>• Dendrite prevention</li> <li>• Bending resist</li> <li>• Stable market size</li> </ul>	<ul style="list-style-type: none"> <li>• Low mechanical strength</li> <li>• Quasi-solid state</li> <li>• Relative high expense</li> </ul>	[111]



Table 1. Continued.

Materials	Structures	Molecular weight [g mol <sup>-1</sup> ]	Ionic conductivities [S cm <sup>-1</sup> ]	Market price and size (CAGR) <sup>a)</sup>	Advantages	Disadvantages	Ref.
Cellulose (Carboxymethyl cellulose sodium (CMC)) <sup>e)</sup>		500 000	$1.64 \times 10^{-2}$	Price: \$500–2000/T; Size: \$2.32 billion by 2025 with a CAGR of 2.7%	<ul style="list-style-type: none"> <li>• High ionic conductivity</li> <li>• Dendrite prevention</li> <li>• Large and stable market size</li> <li>• Low cost</li> </ul>	<ul style="list-style-type: none"> <li>• Low mechanical strength</li> <li>• Quasi-solid state</li> </ul>	[50,112]
Chitosan		$161.16 \times n$ ( $n = 310\text{--}1200$ )	—	Price: \$10 000–26000/T; Size: \$20.5 billion by 2023 with a CAGR of 24.7%	<ul style="list-style-type: none"> <li>• Potential dendrite prevention</li> <li>• Large and stable market size</li> <li>• High swelling ratio</li> </ul>	<ul style="list-style-type: none"> <li>• Low mechanical strength</li> <li>• Quasi-solid state</li> <li>• High cost</li> </ul>	[113]
Gum Arabic <sup>f)</sup>		250 000	—	Price: \$2600–2850/T; Size: \$469.25 million by 2023 with a CAGR of 5.9%	<ul style="list-style-type: none"> <li>• Potential dendrite prevention</li> <li>• Stable price and market</li> </ul>	<ul style="list-style-type: none"> <li>• Low mechanical strength</li> <li>• Quasi-solid state</li> </ul>	[114–116]
Gum karaya <sup>f)</sup>		9 500 000	—	Price: \$580–700/T; Size: \$90.1 million by 2025 with a CAGR of 3.4%	<ul style="list-style-type: none"> <li>• Potential dendrite prevention</li> <li>• Stable price and market</li> <li>• Low cost</li> </ul>	<ul style="list-style-type: none"> <li>• Low mechanical strength</li> <li>• Quasi-solid state</li> <li>• Limited market</li> </ul>	[114,117]
Starch		$359.33 \times n$ ( $n = 2800\text{--}280\ 000$ )	—	Price: \$330/T; Size: \$106.64 billion by 2022 with a CAGR of 6.64%	<ul style="list-style-type: none"> <li>• Potential dendrite prevention</li> <li>• Stable price and large market</li> <li>• Low cost</li> <li>• Shearing-thicken ability</li> </ul>	<ul style="list-style-type: none"> <li>• Low mechanical strength</li> <li>• Quasi-solid state</li> </ul>	[118]
Aloe vera gel <sup>g)</sup>		$267.28 \times n$ ( $n = 1\text{--}1400$ )	—	Price: \$7000–8000/T; Size: \$2.14 billion by 2022 with a CAGR of 7.6%	<ul style="list-style-type: none"> <li>• High swelling ratio</li> <li>• Potential dendrite prevention</li> <li>• Large market size</li> <li>• Biocompatible</li> </ul>	<ul style="list-style-type: none"> <li>• Relatively low mechanical strength</li> <li>• Quasi-solid state</li> <li>• High cost</li> </ul>	[119,120]
PAM		$71.08 \times n$ ( $n = 500\text{--}100\ 000$ )	$1.2 \times 10^{-1}$	Price: \$1538/T; Size: \$3.85 billion by 2021 with CAGR of 6.8%	<ul style="list-style-type: none"> <li>• High swelling ratio</li> <li>• High ionic conductivity</li> <li>• Dendrite prevention</li> <li>• Large and stable market size</li> <li>• Low cost</li> <li>• Great stretchability</li> <li>• Anti-flammability</li> </ul>	<ul style="list-style-type: none"> <li>• Low tensile strength</li> </ul>	[42,121,122]
PAA		$72.06 \times n$ ( $n = 25\text{--}100\ 000$ )	$2.75 \times 10^{-1}$	Price: \$53 000/T; Size: \$706 million by 2026 with a CAGR of 5.7%	<ul style="list-style-type: none"> <li>• High ionic conductivity</li> <li>• Dendrite prevention</li> </ul>	<ul style="list-style-type: none"> <li>• Relatively low mechanical strength</li> <li>• High cost</li> </ul>	[96,123]

**Table 1.** Continued.

Materials	Structures	Molecular weight [g mol <sup>-1</sup> ]	Ionic conductivities [S cm <sup>-1</sup> ]	Market price and size (CAGR) <sup>a)</sup>	Advantages	Disadvantages	Ref.
PVA		44.05 × n (n = 300–2700)	1.26 × 10 <sup>-2</sup>	Price: \$2066.46/T; Size: \$1.2 billion by 2025 with a CAGR 6.1%	<ul style="list-style-type: none"> <li>• Dendrite prevention</li> <li>• Competitive cost</li> <li>• High mechanical strength</li> <li>• High thermal stability</li> <li>• High binding strength</li> </ul>	<ul style="list-style-type: none"> <li>• Slightly low ionic conductivity</li> <li>• Not waterproof</li> </ul>	[94,124]
PEO		44.05 × n + 18.02 (n = 6–230 000)	10 <sup>-3</sup>	Price: \$3000–\$3500/T Size: \$308.8 million by 2026 with a CAGR of 2.3%	<ul style="list-style-type: none"> <li>• Dendrite prevention</li> <li>• High mechanical strength</li> <li>• High thermal stability</li> <li>• High binding strength</li> </ul>	<ul style="list-style-type: none"> <li>• Low ionic conductivity on its own</li> <li>• Requiring ionic liquids to improve ionic conductivities</li> </ul>	[54,125]
PVDF		64.03 × n (2800–8300)	1.69 × 10 <sup>-2</sup>	Price: \$20 000–80 000/T; Size: \$1.16 billion by 2025 with a CAGR of 6.7%.	<ul style="list-style-type: none"> <li>• Dendrite prevention</li> <li>• High mechanical strength</li> <li>• High thermal stability</li> <li>• High binding strength</li> </ul>	<ul style="list-style-type: none"> <li>• High cost</li> <li>• Low ionic conductivity on its own</li> </ul>	[73,125]
PANa		94.04 × n (15–850)	0.2	Price: \$1000–1800/T Size: \$2.14 billion by 2026 with a CAGR of 5.7%	<ul style="list-style-type: none"> <li>• High swelling ratio</li> <li>• High ionic conductivity</li> <li>• Dendrite prevention</li> <li>• Large and stable market size</li> </ul>	<ul style="list-style-type: none"> <li>• Relatively low mechanical strength</li> </ul>	[99,126]

<sup>a)</sup>CAGR = compound annual growth rate; <sup>b)</sup>Image for guar gum structure: Reproduced with permission.<sup>[48]</sup> Copyright 2019, Elsevier; <sup>c)</sup>Image for gelatin structure: Reproduced with permission.<sup>[46]</sup> Copyright 2018, American Chemical Society; <sup>d)</sup>Image for alginate structure: Reproduced with permission.<sup>[49]</sup> Copyright 2019, Elsevier; <sup>e)</sup>Image for cellulose (CMC) structure: Reproduced with permission.<sup>[50]</sup> Copyright 2018, American Chemical Society; <sup>f)</sup>Images for gum Arabic and gum karaya structures: Reproduced with permission.<sup>[114]</sup> Copyright 2018, Elsevier; <sup>g)</sup>Image for aloe vera gel structure: Reproduced under the terms of the CC-BY Creative Commons Attribution 3.0 Unported license (<https://creativecommons.org/licenses/by/3.0>).<sup>[119]</sup> Copyright 2008, The Author, published by MDPI.

ionic conductivity of  $2.65 \times 10^{-2}$  S cm<sup>-1</sup> (Figure 5b-ii). Assembling with the cathode MoS<sub>2</sub>, the battery delivers a specific capacity of 202.6 mAh g<sup>-1</sup> at a current density of 0.1 A g<sup>-1</sup>, a desirable energy density of 148.2 Wh kg<sup>-1</sup> and good cycling stability with a capacity retention of 98.6% over 600 cycles. Apart from the starch hydrogel, the distinct feature of starch complexes to other polysaccharides is that the starch solution is able to form a shearing-thicken suspension if the water content is less than the starch. Suspensions will become more rigid under the shearing-thickening mechanism once exposed to a sudden impact, which is beneficial to protecting the batteries and avoiding the short circuit. A similar strategy has been applied to LIBs for which the shearing-thicken electrolyte has been replaced with silica, while for aqueous ZIBs, starch complexes could be better choices that are suitable for the aqueous system. Further investigation could be applied to the concept of shearing-thickening electrolyte for ZIBs.

### 5.1.2. Protein-Based Electrolyte

Distinguishing from polysaccharides, the gelation process of most proteins is usually induced by heating where the protein is unfolded and aggregated to form a 3D network, whereas for gelatin or casein, the gelation happens by cooling hot solution and acidification, respectively.<sup>[76]</sup> Gelatin, a well-known food thickener, consists of a large number of glycine, proline, and 4-hydroxy proline residues. The gelation process follows the heat-cooling procedure in which gel forms with the formation of hydrogen bonding during the cooling below 35 °C.<sup>[86]</sup> Han et al.<sup>[46]</sup> have synthesized a gelatin-based hydrogel electrolyte with an ionic conductivity of  $6.1 \times 10^{-3}$  S cm<sup>-1</sup>. Accompanying with LiMn<sub>2</sub>O<sub>4</sub>, solid-state ZIBs deliver a specific capacity of 110.2 mAh g<sup>-1</sup> (Figure 6a). Moreover, Yan and co-workers<sup>[87]</sup> also applied gelatin as the quasi-solid electrolyte. Integrating with cathode expanded V<sub>2</sub>O<sub>5</sub> on stainless steel

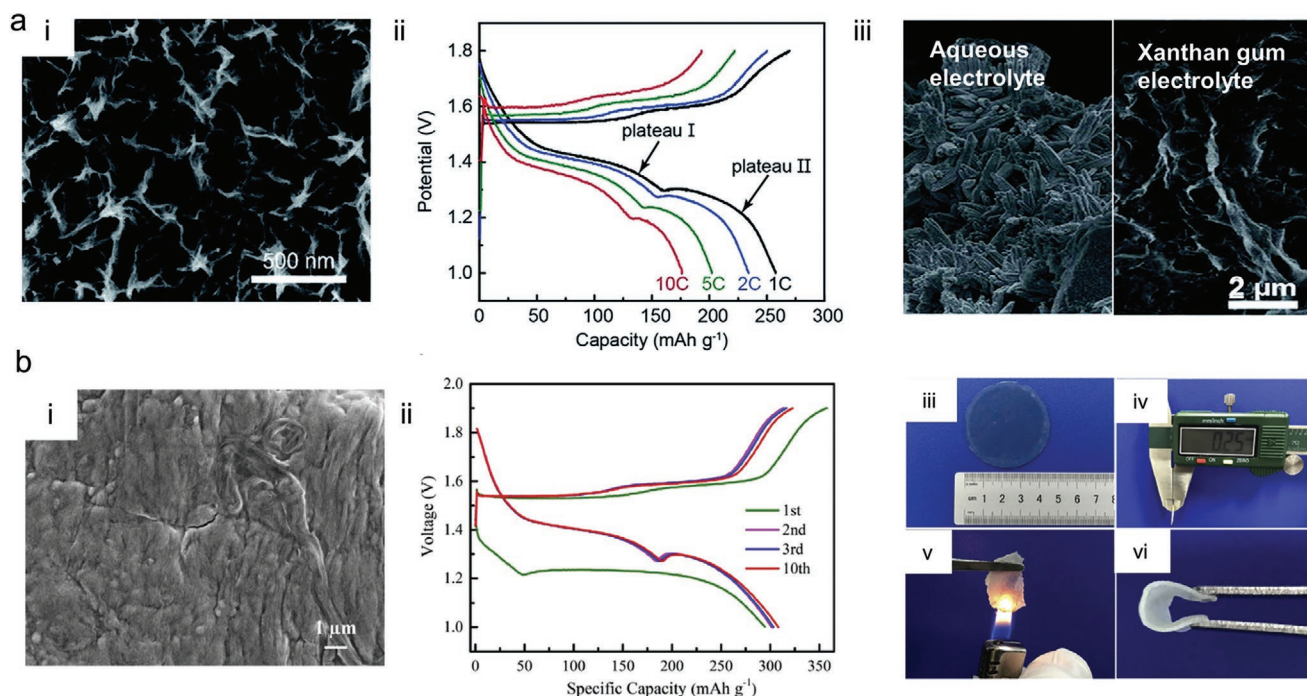


**Figure 3.** a) Characterizations for xanthan polymer electrolyte. i) SEM image of the xanthan polymer electrolyte. ii) Galvanostatic discharge curves at rates of 1 to 10 C, respectively. iii) SEM images of the zinc anode of aqueous and hydrogel electrolytes after cycling. a) Reproduced with permission.<sup>[47]</sup> Copyright 2018, Royal Society of Chemistry. b) Characterizations for guar gum polymer electrolyte. i) SEM image of the guar gum polymer electrolyte. ii) The charging/discharging profiles of the initial three cycles and the 10th cycle at the current density of 0.3 A g<sup>-1</sup>. iii–vi) Digital photos of the guar gum electrolyte under bending and burning states. b) Reproduced with permission.<sup>[48]</sup> Copyright 2019, Elsevier B.V.

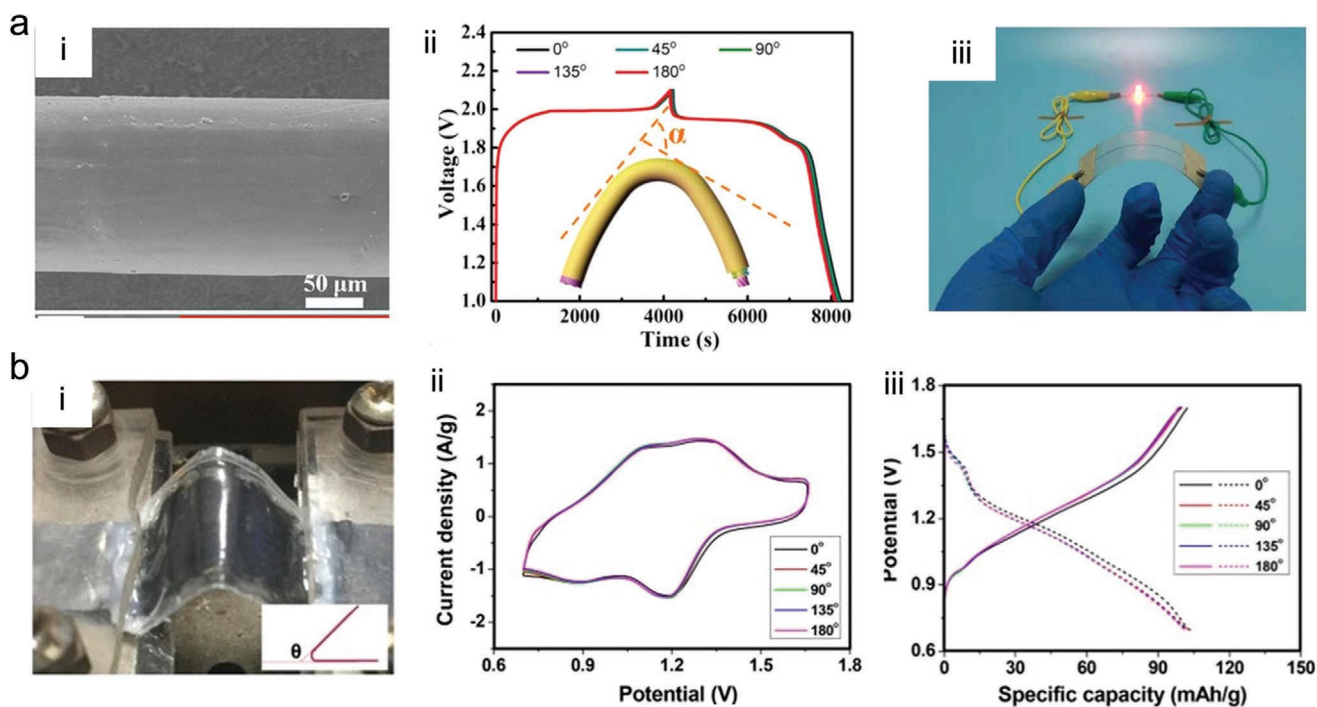


**Figure 4.** a) Characterizations for CMC hydrogel electrolyte of a coaxial-fiber aqueous zinc-ion battery (CARZIBs). i) SEM images of the ZnSO<sub>4</sub>-CMC gel electrolyte coating the surface of Zn nanosheet array on the CNTF. ii) Charge-discharge curves of the CARZIBs at a current density of 0.1 A cm<sup>-2</sup> under different bent angles. iii) Photograph of a red LED illuminated by a fully charged CARZIB under 90° bending. a) Reproduced with permission.<sup>[83]</sup> Copyright 2019, American Chemical Society. b) Characterizations for laminated structure flexible ZIBs. i) Optical photograph of bent battery. ii) CV curves versus bending angle at the scan rate of 2 mV s<sup>-1</sup>. iii) Charge-discharge curves of the ZIBs at a current density of 2 A g<sup>-1</sup> under different bent angles. b) Reproduced with permission.<sup>[50]</sup> Copyright 2018, American Chemical Society.

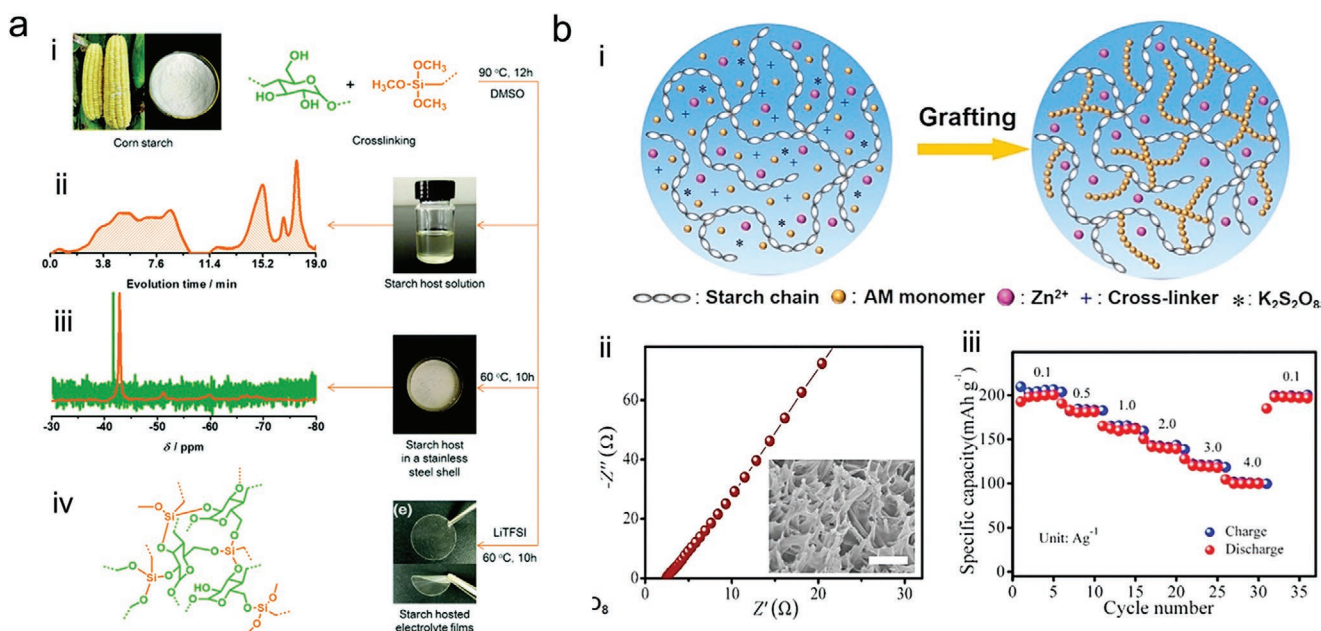


**Figure 5.** a) The preparation method of starch hosted electrolyte films and molecular structural characterization of the starch host. Reproduced with permission.<sup>[84]</sup> Copyright 2016, Royal Society of Chemistry. b) Characterizations of starch/PAM polymer electrolyte. i) Schematic diagram for fabricating the starch/PAM polymer electrolyte; ii) EIS spectroscopy; iii) rate performance. b) Reproduced with permission.<sup>[85]</sup> Copyright 2019, Elsevier B.V.

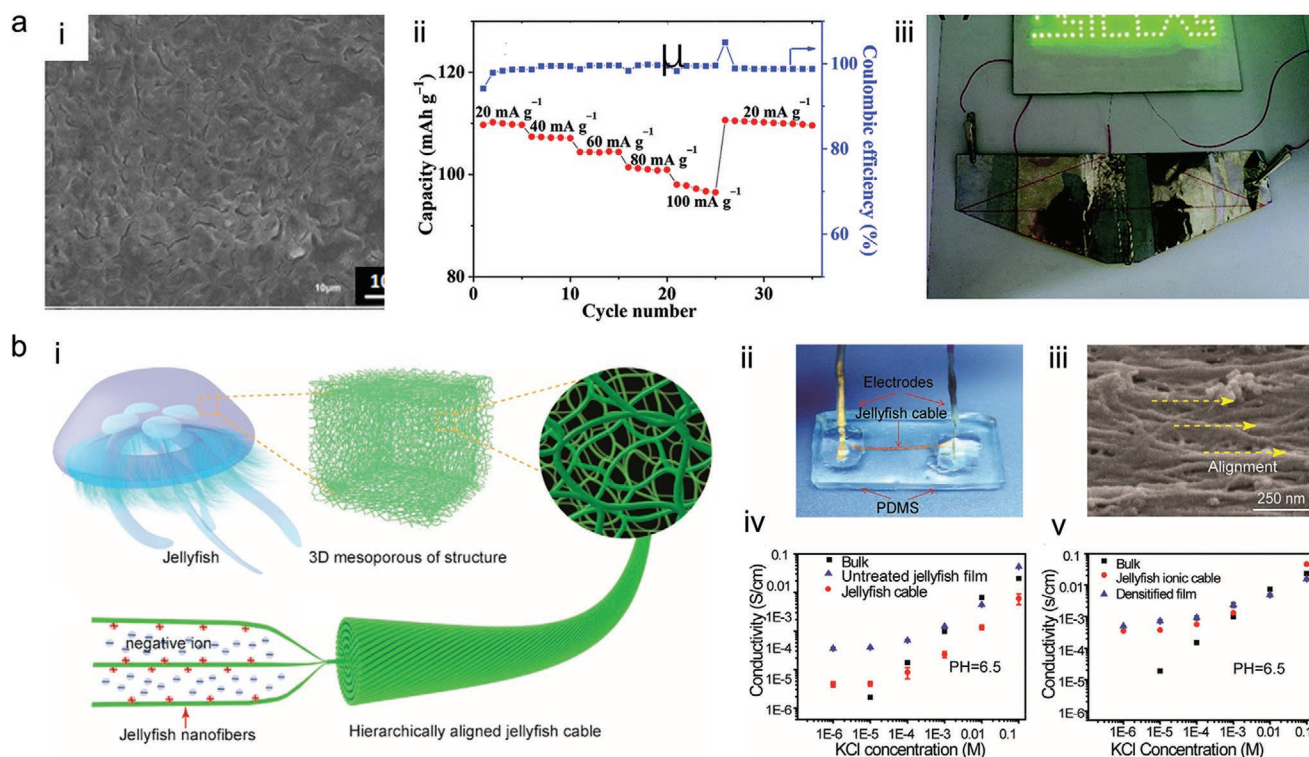
mesh, a high capacity of 361 mAh g<sup>-1</sup> ZIB was attained under different bending states. Collagen, forming the triple-helix structure after gelation, is also essential to apply in ZIBs. Amine and carboxylic acid presented in the collagen could naturally induce positive charges on the surface for facilitating ion transport. Hu et al.<sup>[88]</sup> have synthesized a collagen electrolyte from jellyfish with KCl aqueous solution, and the mesoporous structure was beneficial for salt storage. As shown in Figure 6b (iv),(v), the cable-like electrolyte exhibits an ionic conductivity that increases with the concentration of KCl. Besides from gelatin, protein-based hydrogel electrolytes are merely utilized in ZIBs, whereas preliminary results of the collagen provide an alternative strategy for the development of biomass hydrogel electrolytes.

Table 1 summarizes the reported biomass hydrogel electrolytes regarding their structures, ionic conductivities, market price and size, with associated advantages and disadvantages. Potential candidates for ZIBs are also listed, such as agar, gum karaya and aloe vera gel. Considering the data analysis of the clustering plot shown in Figure 2c, biomass polymer electrolytes exhibit high ionic conductivities in the magnitude of 10<sup>-2</sup> S cm<sup>-1</sup>, whereas pristine biomass polymer electrolytes suffered from tensile strength less than 200 kPa. Due to the lack of systematic analysis for polysaccharides and protein-based hydrogel electrolytes, there are no further factors related with ionic conductivity being revealed, such as the influence from the molecular weight, water content and the degree of polymerization. However, with the development of hydrogel electrolytes, a data mining strategy could be an essential method to exploit the clustering relation in depth.

## 5.2. Synthetic Porous Hydrogel Electrolytes

Owing to the essential 3D porous structure, hydrogels, such as polyacrylamide (PAM), poly(vinyl alcohol) (PVA), poly(acrylic acid) (PAA) and sodium polyacrylate (PANa), have been reported for ZIBs. Especially PAM hydrogel electrolytes, various HBPEs based on PAM have been intensively investigated by Zhi and co-workers because of their high ionic conductivity and easy fabrication process. Apart from advantages in electrochemical, there is also benefits in market price and size for PAM and PVA as listed in Table 1.

PAM formed by the polymerization of either acrylamide monomers or *N,N'*-methylene bis(acrylamide) monomer acrylamide (AM)<sup>[70]</sup> is often utilized to flocculate solids in a liquid. The cross-linked polymer exhibiting the porous structure in Figure 7a can absorb and retain extremely large amounts of aqueous electrolyte owing to the amide groups which form strong hydrogen bonds with water molecules. The hydrated PAM is a soft gel that is used in gel electrophoresis and as a super water-absorbing polymer (SAP) exhibiting a stretchable and self-healing capabilities. The pristine PAM hydrogel electrolyte synthesized by Zhi<sup>[42]</sup> coupled with an aqueous solution of 2 M ZnSO<sub>4</sub> + 0.2 M CoSO<sub>4</sub> processes a high ionic conductivity of 0.12 S cm<sup>-1</sup> at 300% swelling ratio. Laminating with Co(III) rich-Co<sub>3</sub>O<sub>4</sub> nanorod material, Zn/Co(III) rich-Co<sub>3</sub>O<sub>4</sub> batteries can offer a high voltage of 2.2 V (Figure 6b-i), a capacity of 205 mAh g<sup>-1</sup> (Co<sub>3</sub>O<sub>4</sub>) and an excellent cycling stability of 92% capacity retention even after 5000 cycles. Self-healing ZIBs have also been developed using PAM as the electrolyte host. By substituting the electrode substrate with carboxylated-polyurethane (CPU), the as-fabricated battery indicates a self-healing ability



**Figure 6.** a) Characterizations of gelatin-based polymer electrolyte. i) SEM image of the gelatin polymer electrolyte; ii) Cycling performance of the full cell at various current densities; iii) the damage test of a tandem solid-state battery powering the LED twinkle light. a) Reproduced with permission.<sup>[46]</sup> Copyright 2018, Royal Society of Chemistry. b) Characterizations of collagen-based polymer electrolyte. i) Schematic diagram demonstrating the working principle of the jellyfish cable as an inexpensive, stable, and high ionic conductivity material; ii) photograph showing the jellyfish cable device; iii) SEM of the jellyfish cable nanostructure; iv,v) ionic conductivity performances. b) Reproduced with permission.<sup>[89]</sup> Copyright 2019, American Chemical Society.

attributing to the reversible formation of hydrogen bonds in both PAM electrolyte and CPU substrates (Figure 7c). In terms of the cycling performance after cutting and healing, it is impressive that the capacity of  $100 \text{ mAh g}^{-1}$  can remain even at 10 C after four cycles of cutting and recovery as shown in Figure 7c-iii. Based on these characteristics and the stable macroporous structure, a few HBPEs illustrated in the latter section have been developed based on PAM host polymer with additional functionalities, such as anti-freezing, stretching and thermoresponsive abilities. The water-in-salt strategy has also been applied into PAM hydrogel electrolyte, for which Liu et al.<sup>[90]</sup> have developed a highly concentrated dual-ion electrolyte (HCE) based on the PAM framework. Assembling cathode  $\text{LiVPO}_4\text{F}$ , the hybrid battery expanded a stable voltage window to 2.2 V with a high-voltage discharge plateau of nearly 1.9 V.

PVA is a non-toxic thermoplastic polymer produced by the hydrolysis of poly(vinyl acetate) instead of polymerization. Because of its good mechanical properties, excellent thermal stability, and high gas barrier properties, it has been applied to battery production as the solid polymer for LIBs. Owing to the presence of hydroxyl groups, PVA exhibits a high-water absorbing ability which is essential for the storage of aqueous electrolyte. PVA-based electrolytes for ZIBs have also been studied intensively covering neutral and mild alkaline or acid electrolytes. Lu et al.<sup>[41]</sup> invented a flexible rechargeable quasi-solid-state Zn/MnO<sub>2</sub> battery for the mild acid system, for which

PVA hydrogel electrolyte was immersed with  $\text{ZnCl}_2/\text{MnSO}_4$  solution offering an ionic conductivity of  $1.26 \times 10^{-2} \text{ S cm}^{-1}$ . Assembling with Zn and MnO<sub>2</sub> electrodes on a polymer host poly(3,4-ethylene dioxythiophene) (PEDOT) as shown in Figure 8a, the fabricated Zn/MnO<sub>2</sub>@PEDOT flexible battery presents a high capacity of  $282.4 \text{ mAh g}^{-1}$ , 77.7% of its initial capacity and nearly 100% Coulombic efficiency after 300 cycles (Figure 8b). Mohamad et al.<sup>[92]</sup> and Vatsalarani et al.<sup>[93]</sup> have also developed PVA-based SPEs for alkaline ZIBs, which exhibited a high ionic conductivity of  $8.7 \times 10^{-3} \text{ S cm}^{-1}$ , where KOH and  $\text{Zn}(\text{CH}_3\text{COO})_2$  are dissolved into the complex. Assembling within a Zn/AgO battery configuration, a minimum specific capacity loss of  $\approx 3\%$  has been observed over 20 cycles.

PAA is an anionic polymer where the side chains can lose protons and acquire a negative charge forming a polyelectrolyte, hence PAA has been utilized as the polymer electrolyte for alkaline batteries,<sup>[96]</sup> especially in zinc-air batteries to facilitate OH<sup>-</sup> ion transportation (Figure 8c). For zinc-air batteries, KOH filled PAA hydrogel electrolyte exhibits an ionic conductivity of  $2.75 \times 10^{-1} \text{ S cm}^{-1}$ .<sup>[95]</sup> Zhu et al.<sup>[97]</sup> reported a PAA based hydrogel electrolyte with  $8.4 \text{ mol L}^{-1}$  KOH solution for alkaline Zn/MnO<sub>2</sub> batteries exhibiting an ionic conductivity of  $0.288 \text{ S cm}^{-1}$  at room temperature. Benefitting from strong mechanical strength, a flexible and printed alkaline Zn/MnO<sub>2</sub> battery fabricated by Gaikwad et al.<sup>[98]</sup> exhibited superior flexibility and low-temperature adaptability where there was no decrease in electrochemical performance under bending

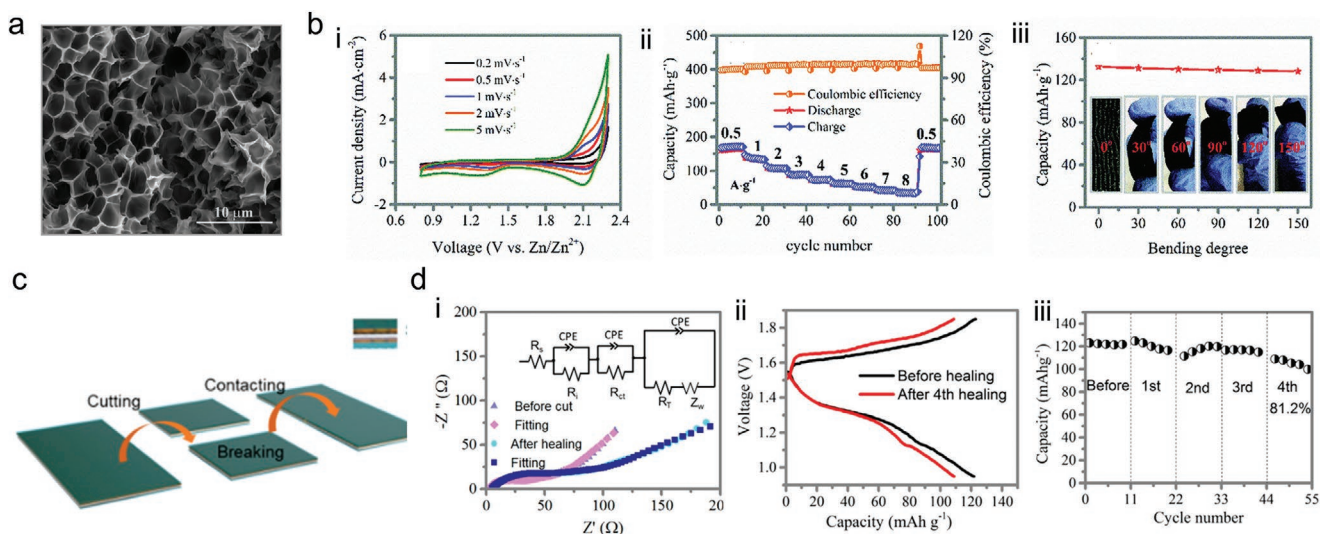


**Figure 7.** Characterizations of PAM polymer electrolyte. a) SEM image of PAM polymer electrolyte. b) Electrochemical performances of the solid-state Zn/Co(III) rich- $\text{Co}_3\text{O}_4$  batteries. i) CV curves at different scan rates; ii) rate performance; iii) specific capacity at different bending states. a,b) Reproduced with permission.<sup>[42]</sup> Copyright 2018, Royal Society of Chemistry. Characterizations of self-healing PAM polymer electrolyte. c) Demonstration of the self-healing PAM based ZIBs. d) Electrochemical characterizations. i) EIS curves of the healable Zn/ $\delta$ -NMOH battery before and after healing; ii) Discharge-charge profiles at 10 C before healing and after fourth healing; iii) capacity change versus healing times at 10 C before healing and after fourth healing. c,d) Reproduced with permission.<sup>[91]</sup> Copyright 2019, American Chemical Society.

conditions ranging from 3.81 cm to 0.95 cm bending radii at  $-20^\circ\text{C}$  (Figure 8d).

PANa, also a polyelectrolyte with negatively charged carboxylic groups in the main chain, is in the 3D crosslinked structure with the ionic groups located inside. Huang et al.<sup>[99]</sup> have developed a NiCo-Zn battery employing PANa hydrogel as the electrolyte (Figure 9a), and nickel-cobalt hydroxide and zinc nanosheets deposited on Au@CNT papers as the electrode. The hydrogel electrolyte exhibits a high ionic conductivity of  $0.2\text{ S cm}^{-1}$  and a stable capacity delivery under deformations where the capacities delivered are 87% and 97% of its initial state for 500 cycles stretching and 1500 cycles compression respectively as shown in Figure 9b. Furthermore, Li<sup>[100]</sup> also developed an alkaline ZIB utilizing PANa with a lifespan of capacity decay of 0.02% per cycle over 4200 cycles.

The hydrogels summarized above are conventional polymer electrolytes only employed as physical frameworks without noticeable improvement in electrochemical performances. Therefore, Mo et al.<sup>[101]</sup> have developed a polyelectrolyte exhibiting zwitterionic chains. Zwitterionic chains contain equal numbers of opposite charged functional groups within each repeated unit,<sup>[102]</sup> where the counterions in the aqueous solution, that is,  $\text{Zn}^{2+}$  and  $\text{SO}_4^{2-}$ , can be attracted to separate side groups forming two ion migration channels under an external electric field, as shown in Figure 9c. The zwitterionic sulfobetaine/cellulose hydrogel electrolytes (ZSC-gel) was synthesized by forming covalent networks between cellulose nanofibrils and poly[2-(methacryloyloxy)ethyl]diethyl-(3-sulopropyl) (PMAEDS) through physical entanglement and intertwining. The as-prepared ZSC gel electrolyte possesses a high ionic conductivity of  $2.46\text{ S cm}^{-1}$  and a stable cycling performance compared with PAM electrolyte during bending as shown in Figure 9d. Attribute to the positive channel consisting

of sulfonate groups,  $\text{Zn}^{2+}$  ions from the electrolyte are uniformly deposited on the anode, thus improving the stability. Integrating in the Zn/MnO<sub>2</sub>, the polyelectrolyte-battery exhibited a high capacity of  $148\text{ mAh g}^{-1}$  at 6.5 C with a retention of 90.42% of the initial capacity after 1200 cycles. A flexible device fabricated from this material verified its feasibility in wearable electronics. Moreover, Luo et al. have synthesized a polyelectrolyte hydrogel electrolyte (PZHE), whereas the poly[2-(methacryloyloxy)ethyl]dimethyl-(3-sulopropyl) (PSBMA) not only possesses strong water retention capacity to inhibit side reaction and dendrites but also immobilizes anions to increase the  $\text{Zn}^{2+}$  transference number to 0.656.<sup>[103]</sup>

### 5.3. Oxide Hydrogel Electrolytes

Oxide hydrogels, also the potential candidates for ZIB electrolytes, are merely been investigated. Fan<sup>[41]</sup> developed a fume silica based quasi-solid electrolyte which exhibited an ionic conductivity of  $\approx 8.1\text{ S} \times 10^{-3}\text{ cm}^{-1}$  at room temperature. Apart from the silica, it is expected to further exploit the metal oxide hydrogel electrolytes. Metal oxides such as ZnO and CuO can absorb water, thus forming ionically conductive hydrogels by ionic bonding. Metal oxide hydrogels have hardly been investigated in ZIBs, while Tan et al.,<sup>[104]</sup> who synthesized the ionically conductive hydrogel from a non-stoichiometric oxide of the zinc, revealed the potential application in ZIBs. The porous structure generated in the ZnO hydrogel exists in two states, a hydrated (H) and dehydrated (DH) state depending on the ambient humidity. Assembling this with Zn and Cu electrodes, a redox system in the gel with the oxidation and reduction peaks was attained around 0.61 V and 0.28 V (vs SHE), respectively. Hence, there is a reversible reaction of  $\text{Zn} \leftrightarrow \text{Zn}^{2+} + 2\text{e}^-$  in the battery. Additionally, the gel has humidity-triggered changes in optical,

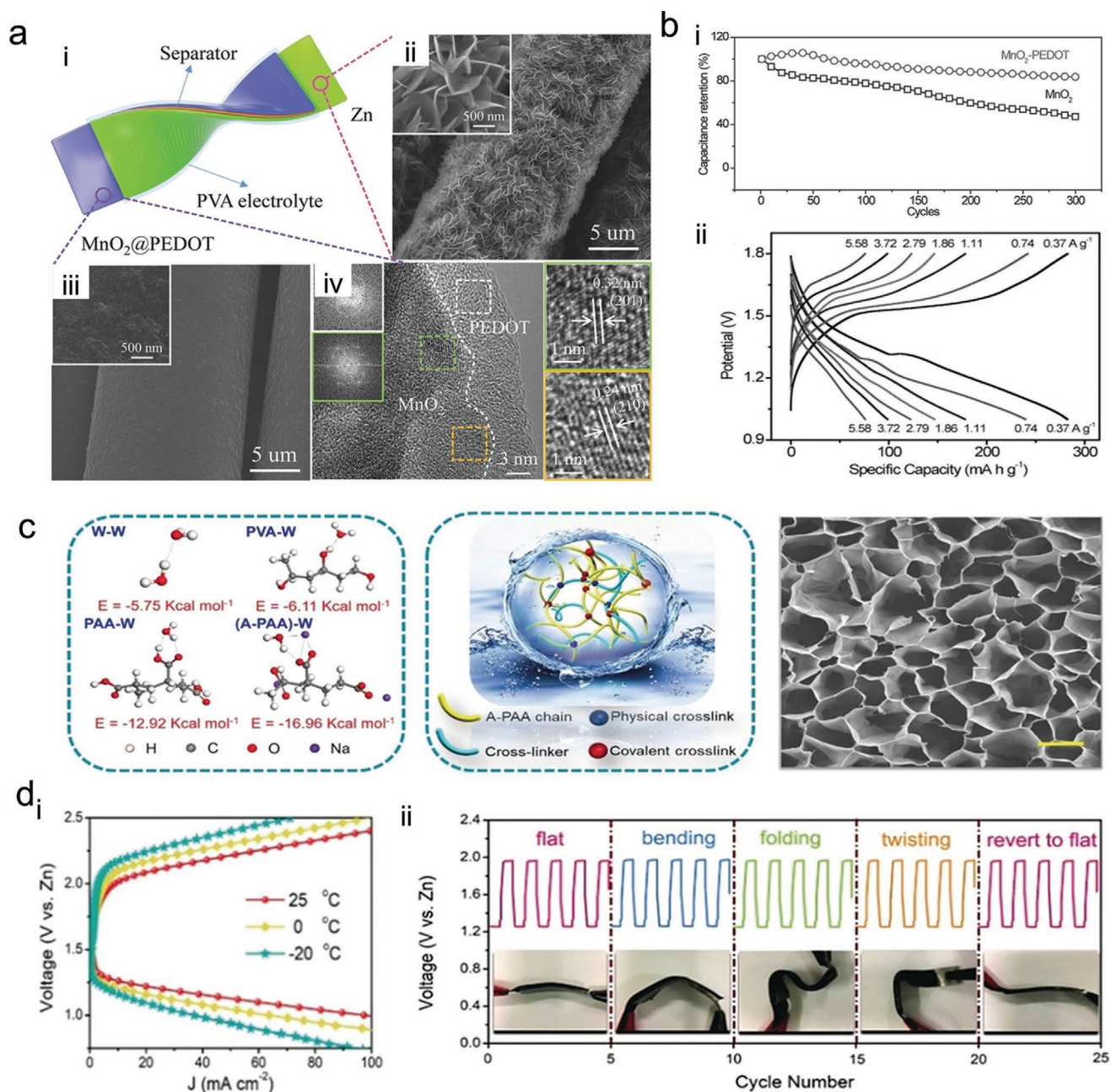


**Figure 8.** Characterizations of PVA-based polymer electrolyte. a-i) Schematic illustration of flexible quasi-solid-state Zn-MnO<sub>2</sub>@PEDOT battery; ii) SEM images of the Zn anode; iii, iv) SEM and HRTEM images of MnO<sub>2</sub>@PEDOT respectively. b-i) Cycling performance at the current density of 1.11 A g<sup>-1</sup>; ii) Galvanostatic charge/discharge profiles at different current densities. a, b) Reproduced with permission.<sup>[94]</sup> Copyright 2017, Wiley-VCH. Characterizations of PAA based polymer electrolyte. c) Material model and SEM image of PAA electrolyte. Scale bar = 10 μm. d-i) Charging/discharging profiles for PAA based battery under different temperatures; ii) cycling profiles with the current density of at 2 mA cm<sup>-2</sup> under various mechanical deformations. c, d) Reproduced with permission.<sup>[95]</sup> Copyright 2020, Wiley-VCH.

electrical, and electrochemical properties that can be exploited for a wide range of applications such as thermo-hygroscopic windows, infrared radiation (IR) blocking windscreens, and the construction of electrochemical cells for energy harvesting. The integration of a thermo-hygroscopic window combined with IR blocking windscreen leads to extensive energy savings in buildings. Exposed to the ambient condition, the ionic conductivity increases with the time exposed for water absorption.

## 6. Hybrid Polymer Electrolytes

As demonstrated above, the HPE offers a comparable ionic conductivity above 10<sup>-3</sup> S cm<sup>-1</sup> permitting a highly reversible electrochemical reaction within the batteries, whereas the mechanical strength is limited compared to the solid polymer electrolyte. HBPE is the best trade-off to satisfy different requirements. The HBPE is a composite formed by more than

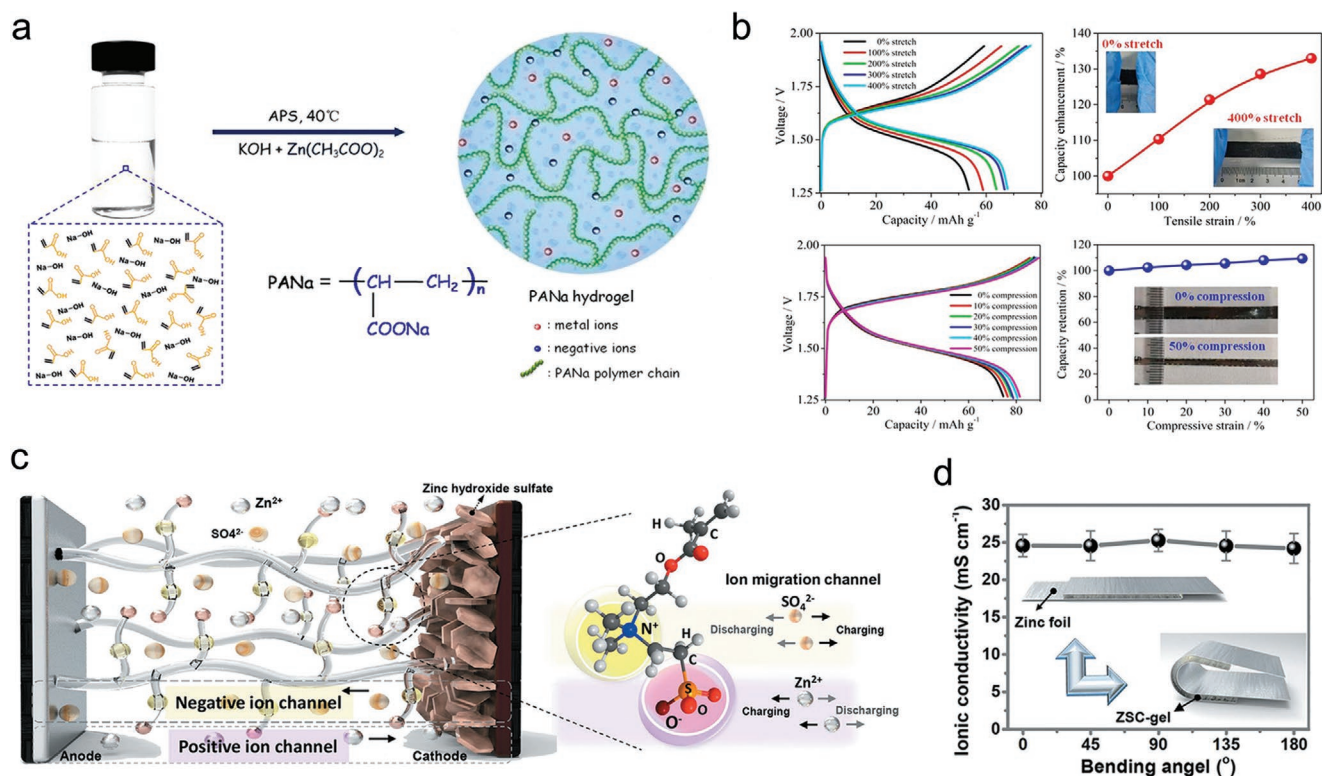


**Figure 9.** Characterization of PANa electrolyte for ZIBs. a) Preparation of the PANa polyelectrolyte; b) electrochemical performance of the battery comprising the PANa polyelectrolyte under stretching and compressing. a,b) Reproduced with permission.<sup>[99]</sup> Copyright 2019, Elsevier B.V. Characterization of polyzwitterions of the ZSC-gel electrolyte. c) Schematic illustration of the ZSC-gel electrolyte in a ZIB under an external electric field. Under the external electric field, ion migration channels are formed in the gel matrix owing to the electrostatic attractions between the zwitterionic groups and positive/negative ions. d) Ionic conductivities of the ZSC-gel electrolyte at different bending states (45°, 90°, 135°, 180°). c,d) Reproduced with permission.<sup>[101]</sup> Copyright 2020, Wiley-VCH.

one polymer structure in chemical crosslinking and physical grafting methods, and the focus is on enhancing at least one functionality of the entire polymer electrolyte. A few strategies have been investigated to increase the mechanical strength and stretchability, such as compositing hydrogel with solid polymer electrolytes and polysaccharide with PAM, respectively. Aside from the mechanical enhancement, additional functionalities such as dendrite prevention, anti-freezing and thermoresponsive properties have also been developed.

### 6.1. Hybrid PEO Electrolytes

Similar to the thermoreversible polymer electrolyte demonstrated in PAM based hydrogel electrolytes, PEO derivatives and Pluronic hydrogel electrolytes (PHEs) also exhibit the sol-gel transition, which is in the gel state at room temperature but transit to the liquid phase upon cooling.<sup>[127]</sup> Cu's group<sup>[44]</sup> has developed a PHE based on a representative thermo-reversible polymer, poly(ethylene oxide)-poly(propylene oxide)-poly(ethylene oxide) (PEO<sub>53</sub>-PPO<sub>34</sub>-PEO<sub>53</sub>, Pluronic, F77). After mixing with ZnSO<sub>4</sub> and Li<sub>2</sub>SO<sub>4</sub> aqueous solution, the hydrogel electrolyte exhibits a superior thermoresponsiveness. The electrolyte is in the sol phase when the temperature is -5 °C, where F77 aggregates into micelles hydrating the PEO shell. However, when the temperature increases to 25 °C, the hydrophobic

interactions induce the dehydration of PEO and PPO interface eventually causing hard-sphere crystallization (Figure 10a,b). Integrating with cathodes LiMnO<sub>2</sub>, the flexible cooling recovery battery possesses a reversible capacity of 71.1  $\text{mAh g}^{-1}$  at 20.0  $\text{mA g}^{-1}$ . As demonstrated in Figure 10c, the as-fabricated device exhibited lower capacity fading (only 4% after 100 cycles) in the bending-recovering process. The cool-recovered feature is beneficial to the improvement of wettability among the electrode-electrolyte interface, which is the strategy to heal the interface at low temperature.

### 6.2. Hybrid PAM Electrolytes

Attribute to the exploitation by Zhi et al.,<sup>[38]</sup> the mechanical strength for hydrogel electrolytes can be improved by compositing polysaccharides with PAM. As shown in Figure 11a, the hybrid electrolyte was formed by grafting PAM on the gelatin chains with ZnSO<sub>4</sub> and MnSO<sub>4</sub> solution via free radical polymerization, forming a double crosslinking network. The PAN fiber membrane was utilized as a physical host for the hydrogel electrolyte. The hydrogel electrolyte is in a porous structure as shown in Figure 11b, exhibiting ionic conductivity of  $1.76 \times 10^{-2} \text{ S cm}^{-1}$ . The entire flexible device was fabricated in a sandwich structure consisting of the MnO<sub>2</sub> cathode, Zn anode and the hybrid electrolyte, which possesses a high specific capacity



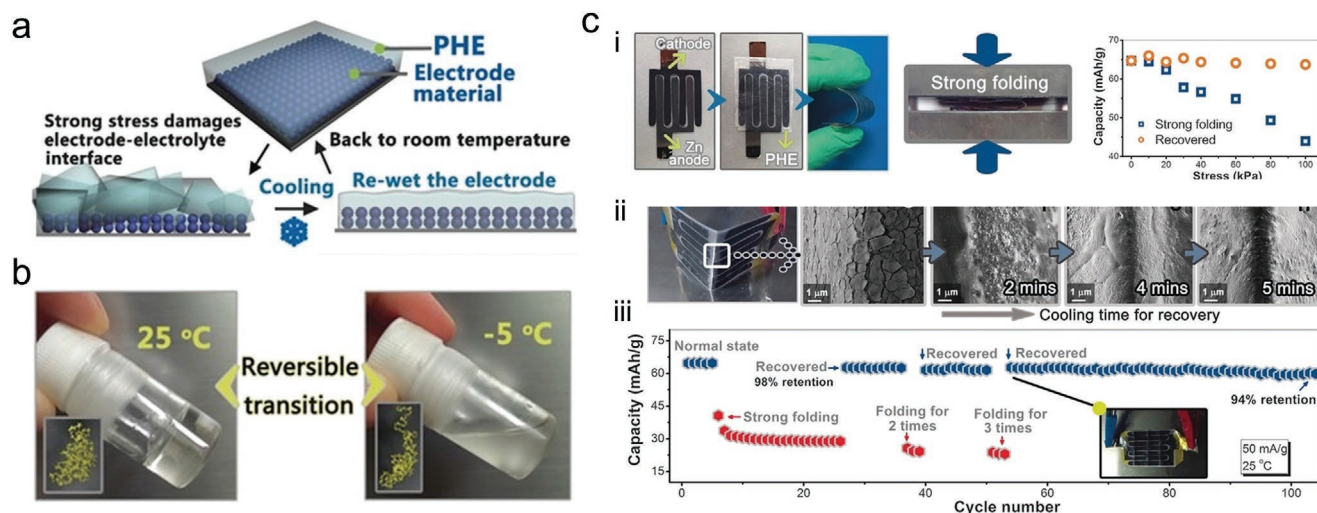


**Figure 10.** a) The cooling–recovery function by the incorporation of a thermoreversible Pluronic hydrogel electrolyte (PHE). b) Photographs of 40% (w/w) PHE and corresponding polymer chain configurations (insets) at different temperatures. c) Electrochemical characterizations under deformation and recovery. i) Capacity change of the battery upon folding and recovering with different stresses. ii) Top-view SEM images of the broken PHE-electrode area due to the strong folding (100 kPa) after cooling for 2, 4, and 5 min at  $-8\text{ }^{\circ}\text{C}$ . iii) Cycling performance at  $25\text{ }^{\circ}\text{C}$  with strong folding interrupts (100 kPa) and (inset) the photograph of the recovered battery after folding three times (at different positions). a–c) Reproduced with permission.<sup>[44]</sup> Copyright 2017, Wiley-VCH.

of  $306\text{ mAh g}^{-1}$  and a capacity retention of 97% even under extreme conditions such as bending, cutting, puncturing and firing (Figure 11d). Owing to the gelatin in the long chain and PAN membrane, the hybrid electrolyte achieved a tensile strength of up to 776 MPa compared to the 1.25 MPa for the pristine hydrogel electrolyte (Figure 11c). However, as revealed by Yan et al.,<sup>[128]</sup> the optimized gelatin/PAM dual network gel without the physical host only exhibits a tensile strength of 0.268 MPa, which indicates that most of the physical properties are contributed by the physical host such as the PAN membranes. It also correlates with the study of alginate/PAM hybrid electrolyte<sup>[49]</sup> where the modulus of the hydrogel greatly increased from 2.36 to 51.83 kPa after introducing a second ionically crosslinked alginate network to the pristine PAM structure. Hence, for PAM hybrid hydrogel electrolytes, although the polysaccharide/PAM double network could enhance the mechanical strength for the PAM hydrogel, physical hosts such as PAN membrane and glass fiber membranes are still necessary to enhance the strength greater than 1 MPa.

Aside from mechanical enhancement, additional functionalities, such as anti-freezing capability were also developed by Zhi and co-workers,<sup>[43]</sup> for which the specific capacity can be retained over 80%, even at  $-20\text{ }^{\circ}\text{C}$ . The anti-freezing (AF) hydrogel electrolyte was synthesized by introducing binary solution ethylene glycol (EG) into the PAM structure, where hydroxyl groups of the EG molecules bind covalently with isocyanate groups, forming stable chemical anchoring instead of simple hydrogen-bonding interactions in the polymer chains (Figure 12a). Integrating with  $\alpha\text{-MnO}_2$ /carbon nanotube (CNT) nanocomposite cathode, the anti-freezing battery delivered a specific capacity of  $24\text{ mAh g}^{-1}$  at a current density of  $0.3\text{ A g}^{-1}$ , even at  $-20\text{ }^{\circ}\text{C}$ , while for PAM-battery, there is a degraded capacity upon cooling with a capacity retention of 27.44% (Figure 12c). The as-prepared hybrid AF hydrogel electrolyte also exhibits a superior adhesion with electrodes for which the

ionic conductivity reaches  $14.6\text{ mS cm}^{-1}$  at  $-20\text{ }^{\circ}\text{C}$ , similar to the magnitude seen at ambient temperature as displayed in Figure 12b. In contrast, for pristine PAM electrolyte, there is a considerable increase in the charge transfer resistance ( $R_{ct}$ ) because of the freezing electrolyte.

Other PAM derivatives developed even provide thermal responsiveness transmitting  $\text{Zn}^{2+}$  ions at low temperature while impeding the mechanism at high temperature. Zhi et al.<sup>[45]</sup> are pioneers who fabricated a temperature-sensitive ZIB based on the sol–gel transition of the copolymer poly(*N*-isopropyl acrylamide-co-acrylic acid) (PNA) with aqueous solution  $\text{ZnSO}_4$  and  $\text{MnSO}_4$ . As shown in Figure 13a-i, the PNA sol–gel electrolyte is in the sol state at low temperature, where the strong hydrogen bond forces the surrounding water molecules formed by carbonyl and imide groups enable the formation of micelles in the electrolyte inducing the free migration of  $\text{Zn}^{2+}$  ions. However, at a high temperature, reaching the gelation point of the gel at  $50\text{ }^{\circ}\text{C}$ , the polymer is in the gel state, where the hydrogen bonds break and the hydrophobic force of isopropyl groups are dominant in the network inhibiting the free movement of  $\text{Zn}^{2+}$  ions. The transition is reversible where the resistance of PNA electrolyte is constant at  $18.1\text{ M}\Omega$  at room temperature, while achieves  $160.9\text{ M}\Omega$  when heated to  $70\text{ }^{\circ}\text{C}$ . Integrating with the cathode  $\alpha\text{-MnO}_2$ , this thermoresponsive battery exhibits a specific capacity of  $145\text{ mAh g}^{-1}$  at  $0.1\text{ A g}^{-1}$  and significantly decreases to  $80\text{ mAh g}^{-1}$  at  $50\text{ }^{\circ}\text{C}$ . The gradual gelation process for the sol–gel electrolyte is essential to act as the switch to protect the battery from the thermal explosion. As indicated in charge–discharge cycles (Figure 13a (ii)), a reversible thermal-induced cycling performance was observed where the charging process was inhibited by the increasing internal resistance when heating to  $70\text{ }^{\circ}\text{C}$  but reversed upon cooling. Leading on from the sol–gel transition, Niu et al.<sup>[129]</sup> have proposed another strategy, which is thermoresponsive by volume shrink instead of the unstable sol–gel reaction.

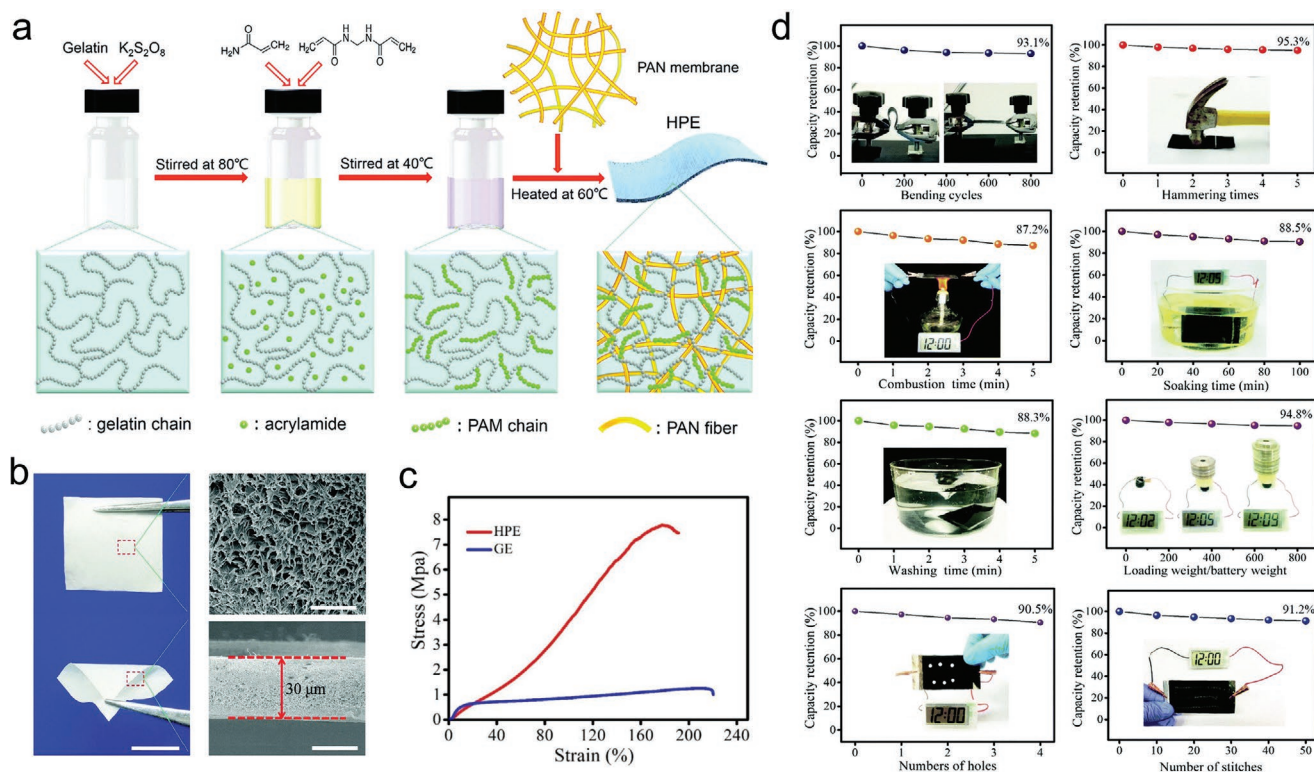


**Figure 11.** a) Schematic diagram of the synthetic route of the HPE. The hierarchical structured HPE was synthesized by grafting PAM on gelatin chains that are filled in the network of PAN electrospun fiber membrane through a facile free radical polymerization approach. b) Optical image of the HPE film. c) Tensile tests for HPE compared with gelatin hydrogel electrolyte. d) Electrochemical performance of the solid-state rechargeable ZIB in different destructive tests. a–c) Reproduced with permission.<sup>[38]</sup> Copyright 2018, Royal Society of Chemistry.

Similarly, poly(*N*-isopropyl acrylamide) (PNIPAM) was also applied as the host owing to the superior thermoresponsive ability where there was a volume shrink when the temperature was beyond its volume phase transition temperature (VPTT); however, acrylamide (AM) was added instead to increase the VPTT to 78 °C due to a large number of hydrophilic acylamino groups in the AM monomer. At room temperature, the aqueous solution with  $\text{Zn}(\text{CF}_3\text{SO}_3)_2$  was swollen in the porous structure showing hydrophilic behavior (Figure 13b-i); whereas when the temperature was above VPTT, the PNIPAM hydrogel suffered from a rapid volume shrinkage releasing aqueous solution from pores and inhibiting the migration of  $\text{Zn}^{2+}$  ions. Assembled with the polyaniline (PANI) cathode, the flexible battery delivers a specific capacity of 168.7 mAh  $\text{g}^{-1}$  at a current density of 0.1 A  $\text{g}^{-1}$ . However at 60 °C, benefiting from a quick transition via hydrophobic association and dehydration reaction, the battery suddenly shuts down rather than gradually increases the resistance, as shown in Figure 13b-ii.

Apart from PNIPAM based sol-gel electrolytes, a composite of SPE and HPE can also employ the thermoreversible feature. Following the study from Cui,<sup>[44]</sup> Zhī's group<sup>[13]</sup> developed a PAM-based hydrogel electrolyte coated with F77, as shown in Figure 14a. Similarly, the electrolyte is a gel at the room temperature and turns back to a liquid at temperatures less than 0 °C. Accompanied with Zn and  $\text{CoFe}(\text{CN})_6$ , F77 skin above the PAM hydrogel electrolyte improves the utilization of  $\text{CoFe}(\text{CN})_6$ , reaching a capacity of 142.34 mAh  $\text{g}^{-1}$  at 1 A  $\text{g}^{-1}$  compared to

119.89 mAh  $\text{g}^{-1}$  without the F77 coating (Figure 14d). Moreover, the battery shows an excellent rate performance and cycling stability for which there is capacity retention of 93.4% over 2000 cycles at 3 A  $\text{g}^{-1}$  as demonstrated in Figure 14e–g. A flexible device fabricated in the cable structure also maintains a constant power supply under bending and twisting deformations.

### 6.3. Hybrid PVA Electrolytes

Apart from PAM-based hybrid hydrogel electrolytes, PVA-based hybrid electrolytes are also widely utilized in ZIBs in both alkaline and acid systems.<sup>[130]</sup> Mitra et al.<sup>[131]</sup> have investigated the feasibility of copolymer PVA–PAA for alkaline ZIBs, for which the KOH is used as the aqueous solution (Figure 15a). The addition of PAA into the host polymer PVA enhances the ionic conductivity.<sup>[132]</sup> Employed with the  $\text{MnO}_2$  electrode and Zn powders, the copolymer PVA–PAA has similar electrochemical performance with the aqueous ZIBs using the separator (Figure 20a), which delivers a specific capacity of 283 mAh  $\text{g}^{-1}$  at a current density of 0.3 mA  $\text{cm}^{-2}$ . Further investigation manifested that fabricated battery exhibited robustness and flexibility which can light up LED lights. Wong<sup>[133]</sup> and co-workers<sup>[134]</sup> also developed poly(vinyl alcohol) (PVA)/glycerol gel electrolyte which exhibits anti-freezing ability (Figure 15b). The borax crosslinking in the framework strongly interact with PVA chains, hence effectively prohibiting the formation of ice

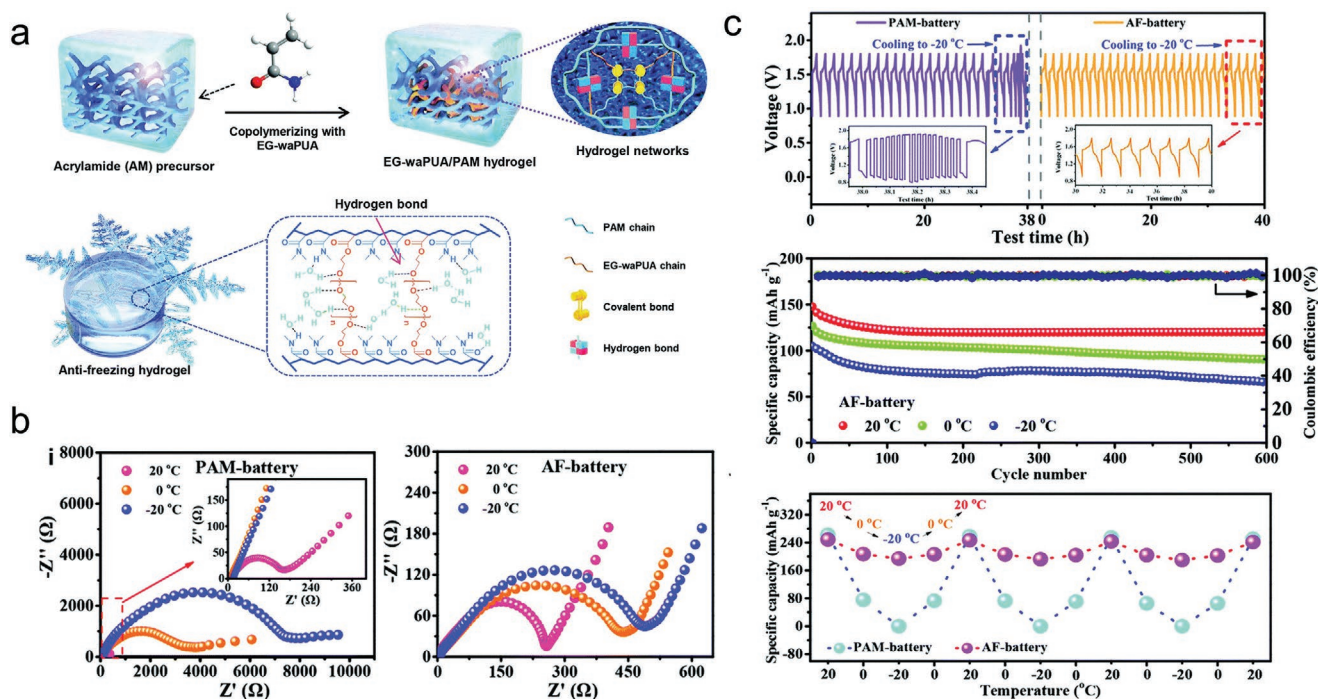


**Figure 12.** a) Design principles of the AF-gel electrolyte. b) Comparison of impedance spectra of pristine PAM and AF polymer electrolyte. c) Electrochemical cycling performance of the AF-battery under different temperatures consisting of voltage profiles at  $0.8 \text{ A g}^{-1}$ ; cycling performance at  $2.4 \text{ A g}^{-1}$  of the AF-battery at different temperatures; and cyclic test of the PAM-battery and AF-battery under  $20$ ,  $0$ , and  $-20 \text{ }^\circ\text{C}$  at  $0.3 \text{ A g}^{-1}$ . a–c) Reproduced with permission.<sup>[43]</sup> Copyright 2019, Royal Society of Chemistry.

crystals within the whole gel network. The freezing point was reduced to  $-60 \text{ }^\circ\text{C}$ , thus resulting in a high ionic conductivity of  $10.1 \text{ mS cm}^{-1}$  and great mechanical properties at  $-35 \text{ }^\circ\text{C}$ .

#### 6.4. Additives in Hybrid Polymer Electrolytes

As indicated above, owing to additives, HBPEs exhibit additional functionalities satisfying the realistic application scenarios in both electrochemical and mechanical aspects. Attributed to comprehensive investigations by Zhi<sup>[135]</sup> and Liang<sup>[136,137]</sup> additives for AZIBs are categorized into four groups with emphasis on specific functions involving evaluating ionic conductivities, modulating electrochemical windows, zinc dendrite inhibition, and extra functionalities. Avoiding from side-reactions illustrated in Section 2, AZIBs suffered from a low electrochemical window. A typical additive to expand the operating voltage is sodium dodecyl sulfate (SDS), where a stability window of aqueous ZIBs improved from  $2.0$  to  $2.5 \text{ V}$  for cathode  $\text{Na}_2\text{MnFe}(\text{CN})_6$ .<sup>[36]</sup> Details for ionic conductivities, electrochemical windows and zinc anode are discussed in Section 9. However, for polymer electrolytes, because of the lower ionic transportation and greater zinc dendrite prevention abilities, the development of polymer electrolytes for flexible ZIBs are emphasized on evaluating ionic conductivities and adding additional features. For solid polymer electrolytes, ionic liquids such as  $[\text{EMIM}]\text{BF}_4$ <sup>[73]</sup> and  $\text{EMIMTFSI}$ <sup>[138]</sup> are organic additives improving ionic conductivities from  $10^{-6} \text{ S cm}^{-1}$  to  $10^{-3} \text{ S cm}^{-1}$ . Moreover, inorganic additives, such as  $\text{SiO}_2$ <sup>[138]</sup> and  $\text{TiO}_2$ <sup>[54]</sup> are also essential materials to expand the free volume

for segmental motions. For hydrogel electrolytes, anti-freezing ability, thermoresponsive ability and high tensile strength are achieved with various additives. **Table 2** summarizes the up-to-date additives applied in flexible ZIBs.

### 7. Flexible Device Configurations

The flexible ZIBs require flexibility not only in electrolytes but for the electrodes as well. Therefore, each component in the battery should be flexible instead of conventional rigid electrodes. Currently, there are two types of structures employed in flexible ZIBs, that is, sandwich film and 1D cable-type constructions. Owing to the ease of fabrication, sandwich-type devices have been widely applied so far in a laminated structure compositing a layer of hydrogel electrolyte in between the electrodes (**Figure 16a**).<sup>[38,46,101]</sup> To enhance the flexibility in electrodes, carbon nanotube papers and carbon cloth are often utilized as the electrode substrates rather than pristine Zn foil. Apart from carbon-based substrates, poly(ethylene terephthalate) (PET) has also been applied as the film substrate providing flexibility. Cable type constructions shown in **Figure 16b,c** are constructed from a single carbon fiber tow. Zhi's group fabricated a cable-type ZIB by integrating two helix carbon nanotube (CNT) yarns where  $\text{MnO}_2$  paste and zinc were roll-dip coated and roll electro-deposited on CNT yarns, respectively.<sup>[143]</sup> The as-fabricated yarns were encapsulated parallelly within a silicone tube immersed with PAM electrolyte in between. The entire device exhibits a high volumetric energy density of  $53.8 \text{ mWh cm}^{-3}$  and a specific capacity of  $302.1 \text{ mAh g}^{-1}$ . The

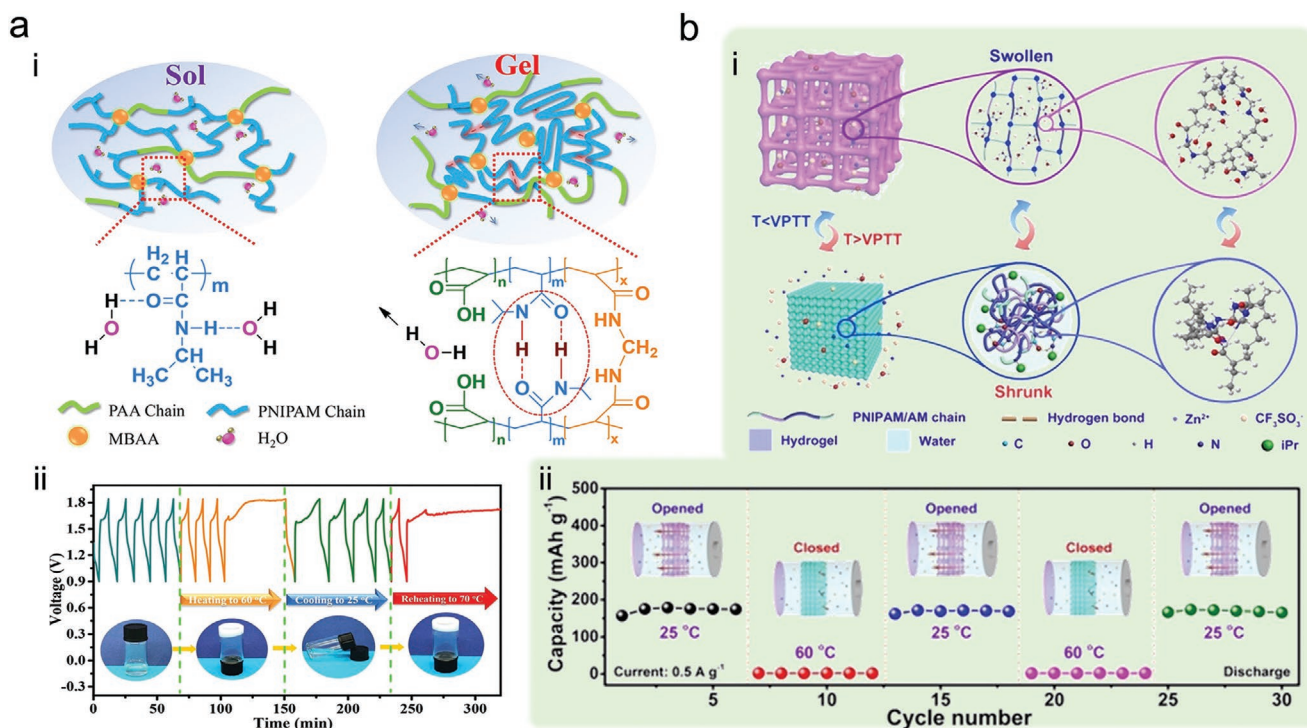


**Figure 13.** a) Characterizations of PNA electrolyte. i) Design principles of smart ZIBs based on sol–gel transition electrolyte; ii) charge–discharge cycles of the Zn/ $\alpha$ -MnO<sub>2</sub> battery with the PNA sol–gel electrolyte at different temperatures. a) Reproduced with permission.<sup>[45]</sup> Copyright 2018, Elsevier B.V. b) Characterizations of PNIPAM electrolyte. i) The working mechanism of the thermal-gated PNIPAM/AM electrolytes with VPTT; ii) electrochemical performance at different temperatures. b) Reproduced with permission.<sup>[129]</sup> Copyright 2020, Wiley-VCH.

unidirectional fiber in the cable endows ZIBs with more deformation robustness and shape versatility. Huang et al.<sup>[144]</sup> even designed a wearable alkaline nickel/cobalt–zinc-based battery in the structure of a yarn-based cable-type battery. This battery delivered an energy density of 8 mWh cm<sup>-3</sup>. PVA–KOH gel electrolyte was also employed in the parallel-yarn cable type ZIBs,<sup>[145]</sup> where the energy density was 4.6 mWh cm<sup>-3</sup>. Distinguished from yarn-based ZIBs, Wei et al.<sup>[83]</sup> have designed a fiber-based cable type ZIB by directly coating on the CNT fiber. As demonstrated in Figure 16c, Zinc nanosheet arrays (NSA), cellulose-based CMC–ZnSO<sub>4</sub> electrolyte and zinc hexacyanoferrate (ZnHCF) were coated on a single CNT fiber in the sequence by a facile electrodeposition method. Although the specific capacity delivered is 100.2 mAh cm<sup>-3</sup>, less than the yarn-based Zn–MnO<sub>2</sub> cable battery, the volumetric energy density is 195.39 mWh cm<sup>-3</sup>, greater than that of the yarn-based Zn–MnO<sub>2</sub> cable battery. Therefore, cable type flexible batteries are beneficial to offering high volumetric energy densities and robust deformations than sandwich flexible batteries (Figure 16d). Most fabrication reported for flexible ZIBs are designed for thin film or 1D batteries, while strategies such as island-bridge,<sup>[146]</sup> Miura fold,<sup>[147]</sup> and wavy structure<sup>[147]</sup> can also be considered for future applications.

Until now, most hydrogel-based ZIBs was designed for the application of wearable electronics. Guo<sup>[147]</sup> has summarized the essential factors to determine the flexibility of flexible zinc-ion batteries based on the radius of bending curvature. However, there is no index indicating whether the as-designed hydrogel ZIBs are feasible to be applied to the realistic scenario

of wearable devices or wearable band. Herein, inspired by the multifunctional coefficient,<sup>[148]</sup> a ranking coefficient  $\eta_r$  is proposed which is not only beneficial for the comparison but also essential for being an index of industrialization.  $\eta_r$  is the combination of electrical ( $\eta_e$ ) and mechanical coefficient ( $\eta_m$ ) concerning the magnitude of commercial wearable bands. By summarizing the world's top 5 brands for wearable band shipments over 2019–2020<sup>[149]</sup> (Table 3), as shown in the equation below, the index can be deduced regarding the average values for the capacity density ( $C_{fd}$ ) and the tensile strength ( $\sigma_{fd}$ ). If  $\eta_r$  is greater than 1, flexible ZIBs are likely to be exploited further as a product, whereas when  $\eta_r$  is close to 2, current wearable device with LIBs can be substituted with flexible ZIBs. However, owing to the heterogeneity of the data reported for different flexible ZIBs, there is a difficulty in ranking current flexible ZIBs reported according to this index. This index is also available to be applied in different realistic scenarios whereby substituting the magnitude of commercial electrochemical and mechanical properties. It will be a determinant factor for flexible ZIBs in future research.

$$\eta_r = \eta_e + \eta_m = \frac{C_{zfd}}{C_{fd}} + \frac{\sigma_{zfd}}{\sigma_{fd}} \quad (4)$$

where  $\eta_e$  and  $\eta_m$  represent electrical and mechanical coefficients, respectively;  $C_{zfd}$  and  $\sigma_{zfd}$  are capacity density and tensile strength for flexible devices of ZIBs;  $C_{fd}$  and  $\sigma_{fd}$  are average capacity density and tensile strength for commercial flexible devices.

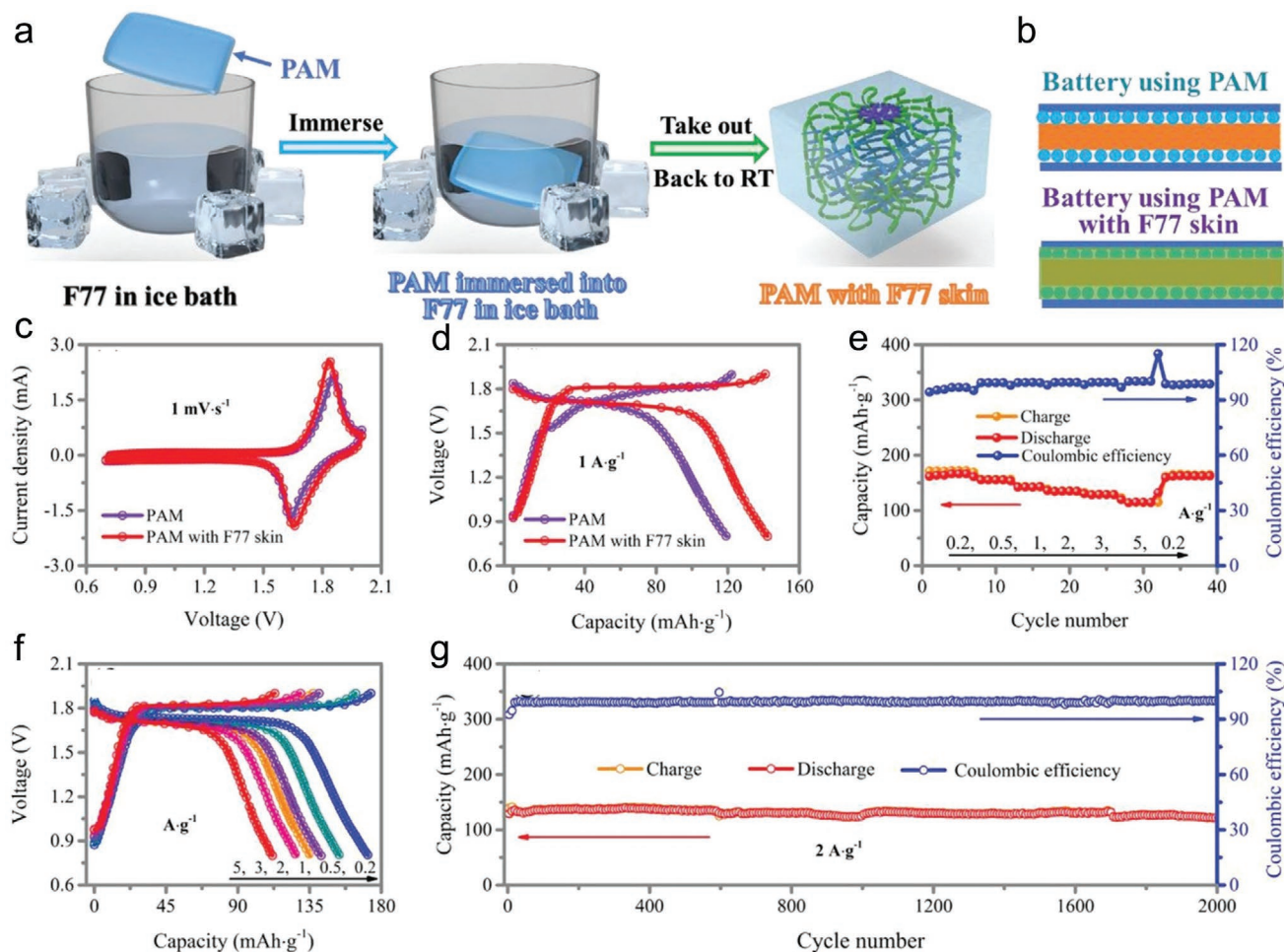


**Figure 14.** The electrochemical performance comparison of solid-state Zn/CoFe(CN)<sub>6</sub> battery using PAM hydrogel and PAM hydrogel coated with F77 hydrogel skin electrolyte: a,b) Schematic illustration of the synthetic process for PAM with F77 skin hydrogel, and battery using PAM without and with F77 skin electrolyte. c) CV curves, d) galvanostatic charge/discharge curves, e) rate performance, f) galvanostatic charge/discharge curves at different current densities, and g) cyclic stability at the current density of 3 A g<sup>-1</sup>. a–g) Reproduced with permission.<sup>[13]</sup> Copyright 2019, Wiley-VCH.

$$\eta_r = \frac{C_{zfd}}{5.79} + \frac{\sigma_{zfd}}{11.58} \quad (5)$$

## 8. Device Fabrication Strategies

The fabrication method is critical to evaluate devices for scalable production. The up-to-date fabrication strategies reported can be summarized as layer-by-layer (LbL) assembly<sup>[150]</sup> and printing techniques.<sup>[151]</sup> Layer-by-layer assembly strategies, developed half a century ago, are largely utilized in industries which have undergone several iterations. The standard conventional method for LbL assembly for batteries on planar substrates is immersive assembly, whereby the cathode substrate is sequentially immersed into polymer electrolyte solutions for in situ polymerization, with rinsing steps between the deposition steps. For experimental scale, the LbL is proceeded manually, while for industry a robotic and automated LbL is utilized in production lines as shown in **Figure 17a**. Besides, spinning LbL assembly could also be applied, where the polymer electrolyte resin is spin-coated on the electrodes.

However, traditional LbL assemblies are designed for planar substrates, vacuum-assisted resin transfer molding (VARTM) and coaxial fiber coating are LbL derivatives for nonplanar substrates. VARTM<sup>[152]</sup> (see **Figure 17c**) is a common method for carbon fiber composite process, whereby the resin flows into a laminate assisted by the vacuum chamber. The laminate is covered into a mold by a vacuum bag; hence a variable nonplanar mold could be applied. After the impregnation occurs the composite part is allowed to post-cure at the designed temperature. VARTM is advantageous for integrating the polymer zinc-ion battery to a designed complex structural component, hence increasing volumetric energy density.<sup>[74,153]</sup>

Various printing techniques have been developed for fabricating stacked batteries as well, for example, 3D printing for lithium-ion batteries<sup>[154,155]</sup> inkjet printing for Zn–Ag batteries<sup>[156,157]</sup> as shown in **Figure 17d**, screen-based printing for Zn–air batteries<sup>[158]</sup> and Zn–MnO<sub>2</sub> batteries.<sup>[81,83,115]</sup> In particular, screen printing is a promising strategy to precisely control the pattern design with adjustable rheology of the inks, where there are four steps shown in **Figure 17b**. Printing the conducting agent graphene, cathode and anode materials

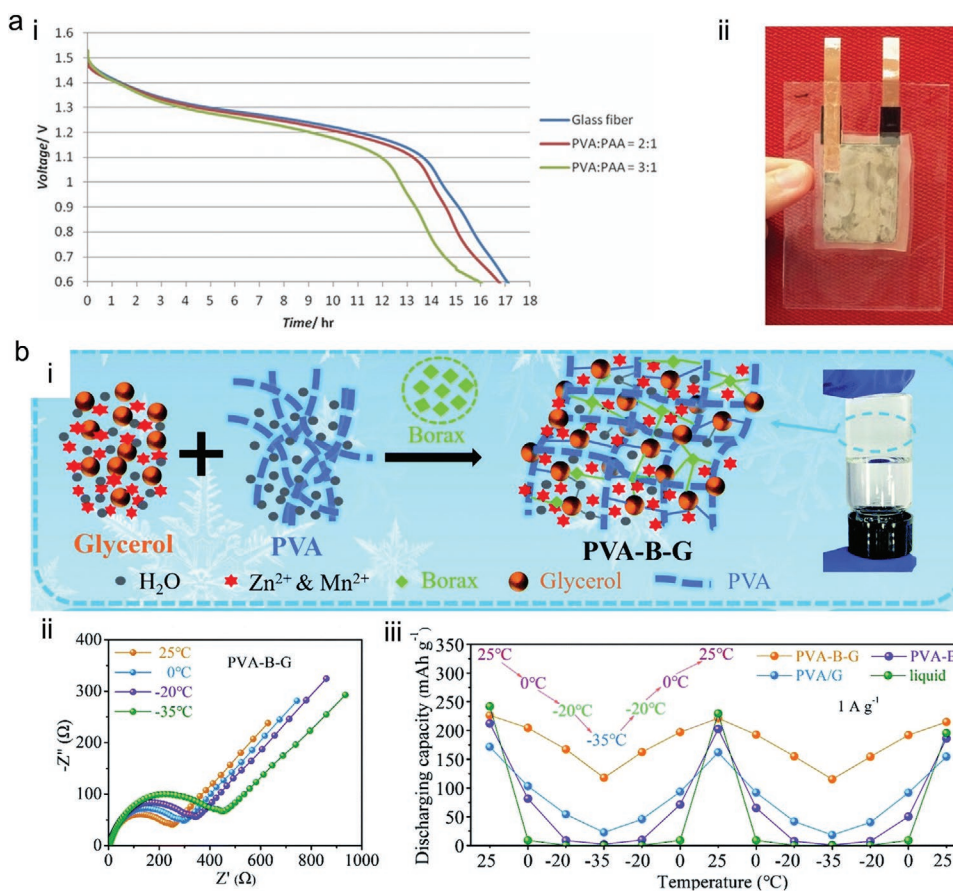


**Figure 15.** a) Characterizations of PVA/PAA polymer electrolyte. i) Galvanic discharge curves with different PVA/PAA ratios; ii) photo of the cell device. a) Reproduced with permission.<sup>[131]</sup> Copyright 2014, Wiley-VCH. b) Characterizations of PVA/glycerol polymer electrolyte. i) The synthetic scheme of PVA/glycerol electrolyte; ii) EIS plots; iii) cyclic tests for four types of batteries at 25, -20, and -35 °C at 1A g<sup>-1</sup>. b) Reproduced with permission.<sup>[133]</sup> Copyright 2020, Royal Society of Chemistry.

sequentially on the substrate such as PET, the device can be eventually fabricated by wrapping polymer electrolytes. Printing techniques are beneficial for precise machinings such as implantable batteries and flexible IoTs, while LbL assemblies are essential for large integrated components. **Table 4** summarizes the recent reported flexible devices regarding the device construction and fabrication, where LBL method and sandwich constructions are most reported. Aiming for different application scenarios, device fabrication strategies are crucial to be considered in advance of the experimental design.

## 9. Current Challenges and Potential Strategies

In this section current issues and potential strategies are reviewed regarding both electrochemical and mechanical enhancements. Moreover, besides academic perspectives, insight into the realistic demand from the market is also considered.

### 9.1. Application Scenarios

With the growth of electric vehicles, the price of LIBs is predicted to be \$62 kWh by 2030.<sup>[6]</sup> Thus, in the next decade, the

price advantage of ZIBs will not be obvious. As a competitor, it is necessary to leverage the strength of ZIBs considering the cost, electrochemical and mechanical performances. For flexible ZIBs, it is crucial to accelerate the development of the flexible devices under realistic application scenarios. Wearable devices, for example, are flexible electronics directly contacting with skin, hence biocompatibility should be considered in the design. Meanwhile, electrochemical properties and mechanical strength of flexible ZIBs are required to satisfy the customers' demand such as high operational voltage and robustness in flexibility. Moreover, to satisfy the application in different temperature regions, flexible ZIBs should be tolerant in a large temperature range from -30 to 50 °C. Being waterproof is also a factor that should be included for flexible ZIBs.

### 9.2. Achieving High Operational Voltage

Reviewing the Pourbaix diagram shown in Figure 1, the stable operational windows for AZIBs limited by HER and OER are normally below 1.9 V. The relatively low operational voltage restricts AZIBs to behave as an alternative for LIBs in high energy density applications. Hydrogel electrolyte is expected to provide a higher operational voltage owing to the high

**Table 2.** Additives in polymer electrolytes for flexible ZIBs.

Additives	Additive types	Applied polymer electrolytes	Functions	Ref.
SDS	Organic	Aqueous/hydrogel	Broaden electrochemical window	[36]
F77	Organic	Solid polymer/hydrogel	Provide thermo-response ability	[13,44]
Gelatin	Organic	Hydrogel	Enhance mechanical strength	[38]
Starch	Organic	Hydrogel	Enhance mechanical strength	[85]
Sodium alginate	Organic	Hydrogel	Enhance mechanical strength	[49]
Ethylene glycol	Organic	Hydrogel	Reduce freezing point	[43]
Glycerol	Organic	Hydrogel	Reduce freezing point	[133]
[EMIM]BF <sub>4</sub>	Organic	Solid polymer	Increase ionic conductivity	[73]
TiO <sub>2</sub>	Inorganic	Solid polymer	Increase ionic conductivity	[54]
SiO <sub>2</sub>	Inorganic	Solid polymer	Increase ionic conductivity	[138]
EMIMTFSI	Organic	Solid polymer	Increase ionic conductivity	[138]
ZnBr <sub>2</sub>	Ionic	Aqueous/hydrogel	Extra Faradaic contributions improve energy density	[139]
MnSO <sub>4</sub>	Ionic	Aqueous/hydrogel	Stabilize cathode dissolution and improve capacity for Mn-based materials	[140,136]
Al <sub>2</sub> (SO <sub>4</sub> ) <sub>3</sub>	Ionic	Aqueous/hydrogel	Broaden electrochemical window	[141]
ZnO & SnO	Inorganic	Aqueous/hydrogel (alkaline)	Suppress Zn dendritic growth in alkaline ZIBs	[142]

interfacial energy, while the reported hydrogel electrolytes still suffer from electrochemical stability issues. Up-to-date strategies exploited recently in electrolyte development emphasize suppressing water hydrolysis processes such as introducing electrolyte additives, “water-in-salt” solutions and organic/aqueous electrolytes. “Water-in-salt” is a method to suppress the water content by increasing the salt concentration. Wang et al.<sup>[164]</sup> have first applied the ultrahigh concentrated electrolyte of 20 m/kg of LiTFSI and 1 m/kg Zn(TFSI)<sub>2</sub>, which enables the dendrite-free Zn plating/stripping at nearly 100% CE, but also retains water in the open atmosphere. The strong (Zn-TFSI)<sup>+</sup>

interactions impede the formation of (Zn-(H<sub>2</sub>O)<sub>6</sub>)<sup>2+</sup>, resulting in a stable electrochemical performance rather than generating hydroxyl ion (OH<sup>-</sup>) and inducing the dead zinc (ZnO) formation. Ji et al.<sup>[37]</sup> also exploited the mechanism of “water-in-salt” electrolyte (Figure 18a), where using 30 m ZnCl<sub>2</sub> exhibited an average Coulombic efficiency of 95.4%, increasing from 73.2% in 5 m ZnCl<sub>2</sub>. Similar to that of Zn(TFSI)<sub>2</sub>, the high concentration of ZnCl<sub>2</sub> suppresses the reaction between Zn<sup>2+</sup> with OH<sup>-</sup>, hence, resulting in less octahedral ionic species, such as Zn(OH<sub>2</sub>)<sub>6</sub><sup>2+</sup> and [Zn(OH<sub>2</sub>)<sub>2</sub>Cl<sub>4</sub>]<sup>2-</sup>. Inspired by the “water-in-salt” strategy, Zhi and co-workers<sup>[13]</sup> have utilized a hydrogel

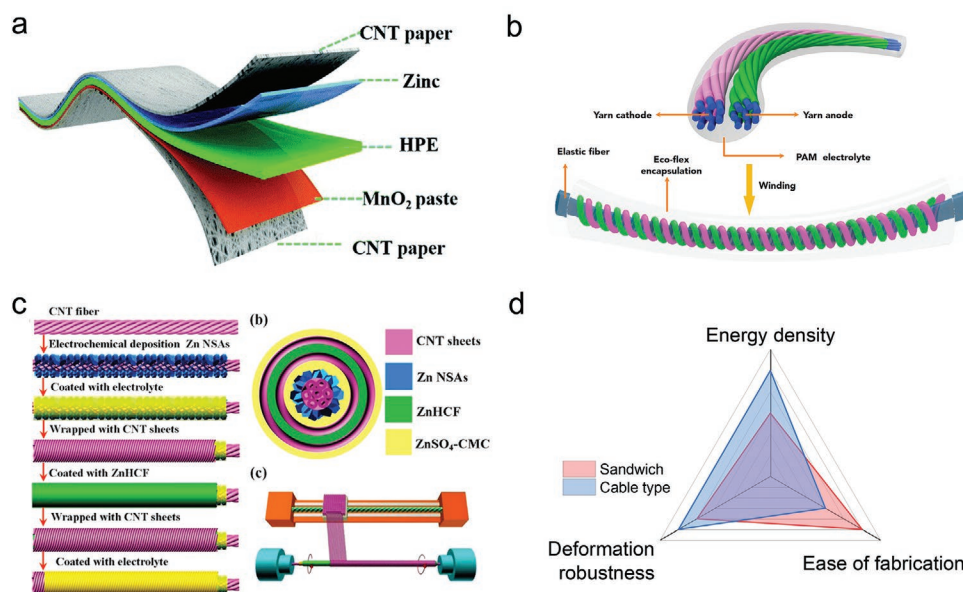


**Figure 16.** a) Sandwich structure. Reproduced with permission.<sup>[38]</sup> Copyright 2018, Royal Society of Chemistry. b) Cable type structure. Reproduced with permission.<sup>[143]</sup> Copyright 2018, American Chemical Society. c) Cable type structure by coating strategy. Reproduced with permission.<sup>[83]</sup> Copyright 2019, American Chemical Society. d) Radar diagram comparing sandwich and cable type structures.

**Table 3.** Summary of materials for current wearable bands.

Brand	Battery capacity [mAh]	System mass [g]	Band materials	Device-specific capacity [mAh g <sup>-1</sup> ]	Straps tensile strength [MPa]
MI band 4	135	22.1	TPSiV thermoplastic elastomers	6.1	15.0
Fitbit inspire	60	20	TA6589K-5 thermoplastic elastomers	3.0	8.0
Huawei band 4 pro	100	25	Silicon strap	4.0	9.0
Samsung band	200	34	Silicon strap	5.9	12.0
Apple watch	750	75	Fluoroelastomer	10.0	13.9
Average				5.79	11.58

electrolyte immersed into highly concentrated 4 M Zn(OTf)<sub>2</sub>, offering a stable and high voltage window of 0.7–2.0 V for Zn/CoFe(CN)<sub>6</sub> batteries. Apart from modulating the concentration, the surfactant such as SDS can expand the electrochemical stability window beyond the limitation of water. The investigation carried out by Qian et al.<sup>[36]</sup> has revealed that by mixing SDS with pristine electrolyte ZnSO<sub>4</sub> and MnSO<sub>4</sub>, the onset potential with the additional SDS at the critical micelle concentration (CMC = 0.8 × 10<sup>3</sup> mol L<sup>-1</sup>) was -1.15 V (vs SHE), which was 0.45 V lower than that of the pristine electrolyte, thus inhibiting HER (Figure 18b). Regarding the cathodes, the shift of voltage from 1.1 to 1.4 V (vs SHE) also prove the capability of suppressing OER. Integrating with cathode Na<sub>2</sub>MnFe(CN)<sub>6</sub>, the battery could achieve a high voltage window up to 2.5 V, attributing to the hydrophobic layer of the SDS, where the hydrophobic group of the SDS are facing to the electrolyte as a high energy barrier for water molecules to transmit through, hence resulting in a higher HER and OER potential. Other organic acids including succinic acid, dicarboxylic acid and tartaric acid<sup>[165]</sup> could also inhibit the HER reaction on the zinc anode because of the presence of polar groups.

Regarding hydrogel electrolytes for ZIBs, although solid-liquid interface between electrodes and electrolyte is the barrier to impede HER and OER, the relatively weak constrain with water molecules is still likely to drive the HER reaction on the anode. Initializing by hydrophilic and hydrophobic performance, a hydrophobic layer can be introduced outside of the hydrogel electrolytes for further investigation, which is consistent with the exploration by Wang et al.<sup>[166]</sup> who developed a hydrophilic layer above the anode in the AZIBs. Meanwhile, besides the hydrophilic groups in the hydrogel framework, it is worth mixing the solid polymer or highly concentrated salt solutions in the structure thus inhibiting the formation of byproducts resulting from the reaction between Zn<sup>2+</sup> and OH<sup>-</sup>. Apart from the enhancement of the voltage window by modulating the hydrogel electrolyte, it is notable that the development of hybrid redox flow battery with the ZIBs offers an alternative approach to increase the operational voltage. As shown in Figure 18c, decoupling the two half-cell reactions between acidic or mild MnO<sub>2</sub> and alkaline Zn redox reactions in the electrolyte, the hybrid battery can reach an open circuit potential of 2.83 V.<sup>[167–170]</sup> Inspired by the redox flow battery, a novel hydrogel electrolyte storing both acid and alkaline aqueous solutions is essential to deliver a comparable high voltage battery for flexible devices.

### 9.3. Cathode–Electrolyte Interfacial Interaction

The voltage window is highly related to the electrode–electrolyte interfaces (EEI) consisting of the cathode–electrolyte interface (CEI) and anode–electrolyte interface (AEI). For SPEs with organic solutions, on the cathode side, once the potential is lower than the highest occupied molecular orbital (HOMO) level of the electrolyte, there will be an oxidation of the electrolyte at the CEI resulting in a polarized electrode; while on the anode side, if the potential is higher than the lowest unoccupied molecular orbital (LUMO) level of the electrolyte, there will be a reduction of the electrolyte at AEI forming a solid-liquid interface (SEI).<sup>[171]</sup> However, owing to the presence of aqueous solutions, the redox couple for the reduction is H<sub>2</sub>O/H<sub>2</sub> (HER) at the anode; and that for oxidation O<sub>2</sub>/H<sub>2</sub>O (OER) at the cathode (Figure 19b). Regarding the CEI, the hydrogel electrolyte serves as the physical barrier impeding the dissolution of the cathode materials, especially for Mn-based and PBA-based cathode materials. However, there are still limited studies investigating the CEI in flexible ZIBs. Desolvation/adsorption mechanism could be essential to unravel the interaction at the interface. Deduced from the desolvation mechanism proposed by Liang<sup>[172]</sup> and Nazar<sup>[173]</sup> who investigated the desolvation of Zn<sup>2+</sup> in both aqueous and non-aqueous electrolytes, there would be a higher activation energy associated with the nonaqueous interfacial charge transfer process for the SPE compared with the hydrogel electrolyte. For hydrogel electrolytes, Zn<sup>2+</sup> will be solvated and form a [Zn(OH)<sub>2</sub>]<sub>6</sub><sup>2+</sup> sheath, the most stable solvation shell in the aqueous electrolyte. During discharging, OH<sup>-</sup> at the CEI dissociated from H<sub>2</sub>O will capture Zn<sup>2+</sup> from [Zn(OH)<sub>2</sub>]<sub>6</sub><sup>2+</sup> thus forming [Zn(OH)<sub>n</sub>]<sub>n</sub><sup>2-n</sup>, which accelerates the Zn<sup>2+</sup> desolvation. As shown in Figure 19c, partial [Zn(OH)<sub>n</sub>]<sub>n</sub><sup>2-n</sup> formation is likely combining with an anion in the electrolyte resulting in a layer of Zn<sub>4</sub>SO<sub>4</sub>(OH)<sub>6</sub>·4H<sub>2</sub>O and delivering extra capacity. In contrast, for solid polymer electrolytes, the large impedance and high activation energies attained indicate a larger barrier for nonaqueous Zn<sup>2+</sup> intercalating into cathode materials which results in a low capacity being achieved. Although electrolytes with the sufficient water content exhibit a good capacity, the presence of OH<sup>-</sup> from the water decomposition often induces the formation of Zn(OH)<sub>2</sub> and eventually converts to ZnO at the AEI, which significantly decreases the Zn stripping/plating reversibility.<sup>[164]</sup> Wang et al.<sup>[37,164]</sup> demonstrated that the strong interaction between Zn<sup>2+</sup> and water molecules constitutes a high energy barrier for a solvated Zn<sup>2+</sup>



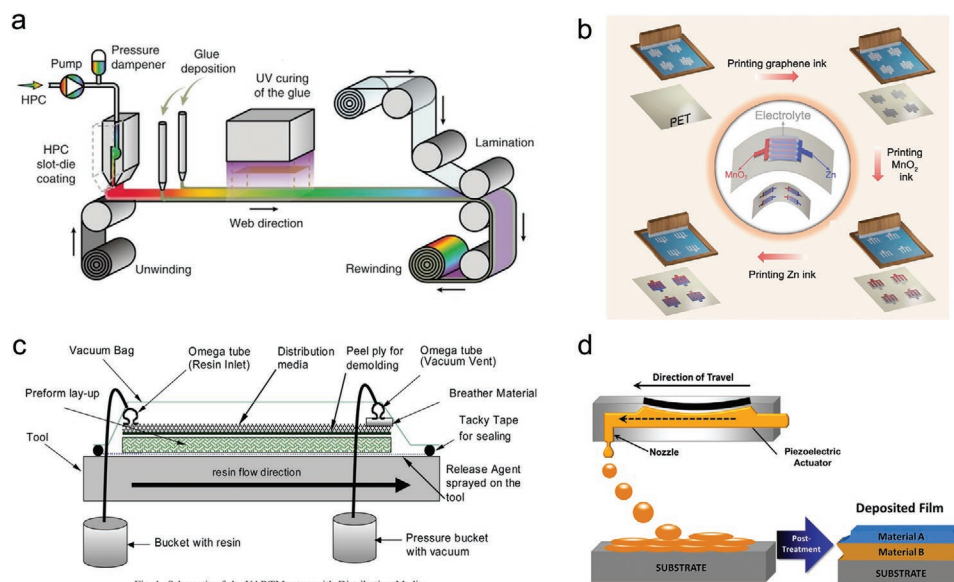


Fig. 1. Schematic of the VARTM setup with Distribution Media.

**Figure 17.** a) Schematic illustration of automated layer-by-layer immersive assembly on flexible substrates using polymer solutions. Movement through positively charged polymer and washing solutions and movement through negatively charged polymer and washing solutions. Reproduced under the terms of the CC-BY Creative Commons Attribution 4.0 International license (<https://creativecommons.org/licenses/by/4.0/>).<sup>[159]</sup> Copyright 2018, The Authors, published by Springer Nature. b) Schematic diagram of screen printing for printed Zn//MnO<sub>2</sub> batteries. Reproduced with permission.<sup>[151]</sup> Copyright 2020, Oxford University Press. c) Schematic illustration of vacuum-assisted resin transfer molding (VARTM) whereby the resin flows into the layout uniformly. Reproduced with permission.<sup>[152]</sup> Copyright 2005, Elsevier. d) Schematic illustration of inkjet printing. Individual ink drops coalesce to form wet layers. Solvent from the wet layer evaporates to form dry layers. These dry layers may serve as substrates for deposition of the next material. After all, layers are deposited, post-printing treatment may be used to remove residual solvent or additives or to cross-link polymers. Reproduced with permission.<sup>[156]</sup> Copyright 2017, Wiley-VCH.

to desolvate and deposit. By introducing highly concentrated aqueous electrolytes, water-in-salt solutions such as 30 m ZnCl<sub>2</sub> and 20 m LiTFSI, [Zn(OH)<sub>2</sub>]<sub>6</sub><sup>2+</sup> can be suppressed by [ZnCl<sub>4</sub>]<sup>2-</sup> and [Zn-TFSI]<sup>+</sup>. As for AEI, less water content could enhance the stability with dendrite free ZIBs. A trade-off design should be considered in polymer electrolytes for flexible ZIBs between the water content with capacity and stability. HBPEs compositing both the water content in hydrogel electrolytes with organic solvent for solid electrolytes would be a possible strategy to guarantee both good stability and reversibility of the zinc anode, and the considerable capacity for cathode materials.

#### 9.4. Anode–Electrolyte Interfacial Interaction

In terms of the AEI interface, Zn plating/stripping is expected with chemical conversion reaction between Zn and Zn<sup>2+</sup>. However, because of the uneven electron and ion distribution at the interface, the inhomogeneous zinc nucleation eventually results in the formation of dendrites as shown in **Figure 20a**. Accompanied by zinc dendrites, there would be a decrease of electron transfer at the interface and the plated Zn prefers depositing on the existing nucleus resulting in “dead zinc” causing a short circuit of AZIBs. For flexible ZIBs, owing to the benefit of the polymer electrolyte, zinc dendrite formation is suppressed by the physical solid–solid interface between the electrolyte and the anode. However, as the water molecules are present in HPEs, HPEs also suffer from water-induced side effects. Refer to **Figure 1a**, HER at the anode not only generate H<sub>2</sub> causing

the battery failure, but the consumption of H<sup>+</sup> causes a pH change at the interface to an alkaline environment forming the insulating material ZnO.<sup>[175,176]</sup>

Strategies employed recently can be categorized into four classes: i) physical modification of anode structures; ii) anode surface coating; iii) novel separator designs; iv) electrolyte modification. Among these, electrolyte modification especially the application of polymer electrolyte will effectively suppress the dendrite growth because of the physical solid–solid interface. Aiming to enlarge the surface area of the zinc anode and minimizing the effect of zinc dendrites, Li et al.<sup>[145]</sup> have deposited the zinc onto the core/shell CC-ZnO@C skeleton synthesized from zeolitic-imidazolate frameworks (ZIF-8). Distinguishing from the zinc plate, the finely crafted skeleton offers a homogeneous charge distribution, hence effectively suppressing zinc dendrite formation (**Figure 20b**). The surface treatment is also another approach where the hydrophobic modulation on the anode surface is approved to suppress the formation of the zinc dendrite. Coating a thin metal-organic framework (MOF) layer on the anode and filling the pores of MOFs with hydrophobic Zn(TFSI)<sub>2</sub>-tris(2,2,2-trifluoroethyl)phosphate (TFEP) organic electrolyte, the hydrophobic solid layer chemically prevents water hydrolysis at the anode resulting in a smooth morphology (**Figure 20c**). Cui et al.<sup>[39]</sup> also created the artificial interface on the zinc surface by constructing a “brightener-inspired” polyamide layer elevating the nucleation barrier and restricting the 2D diffusion of Zn<sup>2+</sup> (**Figure 20d**). The buffer layer of the brightener strongly coordinates with Zn<sup>2+</sup>, improving the electrochemical polarization and the nucleation overpotential. A separator could also be used as a buffer layer; Liu<sup>[177]</sup> developed

**Table 4.** Summary of recent flexible ZIBs in electrolyte, cathode, anode, voltage range, device configuration and fabrication, capacity, cycling life, energy density and power density.

Electrolytes	Cathodes	Anodes	Voltage ranges	Device configurations & fabrications	Capacity	Cycling life	Energy density	Power density	Ref
PEO (ZnCl <sub>2</sub> +TiO <sub>2</sub> )	—	—	—	—	—	—	—	—	[54]
PEO (ZnBr <sub>2</sub> )	MnO <sub>2</sub> @Ni	Zn foil (0.25mm)	—	—	—	—	—	—	[52]
PVDF ([EMIM] BF <sub>4</sub> + Zn(BF <sub>4</sub> ) <sub>2</sub> )	CoHCF@ carbon cloth	Deposited Zn@ carbon cloth	0.5–2.05 V	Sandwich (LBL)	149.53 mAh g <sup>-1</sup> (0.2 A g <sup>-1</sup> )	90% capacity retention (2 A g <sup>-1</sup> , 30 000 cycles)	—	—	[73]
PVA (ZnCl <sub>2</sub> +MnSO <sub>4</sub> )	MnO <sub>2</sub> @PEDOT	Deposited Zn@ carbon cloth	1.0–1.8 V	Sandwich (LBL)	282.4 mA h g <sup>-1</sup> (0.37 A g <sup>-1</sup> )	77.7% capacity retention (1.86 A g <sup>-1</sup> , 300 cycles)	504.9 Wh kg <sup>-1</sup>	8.6 kW kg <sup>-1</sup>	[41]
PVA (ZnCl <sub>2</sub> +MnSO <sub>4</sub> )	MnO <sub>2</sub> @nitrogen doped carbon cloth	Deposited Zn@ carbon cloth	1.0–1.8 V	Sandwich (LBL)	353 mA h g <sup>-1</sup> (0.5 A g <sup>-1</sup> )	86.7% capacity retention (1.0 A g <sup>-1</sup> , 1000 cycles)	440 Wh kg <sup>-1</sup>	7.9 kW kg <sup>-1</sup>	[160]
PVA (ZnCl <sub>2</sub> )	MnO <sub>2</sub> @CNT fiber	Zn wire	1.0–2.0 V	Cable (Electrolyte immerse sol–gel transition)	290 mAh g <sup>-1</sup> (0.1 A g <sup>-1</sup> )	75% capacity retention (1.0 A g <sup>-1</sup> , 300 cycles)	360 Wh kg <sup>-1</sup>	2.0 kW kg <sup>-1</sup>	[93]
PVA (KOH)	AgO@silver mesh	Zn@silver mesh	0.8–1.6 V	Sandwich (LBL)	25 mAh g <sup>-1</sup> (200 μA cm <sup>-2</sup> )	97% capacity retention (200 μA cm <sup>-2</sup> , 20 cycles)	—	—	[161]
PANa (KOH + Zn(CH <sub>3</sub> COO) <sub>2</sub> )	NiCo@Au@CNT paper	Zn@Au@CNT paper	1.2–2.0 V	Sandwich (LBL)	79 mAh g <sup>-1</sup> (28 A g <sup>-1</sup> )	86% capacity retention (14 A g <sup>-1</sup> , 340 cycles)	—	—	[99]
PANa (KOH + Zn(CH <sub>3</sub> COO) <sub>2</sub> )	CoSe <sub>2,x</sub> @carbon cloth	Zn foil	0.75–2.05 V	Sandwich (LBL)	—	84% capacity retention (10 mA cm <sup>-2</sup> , 4200 cycles)	—	—	[100]
PAA (KOH)	MnO <sub>2</sub> @Cu net	Zn slurry@ Cu net	—	Sandwich (LBL)	280 mAh g <sup>-1</sup> (1 C)	—	—	—	[97]
Fumed silica (ZnSO <sub>4</sub> )	Zinc orthovanadate@ graphene foam	Zn-array@ graphene foam	0.4–1.5 V	Sandwich (LBL)	204 mAh g <sup>-1</sup> (0.5 C)	89% capacity retention (20 C, 2000 cycles)	115 Wh kg <sup>-1</sup>	5.1 kW kg <sup>-1</sup>	[40]
Aqueous Zn(CF <sub>3</sub> SO <sub>3</sub> ) <sub>2</sub>	freestanding rGO/VO <sub>2</sub>	Zn foil	0.3–1.3 V	Sandwich (LBL)	260 mAh g <sup>-1</sup> (0.2 A g <sup>-1</sup> )	99% capacity retention (4 A g <sup>-1</sup> , 1000 cycles)	65 Wh kg <sup>-1</sup>	7.8 kW kg <sup>-1</sup>	[162]
PAM (ZnSO <sub>4</sub> +CoSO <sub>4</sub> )	Co(III)-Co <sub>3</sub> O <sub>4</sub> @ carbon cloth	Deposited Zn@ carbon cloth	0.8–2.3 V	Sandwich (LBL)	52 m h g <sup>-1</sup> (8 A g <sup>-1</sup> )	94.6% capacity retention (2 A g <sup>-1</sup> , 2000 cycles)	360.8 Wh kg <sup>-1</sup>	—	[42]
PAM (ZnSO <sub>4</sub> +MnSO <sub>4</sub> )	MnO <sub>2</sub> @CNT yarn	Deposited Zn@ CNT yarn	1.0–2.0 V	Double-helix cable (Electrolyte immerse sol–gel transition)	302.1 mAh g <sup>-1</sup> (60 mA g <sup>-1</sup> )	98.5% capacity retention (2 A g <sup>-1</sup> , 500 cycles)	53.8 mWh cm <sup>-3</sup>	—	[143]
Starch-g-PAM (ZnSO <sub>4</sub> )	MoS <sub>2</sub> @carbon cloth	Deposited Zn@ carbon cloth	0.3–1.5 V	Sandwich (LBL)	199.3 mAh g <sup>-1</sup> (0.1 A g <sup>-1</sup> )	97.7% capacity retention (1.0 A g <sup>-1</sup> , 500 cycles)	148.2 Wh kg <sup>-1</sup>	—	[85]

**Table 4.** Continued.

Electrolytes	Cathodes	Anodes	Voltage ranges	Device configurations & fabrications	Capacity	Cycling life	Energy density	Power density	Ref
Gelatin (ZnSO <sub>4</sub> +Li <sub>2</sub> SO <sub>4</sub> )	LiMn <sub>2</sub> O <sub>4</sub> @stainless steel foil	Zn foil	1.4–2.2 V	Sandwich (LBL)	109.7 mAh g <sup>-1</sup> (0.02 A g <sup>-1</sup> )	90% Capacity retention (0.025 A g <sup>-1</sup> , 100 cycles)	—	—	[46]
Gelatin (Zn(CF <sub>3</sub> SO <sub>3</sub> ) <sub>2</sub> )	Expanded V <sub>2</sub> O <sub>5</sub> @stainless steel mesh	Zn/stainless steel mesh	0.3–1.6 V	Sandwich (LBL)	361 mAh g <sup>-1</sup> (0.1 A g <sup>-1</sup> )	85% capacity retention (1.0 A g <sup>-1</sup> , 300 cycles)	156 Wh kg <sup>-1</sup>	6.9 kW kg <sup>-1</sup>	[87]
Gelatin-g-PAM (ZnSO <sub>4</sub> +MnSO <sub>4</sub> )	MnO <sub>2</sub> @CNT paper	Deposited Zn@ CNT paper	0.9–2.0 V	Sandwich (LBL)	306 mAh g <sup>-1</sup> (2.7 A g <sup>-1</sup> )	97% capacity retention (2.7 A g <sup>-1</sup> , 1000 cycles)	6.18 mW h cm <sup>-2</sup>	148.2 mW cm <sup>-2</sup>	[38]
Xanthan (ZnSO <sub>4</sub> +MnSO <sub>4</sub> )	MnO <sub>2</sub> @CNT film	Zn foil	1.0–2.0 V	Sandwich (LBL)	260 mAh g <sup>-1</sup> (1 C)	90% capacity retention (1 C, 330 cycles)	364 Wh kg <sup>-1</sup>	2.5 kW kg <sup>-1</sup>	[47]
Guar gum (ZnSO <sub>4</sub> +MnSO <sub>4</sub> )	MnO <sub>2</sub> /rGO@ carbon cloth	Deposited Zn@ carbon cloth	1.0–1.9 V	Sandwich (LBL)	308.2 mAh g <sup>-1</sup> (0.3 A g <sup>-1</sup> )	85% capacity retention (6.0 A g <sup>-1</sup> , 2000 cycles)	416 Wh kg <sup>-1</sup>	7.8 kW kg <sup>-1</sup>	[48]
CMC (ZnCl <sub>2</sub> +NH <sub>4</sub> Cl)	PANI@cellulose papers	Deposited Zn@ graphene paper	0.7–1.7 V	Sandwich (LBL)	142.3 mAh g <sup>-1</sup> (0.2 A g <sup>-1</sup> )	84.7% capacity retention (4.0 A g <sup>-1</sup> , 1000 cycles)	67.8 Wh kg <sup>-1</sup>	3.34 kW kg <sup>-1</sup>	[50]
CMC (ZnSO <sub>4</sub> )	ZnHCF aligned with CNT sheets	Zn nanosheet arrays	1.0–2.4 V	Coaxial cable (LBL: In situ coating)	100.2 mAh cm <sup>-3</sup> (0.1 A cm <sup>-3</sup> )	91.8% capacity retention (0.1 A cm <sup>-3</sup> , 200 cycles)	126.9 mWh cm <sup>-3</sup>	1.9 W cm <sup>-3</sup>	[83]
Sodium alginate (ZnSO <sub>4</sub> +MnSO <sub>4</sub> )	α-MnO <sub>2</sub> @CNT paper	Deposited Zn@ CNT paper	0.9–1.9 V	Sandwich (LBL)	300.4 mAh g <sup>-1</sup> (0.11 A g <sup>-1</sup> )	82% capacity retention (0.88 A g <sup>-1</sup> , 500 cycles)	—	—	[49]
κ-Carrageenan (ZnSO <sub>4</sub> +MnSO <sub>4</sub> )	MnO <sub>2</sub> /rGO@ carbon cloth	Deposited Zn@ carbon cloth	1.0–1.9 V	Sandwich (LBL)	291.5 mA h g <sup>-1</sup> (0.15 A g <sup>-1</sup> )	80% capacity retention (6.0 A g <sup>-1</sup> , 450 cycles)	400 Wh kg <sup>-1</sup>	7.9 kW kg <sup>-1</sup>	[51]
PAM + F77 (Zn(CF <sub>3</sub> SO <sub>3</sub> ) <sub>2</sub> )	CoFe(CN) <sub>6</sub> @CNT paper	Zn wire	0.7–2.0 V	Cable (Electrolyte immerse sol-gel transition)	171.64 mAh g <sup>-1</sup> (0.2 A g <sup>-1</sup> )	93.4% capacity retention (3 A g <sup>-1</sup> , 2000 cycles)	—	—	[13]
PHE (ZnSO <sub>4</sub> +Li <sub>2</sub> SO <sub>4</sub> )	LiFePO <sub>4</sub> @stainless steel foil	Zn powder@ stainless steel foil	0.9–1.7 V	Sandwich (LBL)	169 mAh g <sup>-1</sup> (0.1 C)	90% capacity retention (0.5 C, 300 cycles)	—	—	[44]
PAM+EG (ZnSO <sub>4</sub> +MnSO <sub>4</sub> )	α-MnO <sub>2</sub> @CNT paper	Electroplating zinc@ nickel–copper cloth	0.9–1.9 V	Sandwich (LBL)	226 mA h g <sup>-1</sup> (0.2 A g <sup>-1</sup> , –20 °C)	74.54% capacity retention (2.4 A g <sup>-1</sup> , 600 cycles)	32.68 mWh cm <sup>-3</sup>	—	[43]
PNA (ZnSO <sub>4</sub> +MnSO <sub>4</sub> )	α-MnO <sub>2</sub> @CNT paper	Zn foil	0.9–1.8 V	Sandwich (LBL)	145 mA h g <sup>-1</sup> (0.1 A g <sup>-1</sup> )	—	—	—	[45]
PVA–PAA (KOH+ZnO)	MnO <sub>2</sub> @CNT paper	Zn@CNT paper	0.7–1.5 V	Sandwich (LBL)	283 mAh g <sup>-1</sup> (0.3 mA cm <sup>-2</sup> )	—	289 Wh kg <sup>-1</sup>	—	[131]
PEGDGE (Zn(CF <sub>3</sub> SO <sub>3</sub> ) <sub>2</sub> )	β-MnO <sub>2</sub> @carbon cloth	Zn@carbon cloth	0.8–2.0 V	Sandwich (LBL)	177 mAh g <sup>-1</sup> (0.1 A g <sup>-1</sup> )	Capacity retention 85% (0.5 A g <sup>-1</sup> , 300 cycles)	—	—	[163]

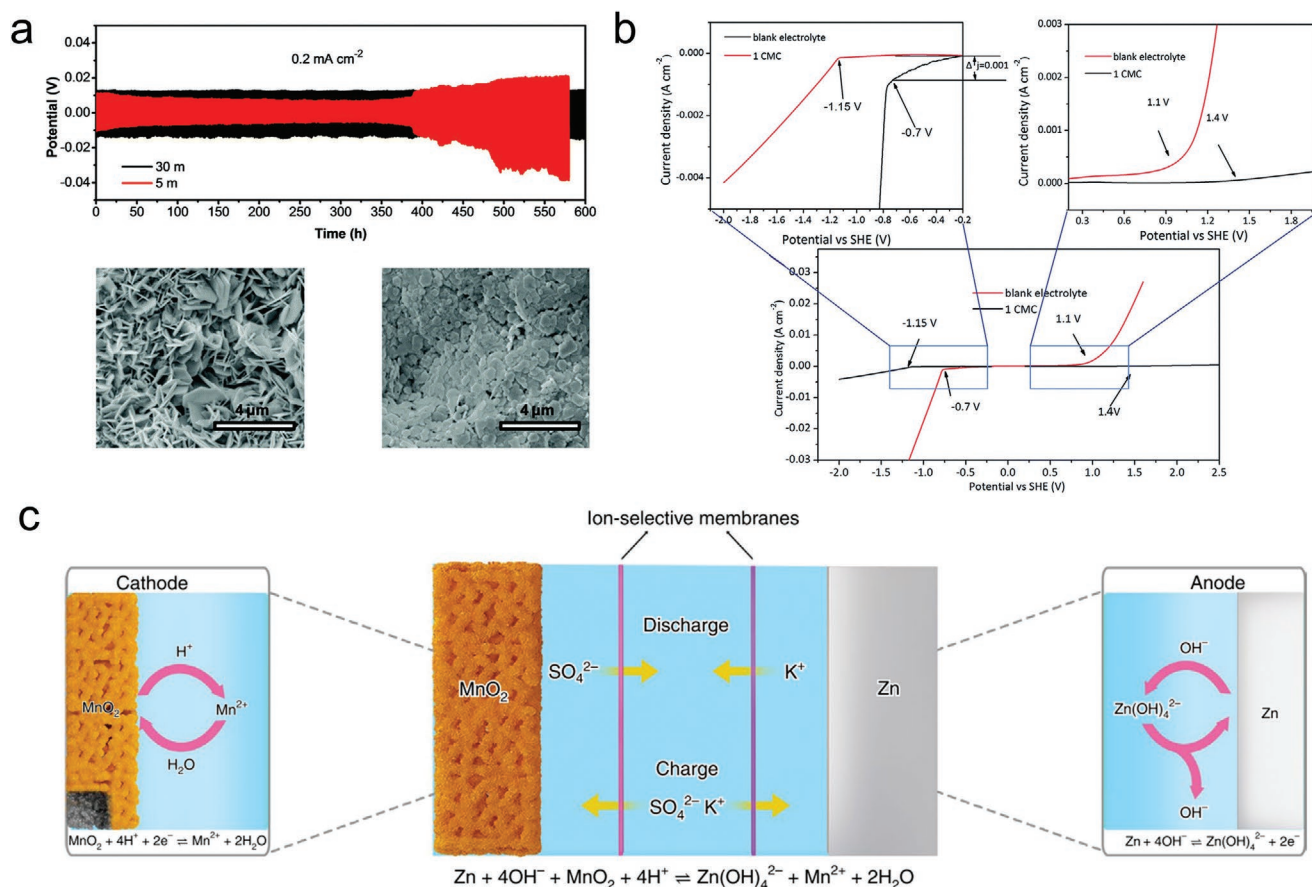


**Figure 18.** a) Characterization of the Zn metal electrode with “water-in-salt” ZnCl<sub>2</sub> electrolytes by cycling test and the post-SEM images of the Zn electrodes. Reproduced with permission.<sup>[37]</sup> Copyright 2018, Royal Society of Chemistry. b) Surfactant widens the electrochemical window of an aqueous electrolyte for better rechargeable aqueous sodium/zinc battery investigated by the measurements of linear sweep voltammetry on titanium grid electrodes versus Ag/AgCl at 10 mV s<sup>-1</sup>. Reproduced with permission.<sup>[36]</sup> Copyright 2017, Royal Society of Chemistry. c) Working mechanisms for hybrid electrolyte-decoupling Zn–MnO<sub>2</sub> batteries. Reproduced with permission.<sup>[167]</sup> Copyright 2020, The Authors, published by Springer Nature.

a novel separator where graphene oxide (GO) was decorated on a glass fiber (GF) separator. Compared with GF, the GO-modified separator results in the uniform nucleation of Zn<sup>2+</sup>. Lee et al.<sup>[178]</sup> also designed a multifunctional separator with PAN-based cation exchange membrane which can selectively and effectively transport cations but block anions, achieving a prolonged cycle life (350 cycles) of the Zn//Zn test. Moreover, electrolyte additives such as “water-in-salt” electrolytes also suppress the growth of zinc dendrite. Hydrogel electrolytes, where the solid–liquid interface is in between, are beneficial to generate the physical barrier for water loss from the polymer framework. Especially for polyelectrolyte hydrogel electrolyte; additional electrostatic effects induced by the charged groups immobilize a uniform zinc plating at the interface. Although strategies reported are essential to inhibit the inevitable zinc dendrite, the energy storage mechanism along the AEI is still not fully understood. Literally, different from the SPE batteries, the preconceived understanding that solid–liquid interfaces are located between the hydrogel electrolyte and the electrodes is not acceptable. Indeed, there is a water layer presenting between the anode and the hydrogel electrolyte. The neglected water region reduces the surface resistance of the hydrogel electrolyte ZIBs via the enhancement of the wettability of the

zinc anode, while the suppression of the zinc dendrite growth is limited. Nazarov et al.<sup>[179]</sup> have investigated the zinc/polymer interface by utilizing electrochemical impedance spectroscopy (EIS) and scanning Kelvin probe (SKP), where the potential drops across the zinc/polymer interface is significantly related to the humidity. Hence, further study is suggested to exploit the influence of the water layer at the interface.

## 9.5. Ionic Conductivity

As summarized in Table 2, compared to hydrogel electrolytes, solid polymer electrolytes suffer from low ionic conductivity which is in the magnitude of 10<sup>-3</sup>–10<sup>-6</sup> S cm<sup>-1</sup> without additives. Considering the desolvation mechanism mentioned in Section 9.3, ZIBs with nonaqueous electrolytes exhibit high desolvation energy resulting in high charge transfer resistance and low ionic conductivity. Introducing organic/inorganic additives as indicated in Table 2, ionic conductivity can be improved with the expanded free volume for segmental motion in SPEs. Ionic liquids such as [EMIM]BF<sub>4</sub> and EMIMTFSI could further enhance the ionic conductivity, whereas the high cost of ionic liquids restricted its application for mass production. The

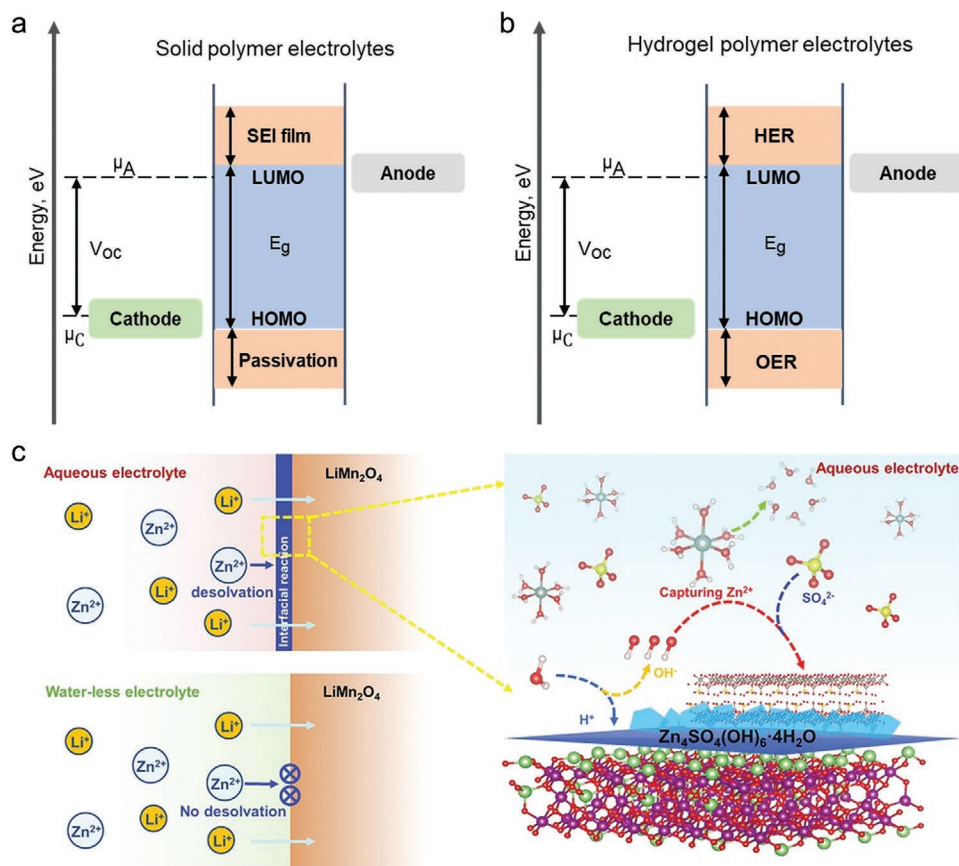


**Figure 19.** a) Schematic open-circuit energy diagram for solid polymer electrolytes. b) Schematic open-circuit energy diagram for hydrogel polymer electrolytes. (e.g., the electrochemical stability window;  $\mu_A$ : redox potential of the anode;  $\mu_C$ : redox potential of the cathode. a,b) Reproduced with permission.<sup>[174]</sup> Copyright 2020, Royal Society of Chemistry. c) Schematic illustration of the cathode/electrolyte interface in an aqueous and waterless electrolyte with desolvation mechanism. Reproduced with permission.<sup>[172]</sup> Copyright 2020, Wiley-VCH.

ionic conductivity for hydrogel electrolytes is highly related to the water content. Zhi<sup>[180]</sup> has observed that with an increase of the water content from 66% to 92.2%, the hydrogel exhibit a higher ionic conductivity and lower interfacial resistance in the PAM-based hydrogel electrolytes. However, as discussed in Section 9.3, high water content would generate a higher energy barrier for  $\text{Zn}^{2+}$  to desolvate and deposit. Meanwhile, accompanied by the high water content, byproducts caused by HER at the AEI decreases the reversibility of zinc stripping/plating. Therefore, the suitable water content in hydrogel electrolytes is required with the compromise between the ionic conductivity and battery stability. Regarding the ionic conductivities and the cost as listed in Table 1, PAM and PVA are the most cost-effective polymer hosts for hydrogel electrolytes. It is suggested that hybrid polymer electrolytes should continue to be developed with the skeleton of PAM and PVA.

## 9.6. Hydrogel Ageing Issue

Under weak bonding with water molecules, hydrogel electrolytes ZIBs exhibit a high Coulombic efficiency greater than 95%, while the capacity retention is often less than that of AZIBs. Employed under an electrical field, a hydrogel electrolyte is likely

to suffer from an ageing issue. We investigated the ageing effect for polymer electrolytes in ZIBs by a continuous EIS test of Zn/SPE/Zn. Recording the bulk resistance ( $R_b$ ) and interface resistance ( $R_f$ ) over a 400-hour EIS test,  $R_f$  maintains constant for over 200 hours for the anti-ageing polymer electrolyte, twice that of conventional hydrogel electrolytes, while  $R_b$  remains constant for 400 and 170 hours for polymer electrolyte and hydrogel electrolyte respectively.  $R_f$  gradually increases with time revealing that the surface passivation film on zinc metal grows in thickness which impedes the stripping/plating process. Owing to the densification of the hydrogel electrolyte, it would be expected that the loss of solvent is more significant resulting in a rapid change in  $R_f$ . A further in situ investigation is required to understand the ageing issue and propose relevant solutions.

## 9.7. Mechanical Strength Enhancement

For flexible ZIBs, the deformation endurance is another important parameter apart from electrochemical properties. Wei et al.<sup>[180]</sup> proposed structural design requirements for flexible energy storage devices. However, with the application of hydrogel or HBPEs, there are differences compared with solid polymer-based flexible batteries. For a typical sandwich device,

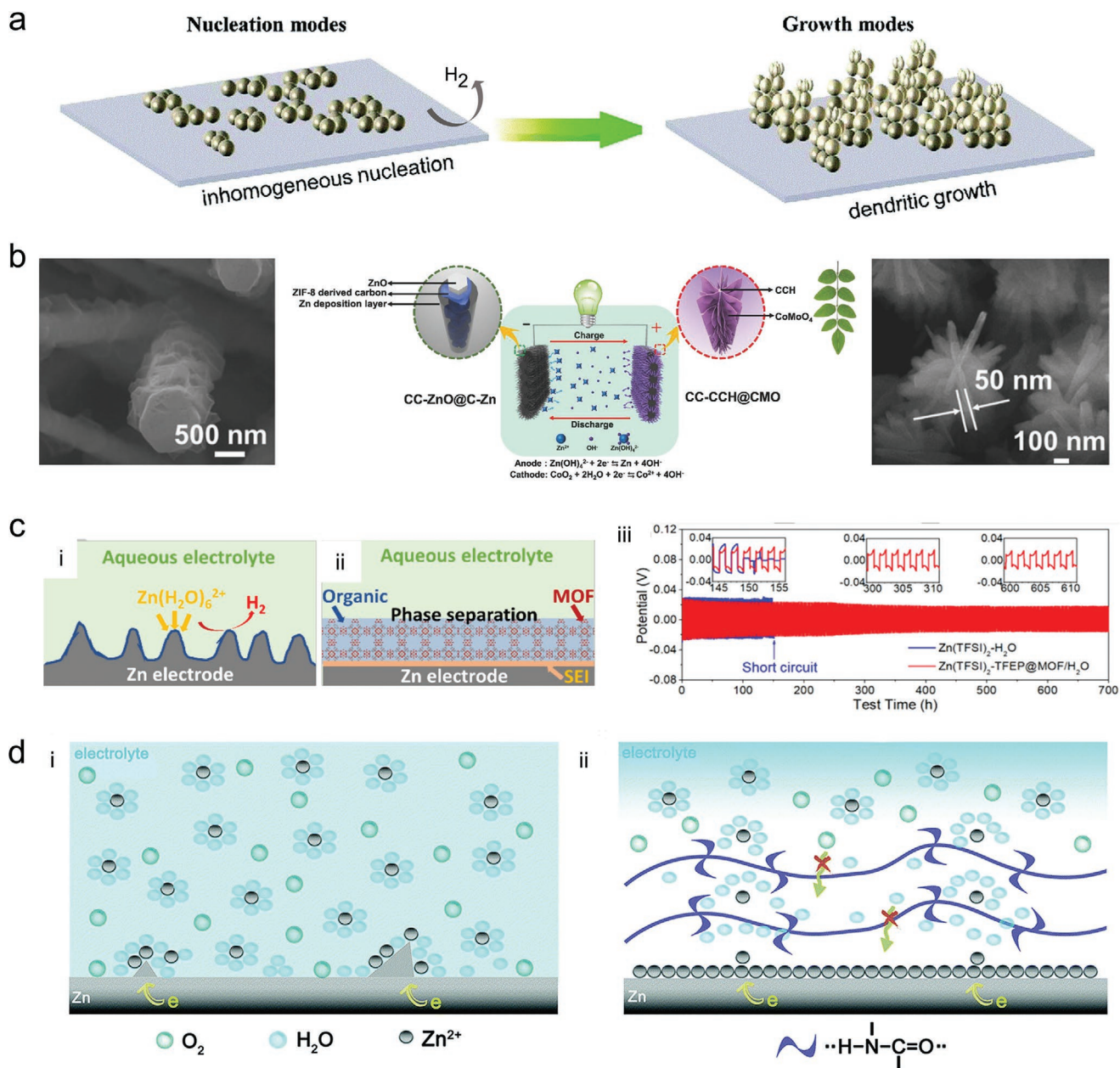


**Figure 20.** a) The inhomogeneous nucleation and dendritic growth of the zinc anode at the anode–electrolyte interface. Reproduced with permission.<sup>[176]</sup> Copyright 2020, Royal Society of Chemistry. b) Schematic illustration of the Zn–Co full battery using the finely crafted 3D CC-ZnO@C-Zn anode and CC-CCH@CMO cathode, together with the redox reactions during charge–discharge processes. Reproduced with permission.<sup>[145]</sup> Copyright 2018, Wiley-VCH. c) Schematic illustration of the surface structure and surface reaction of hydrophobic organic electrolyte protected Zn anodes, and the plating/stripping performance. Reproduced with permission.<sup>[166]</sup> Copyright 2020, Wiley-VCH. d) The bare Zn and the coated Zn, suggesting the role of the PA layer in the inhibition of side reactions. Reproduced with permission.<sup>[39]</sup> Copyright 2019, Royal Society of Chemistry.

the laminated components suffer from different bending strains during bending, where the bottom laminate is under tension and the top laminate is under compression if there is a force perpendicularly acted on the top of the device. The strain in the convex surface can be calculated based on the distance to the neutral plane and the curvature radius as the equation below:

$$\varepsilon = \frac{b}{R} \quad (6)$$

As shown in **Figure 21a**, to simplify the parameters measured during the bending experiment, end-to-end distance  $L$  and bending angle  $\theta$  are introduced.  $L$  is the parameter which can describe the bending state regardless of the shape of the device;  $\theta$  determines the rotating angle of the moving end, and  $R$  is the most appropriate parameter to determine the bending state. Most flexible devices reported exhibit stable capacity retention under different bending states based on this criteria.<sup>[83,87,90,181]</sup> However, the adhesion between polymer

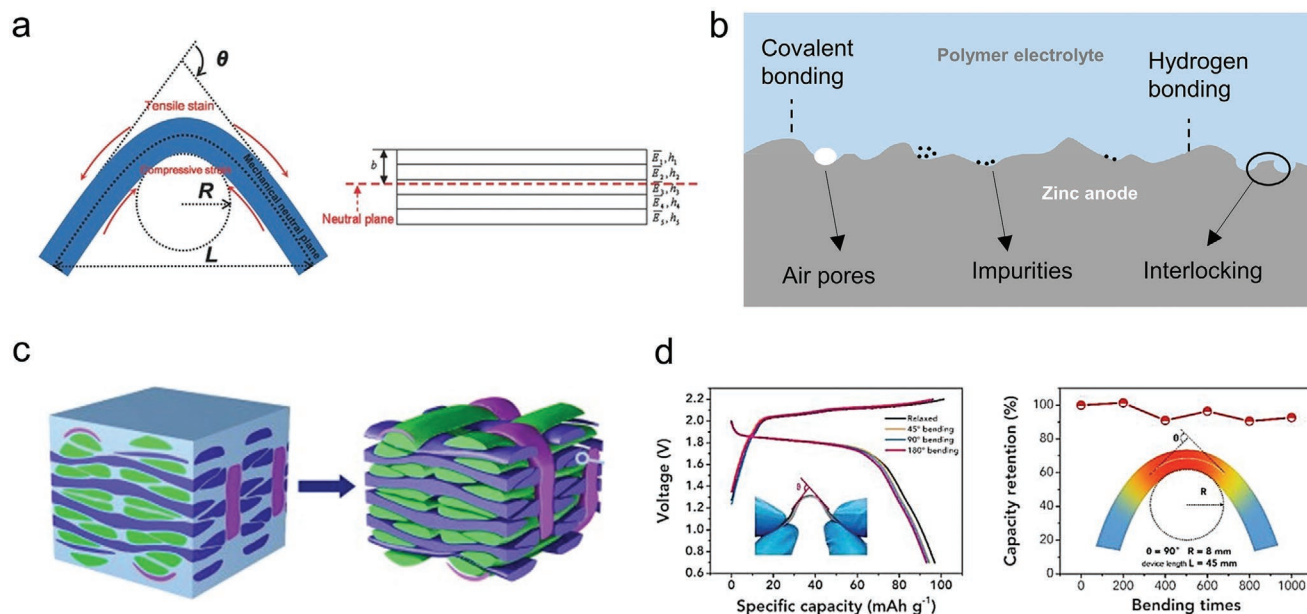


**Figure 21.** a) Bending mechanics of film-on-substrate system ( $L$ : the end-to-end distance along the bending direction;  $\theta$ : the bending angle;  $R$ : the bending radius of curvature.) Reproduced with permission.<sup>[181]</sup> Copyright 2017, Wiley-VCH. b) Adhesive bonding for polymer electrolyte to zinc foil. c) Adhesive bonding for polymer electrolyte to woven carbon cloth. b,c) Reproduced with permission.<sup>[184]</sup> Copyright 2013, Elsevier. d) charging/discharging curves for flexible ZIBs under different bending angles. (Bending radius  $R = 8$  mm, device length  $L = 45$  mm). Reproduced with permission.<sup>[90]</sup> Copyright 2019, Wiley-VCH.

electrolytes and electrodes is the determining factor that affects the flexural strength and the tensile strength.<sup>[180]</sup> As summarized in Table 4, most of electrode substrates for zinc anodes are zinc foils and carbon cloth. In terms of zinc foils, adhesive bonding between polymer electrolytes and the metal surface are formed by the mechanical interlocking, covalent bonding, hydrogen bonding and electrostatic forces (Figure 21b). These adhesive forces have a direct correlation with the contact surface. For the woven carbon cloth (Figure 21c), a larger area of the contact surface is achieved by the polymer resin immersing into the pores. Hence, for a small curvature radius, zinc foil is likely delaminated from the laminate compared with the woven carbon cloth. In consideration of the electrochemical performance, it is necessary to evaluate electrochemical properties under different curvature radius. For the electrodes with metals as the substrates such as zinc foils and stainless-steel foils, because of the less adhesion, metal substrates are likely delaminated from the laminate interface causing the open circuit. Cui et al.<sup>[44]</sup> have fabricated the flexible ZIBs with stainless-steel foils as substrates integrated with the cathode  $\text{LiMn}_2\text{O}_4$ , for which the capacity has degraded from 65 to 30  $\text{mAh g}^{-1}$  at 50  $\text{mA g}^{-1}$  under 100 kPa folding stress (Figure 10c-iii). After applying thermoresponsive HPEs, the interfacial wettability can be refreshed during the cooling process hence recovering the capacity delivering 65  $\text{mAh g}^{-1}$ . For woven carbon cloth as the substrate, the delamination is not likely to happen. Moreover, the application of hydrogel electrolyte even enhances the wettability at the EEI, hence the capacity could still maintain above 92% after bending at 90° for 1000 times as reported by Liu<sup>[90]</sup> (Figure 21d). However, the flexible device with carbon cloth as the substrates can merely maintain the folding stress.

Therefore, it is essential to exploit systematically regarding the adhesive bonding between different polymer electrolytes and substrates at the interface. A potential strategy compromising a good flexural strength and a low capacity fading could be the novel structure design of the substrates, such as controlling the woven structure of the carbon cloth and the porous structure of the metal foam.

Attributed to the good ductility of hydrogel electrolytes, flexible ZIBs could deliver stable capacity during bending or twisting. HPEs exhibit a high stretchability for which a high stretchability up to 3000% strain can be reached for PAM,<sup>[143]</sup> while the tensile strength is too low to satisfy the commercial requirement, where there is only 54 kPa for PAM.<sup>[182,183]</sup> Therefore, the enhancement in tensile strength is significant for the commercialization of flexible ZIBs. As shown in Table 2, few additives from polysaccharides have been applied to enhance the strength by evaluating the chemical crosslinking, however, the improvement is still limited to less than 1 MPa.<sup>[49]</sup> As reported, there is no influence of electrochemical properties by the limited improvement of the mechanical strength. HPEs are normally utilized as both electrolytes and the separator, whereas the improvement of tensile strength for polymer itself is restricted. A strategy to satisfy the requirement of tensile strength is to design a novel separator, such as grafting hydrogel electrolytes on PAN membrane. By grafting PAM and gelatin copolymer on a PAN membrane (Figure 11a), the tensile stress has been improved up to 7 MPa.<sup>[38]</sup> Physically adding other separators, the skeleton of PAN or glass fiber fabrics can sustain the hydrogel electrolytes with the additional load bearings. The chemical crosslinking is another method. By introducing epoxy in flexible ZIBs, carbon cloth substrates can be reinforced

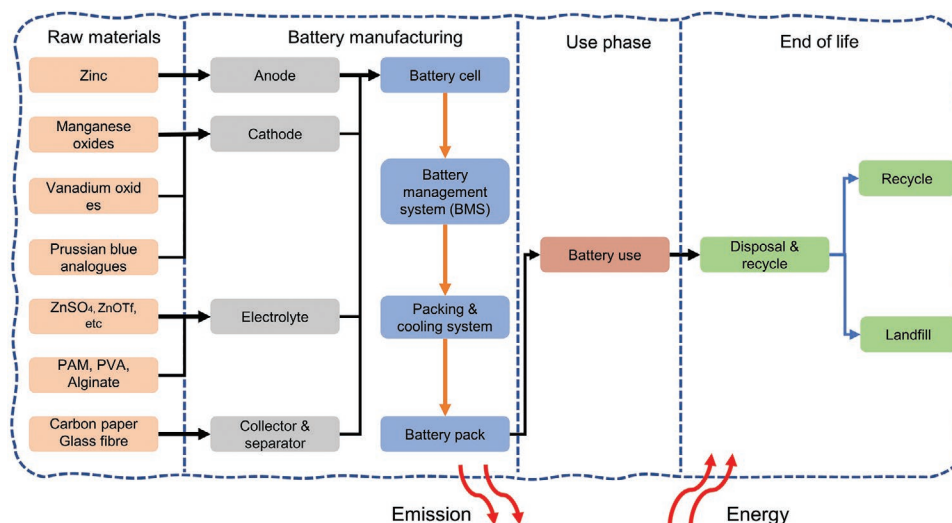


**Figure 22.** General life cycle of flexible ZIBs.

exhibiting a superior tensile strength above 1 GPa.<sup>[148]</sup> Until now, there is no comprehensive study investigating the capacity decay with the tensile test, hence the relationship between the mechanical tensile test and electrochemical performances of the devices should be exploited for further study. As a prediction, under the tensile test, there would be a great impact on the structural integration and capacity retention. However, because of the large plastic zone of hydrogel electrolytes after the yield point, hydrogel electrolytes are expected to fail at last protecting the device from the short-circuit. With further investigation in mechanical performance, the ranking index mentioned ahead could also contain the effect of flexural and tensile strengths.

### 9.8. Life-Cycle Assessment

Life cycle assessment is a methodology assessing environmental impacts associated with entire stages of the life cycle including the raw material processing, the production of batteries, distribution and transportation, use of batteries, recharging of battery and maintenance and final disposal/recycling<sup>[185]</sup> (Figure 22). Although the full industrial line is still absent, with the developing progress of the flexible ZIB, life-cycle assessment is required to be prepared along with the commercialization progress, especially the recycling sector. Zhang, Lu et al.<sup>[186]</sup> recycled zinc from Zn–Mn battery waste and prepared nano-Zn oxide by evaporation and separation with controlled oxidation, where 98.99% recovery efficiency was achieved for zinc. Also for cathode materials, manganese oxides can be recycled under thermal treatment at 900 °C.<sup>[187]</sup> For HPEs, the biocompatibility results in a green environmental friendly recycle economy, which is based on sustainable and clean energy. The application for fluorine-containing SPEs such as polytetrafluoroethylene (PTFE) based polymer electrolytes, however, is more difficult to dispose at the end of the life of batteries. Hence, life cycle assessment is necessary to be covered in the design of the flexible ZIBs.

## 10. Conclusion

There is no doubt that the increasing demand for wearable electronics and implanted health monitoring have accelerated the development of flexible ZIBs from concept to experimental demo in the recent half-decade. Owing to the cost-effectiveness, higher volumetric energy density and the robustness and easiness in fabrication, flexible ZIBs are believed to be the substitutes of flexible LIBs. Most flexible ZIBs reported have already exhibited superior electrochemical properties under deformations, while some real issues such as ageing issue, mechanical strength and the voltage issue still restrict their progress for commercialization. To follow the pace of commercialization of flexible ZIBs, realistic issues facing in the application scenarios, such as the temperature, humidity, and external force, should be considered in the experiments, not merely focusing on the electrochemical performance. The ranking index aforementioned could be utilized as the determining factor for commercialization. Under the same testing reference, data analysis such as clustering and materials predicting, it is possible to evaluate and predict the practical results from micro to macro-scales. Hence, this review is not just a comprehensive summary of current polymer materials, electrolytes, and technologies but provides an insight from lab research to industry speeding the future development of flexible ZIBs.

## Acknowledgements

The authors would like to thank the Engineering and Physical Sciences Research Council (EPSRC, EP/L015862/1, EP/533581/1), STFC Batteries Network (ST/R006873/1), RSC Mobility Grant (M19-7656), and Faraday Institution (EP/S003053/1) Degradation project (FIRG001) for financial support.

## Conflict of Interest

The authors declare no conflict of interest.



## Keywords

commercialization, flexible devices, lab-scale, polymer electrolytes, Zn-ion batteries

Received: November 4, 2020  
Revised: December 19, 2020  
Published online: April 2, 2021

- [1] G. H. Lee, H. Moon, H. Kim, G. H. Lee, W. Kwon, S. Yoo, D. Myung, S. H. Yun, Z. Bao, S. K. Hahn, *Nat. Rev. Mater.* **2020**, *5*, 149.
- [2] H. Huang, L. Han, J. Li, X. Fu, Y. Wang, Z. Yang, X. Xu, L. Pan, M. Xu, *J. Mater. Chem. A* **2020**, *8*, 10291.
- [3] K. Myny, *Nat. Electron.* **2018**, *1*, 30.
- [4] A. Sumboja, J. Liu, W. G. Zheng, Y. Zong, H. Zhang, Z. Liu, *Chem. Soc. Rev.* **2018**, *47*, 5919.
- [5] D. Kundu, B. D. Adams, V. Duffort, S. H. Vajargah, L. F. Nazar, *Nat. Energy* **2016**, *1*, 16119.
- [6] J. Frith, *Lithium-Ion Batteries: The Incumbent Technology Platform for Coal Regions in Transition*, [https://ec.europa.eu/energy/sites/ener/files/documents/6.1\\_frith\\_energy\\_storage.pdf](https://ec.europa.eu/energy/sites/ener/files/documents/6.1_frith_energy_storage.pdf) (accessed: August 2020).
- [7] I. Wagner, Worldwide – lithium ion battery pack costs 2019 | Statista, <https://www.statista.com/statistics/883118/global-lithium-ion-battery-pack-costs/> (accessed: August 2020).
- [8] S. Huang, J. Zhu, J. Tian, Z. Niu, *Chem. – A Eur. J.* **2019**, *25*, 14480.
- [9] Y. Zeng, H. Zhang, P. Yu, X. Lu, Y. Tong, M. Yu, *Small* **2019**, *15*, 1804760.
- [10] J. Lu, Y. Li, J. Fu, K. Amine, C. Zhong, Z. Chen, W. Hu, T. Wu, *Adv. Energy Mater.* **2018**, *9*, 1802605.
- [11] K. Wu, J. Huang, J. Yi, X. Liu, Y. Liu, Y. Wang, J. Zhang, Y. Xia, *Adv. Energy Mater.* **2020**, *10*, 1903977.
- [12] N. Zhang, Y. Dong, M. Jia, X. Bian, Y. Wang, M. Qiu, J. Xu, Y. Liu, L. Jiao, F. Cheng, *ACS Energy Lett.* **2018**, *3*, 1366.
- [13] L. Ma, S. Chen, C. Long, X. Li, Y. Zhao, Z. Liu, Z. Huang, B. Dong, J. A. Zapien, C. Zhi, *Adv. Energy Mater.* **2019**, *9*, 1902446.
- [14] D. Kundu, P. Oberholzer, C. Glaros, A. Bouzid, E. Tervoort, A. Pasquarello, M. Niederberger, *Chem. Mater.* **2018**, *30*, 3874.
- [15] Z. Wu, C. Lu, Y. Wang, L. Zhang, L. Jiang, W. Tian, C. Cai, Q. Gu, Z. Sun, L. Hu, *Small* **2020**, *16*, 2000698.
- [16] Z. Wu, Y. Wang, L. Zhang, L. Jiang, W. Tian, C. Cai, J. Price, Q. Gu, L. Hu, *ACS Appl. Energy Mater.* **2020**, *3*, 3919.
- [17] C. Xu, B. Li, H. Du, F. Kang, *Angew. Chem., Int. Ed.* **2012**, *51*, 933.
- [18] C. Wei, C. Xu, B. Li, H. Du, F. Kang, *J. Phys. Chem. Solids* **2012**, *73*, 1487.
- [19] B. Zhang, Y. Liu, X. Wu, Y. Yang, Z. Chang, Z. Wen, Y. Wu, *Chem. Commun.* **2014**, *50*, 1209.
- [20] V. Soundharrajan, B. Sambandam, S. Kim, V. Mathew, J. Jo, S. Kim, J. Lee, S. Islam, K. Kim, Y. K. Sun, J. Kim, *ACS Energy Lett.* **2018**, *3*, 1998.
- [21] H. Zhang, J. Wang, Q. Liu, W. He, Z. Lai, X. Zhang, M. Yu, Y. Tong, X. Lu, *Energy Storage Mater.* **2019**, *21*, 154.
- [22] P. Hu, M. Yan, T. Zhu, X. Wang, X. Wei, J. Li, L. Zhou, Z. Li, L. Chen, L. Mai, *ACS Appl. Mater. Interfaces* **2017**, *9*, 42717.
- [23] L. Wang, K. W. Huang, J. Chen, J. Zheng, *Sci. Adv.* **2019**, *5*, eaax4279.
- [24] J. Li, K. McColl, X. Lu, S. Sathasivam, H. Dong, L. Kang, Z. Li, S. Zhao, A. G. Kafzas, R. Wang, D. J. L. Brett, P. R. Shearing, F. Corà, G. He, C. J. Carmalt, I. P. Parkin, *Adv. Energy Mater.* **2020**, *10*, 2000058.
- [25] F. Wan, L. Zhang, X. Dai, X. Wang, Z. Niu, J. Chen, *Nat. Commun.* **2018**, *9*, 1656.
- [26] K. Lu, B. Song, Y. Zhang, H. Ma, J. Zhang, *J. Mater. Chem. A* **2017**, *5*, 23628.
- [27] L. Zhang, L. Chen, X. Zhou, Z. Liu, *Sci. Rep.* **2015**, *5*, 18263.
- [28] Z. Jia, B. Wang, Y. Wang, *Mater. Chem. Phys.* **2015**, *149*, 601.
- [29] W. Sun, F. Wang, S. Hou, C. Yang, X. Fan, Z. Ma, T. Gao, F. Han, R. Hu, M. Zhu, C. Wang, *J. Am. Chem. Soc.* **2017**, *139*, 9775.
- [30] Y. Jiao, L. Kang, J. Berry-Gair, K. McColl, J. Li, H. Dong, H. Jiang, R. Wang, F. Cora, D. Brett, G. He, I. P. Parkin, *J. Mater. Chem. A* **2020**, *8*, 22075.
- [31] Q. Pang, C. Sun, Y. Yu, K. Zhao, Z. Zhang, P. M. Voyles, G. Chen, Y. Wei, X. Wang, *Adv. Energy Mater.* **2018**, *8*, 1800144.
- [32] L. Jiang, Z. Wu, Y. Wang, W. Tian, Z. Yi, C. Cai, Y. Jiang, L. Hu, *ACS Nano* **2019**, *13*, 10376.
- [33] H. Pan, Y. Shao, P. Yan, Y. Cheng, K. S. Han, Z. Nie, C. Wang, J. Yang, X. Li, P. Bhattacharya, K. T. Mueller, J. Liu, *Nat. Energy* **2016**, *1*, 16039.
- [34] Q. Zhao, W. Huang, Z. Luo, L. Liu, Y. Lu, Y. Li, L. Li, J. Hu, H. Ma, J. Chen, *Sci. Adv.* **2018**, *4*, eaao1761.
- [35] X. Zeng, J. Liu, J. Mao, J. Hao, Z. Wang, S. Zhou, C. D. Ling, Z. Guo, *Adv. Energy Mater.* **2020**, *10*, 1904163.
- [36] Z. Hou, X. Zhang, X. Li, Y. Zhu, J. Liang, Y. Qian, *J. Mater. Chem. A* **2017**, *5*, 730.
- [37] C. Zhang, J. Holoubek, X. Wu, A. Daniyar, L. Zhu, C. Chen, D. P. Leonard, I. A. Rodríguez-Pérez, J. X. Jiang, C. Fang, X. Ji, *Chem. Commun.* **2018**, *54*, 14097.
- [38] H. Li, C. Han, Y. Huang, Y. Huang, M. Zhu, Z. Pei, Q. Xue, Z. Wang, Z. Liu, Z. Tang, Y. Wang, F. Kang, B. Li, C. Zhi, *Energy Environ. Sci.* **2018**, *11*, 941.
- [39] Z. Zhao, J. Zhao, Z. Hu, J. Li, J. Li, Y. Zhang, C. Wang, G. Cui, *Energy Environ. Sci.* **2019**, *12*, 1938.
- [40] D. Chao, C. (Rose) Zhu, M. Song, P. Liang, X. Zhang, N. H. Tiep, H. Zhao, J. Wang, R. Wang, H. Zhang, H. J. Fan, *Adv. Mater.* **2018**, *30*, 1803181.
- [41] Y. Zeng, X. Zhang, Y. Meng, M. Yu, J. Yi, Y. Wu, X. Lu, Y. Tong, *Adv. Mater.* **2017**, *29*, 1700274.
- [42] L. Ma, S. Chen, H. Li, Z. Ruan, Z. Tang, Z. Liu, Z. Wang, Y. Huang, Z. Pei, J. A. Zapien, C. Zhi, *Energy Environ. Sci.* **2018**, *11*, 2521.
- [43] F. Mo, G. Liang, Q. Meng, Z. Liu, H. Li, J. Fan, C. Zhi, *Energy Environ. Sci.* **2019**, *12*, 706.
- [44] J. Zhao, K. K. Sonigara, J. Li, J. Zhang, B. Chen, J. Zhang, S. S. Soni, X. Zhou, G. Cui, L. Chen, *Angew. Chem., Int. Ed.* **2017**, *56*, 7871.
- [45] F. Mo, H. Li, Z. Pei, G. Liang, L. Ma, Q. Yang, D. Wang, Y. Huang, C. Zhi, *Sci. Bull.* **2018**, *63*, 1077.
- [46] Q. Han, X. Chi, S. Zhang, Y. Liu, B. Zhou, J. Yang, Y. Liu, *J. Mater. Chem. A* **2018**, *6*, 23046.
- [47] S. Zhang, N. Yu, S. Zeng, S. Zhou, M. Chen, J. Di, Q. Li, *J. Mater. Chem. A* **2018**, *6*, 12237.
- [48] Y. Huang, J. Zhang, J. Liu, Z. Li, S. Jin, Z. Li, S. Zhang, H. Zhou, *Mater. Today Energy* **2019**, *14*, 100349.
- [49] Z. Liu, D. Wang, Z. Tang, G. Liang, Q. Yang, H. Li, L. Ma, F. Mo, C. Zhi, *Energy Storage Mater.* **2019**, *23*, 636.
- [50] Y. Ma, X. Xie, R. Lv, B. Na, J. Ouyang, H. Liu, *ACS Sustainable Chem. Eng.* **2018**, *6*, 8697.
- [51] Y. Huang, J. Liu, J. Zhang, S. Jin, Y. Jiang, S. Zhang, Z. Li, C. Zhi, G. Du, H. Zhou, *RSC Adv.* **2019**, *9*, 16313.
- [52] G. G. Kumar, S. Sampath, *Solid State Ionics* **2003**, *160*, 289.
- [53] G. G. Kumar, S. Sampath, *J. Electrochem. Soc.* **2003**, *150*, A608.
- [54] I. Pucić, A. Turković, *Solid State Ionics* **2005**, *176*, 1797.
- [55] A. Turković, M. Pavlović, P. Dubček, M. Lučić-Lavčević, B. Etlinger, S. Bernstorff, *J. Electrochem. Soc.* **2007**, *154*, A554.
- [56] N. Zhang, F. Cheng, J. Liu, L. Wang, X. Long, X. Liu, F. Li, J. Chen, *Nat. Commun.* **2017**, *8*, 405.
- [57] C. Xu, S. W. Chiang, J. Ma, F. Kang, *J. Electrochem. Soc.* **2013**, *160*, A93.
- [58] G. Girish Kumar, S. Sampath, *Polymer* **2004**, *45*, 2889.
- [59] M. Z. A. Munshi, *Adv. Mater.* **1996**, *8*, 866.
- [60] W. H. Meyer, *Adv. Mater.* **1998**, *10*, 439.
- [61] O. Borodin, G. D. Smith, *Macromolecules* **2006**, *39*, 1620.

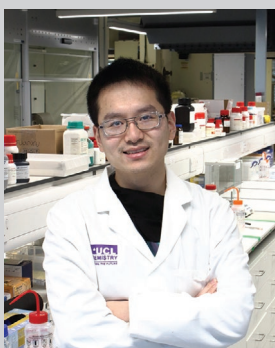
- [62] Z. Gadjourova, Y. G. Andreev, D. P. Tunstall, P. G. Bruce, *Nature* **2001**, 412, 520.
- [63] W. A. Henderson, N. R. Brooks, V. G. Young, *J. Am. Chem. Soc.* **2003**, 125, 12098.
- [64] R. C. Agrawal, G. P. Pandey, *J. Phys. D. Appl. Phys.* **2008**, 41, 223001.
- [65] M. A. Ratner, P. Johansson, D. F. Shriver, *MRS Bull.* **2000**, 25, 31.
- [66] E. Quartarone, P. Mustarelli, *Chem. Soc. Rev.* **2011**, 40, 2525.
- [67] M. Zhang, S. Yu, Y. Mai, S. Zhang, Y. Zhou, *Chem. Commun.* **2019**, 55, 6715.
- [68] A. F. Fuzlin, Y. Nagao, I. I. Misnon, A. S. Samsudin, *Ionics* **2020**, 26, 1923.
- [69] K. B. Girma, V. Lorenz, S. Blaurock, F. T. Edelmann, *Coord. Chem. Rev.* **2005**, 249, 1283.
- [70] B. Xiong, R. D. Loss, D. Shields, T. Pawlik, R. Hochreiter, A. L. Zydney, M. Kumar, *npj Clean Water* **2018**, 1, 17.
- [71] L. Long, S. Wang, M. Xiao, Y. Meng, *J. Mater. Chem. A* **2016**, 4, 10038.
- [72] W. P. Hagan, R. J. Latham, R. G. Linford, S. L. Vickers, *Solid State Ionics* **1994**, 70-71, 666.
- [73] L. Ma, S. Chen, N. Li, Z. Liu, Z. Tang, J. A. Zapien, S. Chen, J. Fan, C. Zhi, *Adv. Mater.* **2020**, 32, 1908121.
- [74] H. Qian, E. S. Greenhalgh, M. S. P. Shaffer, A. Bismarck, *J. Mater. Chem.* **2010**, 20, 4751.
- [75] M. Tako, *Adv. Biosci. Biotechnol.* **2015**, 6, 22.
- [76] Y. Cao, R. Mezzenga, *N. Food* **2020**, 1, 106.
- [77] D. F. S. Petri, *J. Appl. Polym. Sci.* **2015**, 132, 42035.
- [78] M. Iijima, M. Shinozaki, T. Hatakeyama, M. Takahashi, H. Hatakeyama, *Carbohydr. Polym.* **2007**, 68, 701.
- [79] Z. H. Mohammed, A. Haque, R. K. Richardson, E. R. Morris, *Carbohydr. Polym.* **2007**, 70, 38.
- [80] H. Glatz, E. Lizundia, F. Pacifico, D. Kundu, *ACS Appl. Energy Mater.* **2019**, 2, 1288.
- [81] S. S. Jeong, N. Böckenfeld, A. Balducci, M. Winter, S. Passerini, *J. Power Sources* **2012**, 199, 331.
- [82] Y. Li, Q. Zeng, I. R. Gentle, D. W. Wang, *J. Mater. Chem. A* **2017**, 5, 5460.
- [83] Q. Zhang, C. Li, Q. Li, Z. Pan, J. Sun, Z. Zhou, B. He, P. Man, L. Xie, L. Kang, X. Wang, J. Yang, T. Zhang, P. P. Shum, Q. Li, Y. Yao, L. Wei, *Nano Lett.* **2019**, 19, 4035.
- [84] Y. Lin, J. Li, K. Liu, Y. Liu, J. Liu, X. Wang, *Green Chem.* **2016**, 18, 3796.
- [85] H. Li, Q. Yang, F. Mo, G. Liang, Z. Liu, Z. Tang, L. Ma, J. Liu, Z. Shi, C. Zhi, *Energy Storage Mater.* **2019**, 19, 94.
- [86] K. Deshmukh, M. B. Ahamed, R. R. Deshmukh, S. K. K. Pasha, P. R. Bhagat, in *Biopolymer Composites Electronics.*, Elsevier, New York **2017**, pp. 27–128.
- [87] J. Zhao, H. Ren, Q. Liang, D. Yuan, S. Xi, C. Wu, W. Manalastas, J. Ma, W. Fang, Y. Zheng, C. F. Du, M. Srinivasan, Q. Yan, *Nano Energy* **2019**, 62, 94.
- [88] W. Kong, T. Li, C. Chen, G. Chen, A. H. Brozena, D. Liu, Y. Liu, C. Wang, W. Gan, S. Wang, S. He, L. Hu, *Chem. Mater.* **2019**, 31, 9288.
- [89] W. Kong, T. Li, C. Chen, G. Chen, A. H. Brozena, D. Liu, Z. Li, Y. Liu, C. Wang, W. Gan, S. Wang, S. He, L. Hu, *Chem. Mater.* **2019**, 31, 9288.
- [90] Z. Liu, Q. Yang, D. Wang, G. Liang, Y. Zhu, F. Mo, Z. Huang, X. Li, L. Ma, T. Tang, Z. Lu, C. Zhi, *Adv. Energy Mater.* **2019**, 9, 1902473.
- [91] D. Wang, L. Wang, G. Liang, H. Li, Z. Liu, Z. Tang, J. Liang, C. Zhi, *ACS Nano* **2019**, 13, 10643.
- [92] A. A. Mohamad, N. S. Mohamed, M. Z. A. Yahya, R. Othman, S. Ramesh, Y. Alias, A. K. Arof, *Solid State Ionics* **2003**, 156, 171.
- [93] J. Vatsalarani, N. Kalaiselvi, R. Karthikeyan, *Ionics* **2009**, 15, 97.
- [94] M. Yu, Y. Zeng, X. Zhang, Y. Wu, X. Lu, J. Yi, Y. Tong, Y. Meng, *Adv. Mater.* **2017**, 29, 1700274.
- [95] Z. Pei, Z. Yuan, C. Wang, S. Zhao, J. Fei, L. Wei, J. Chen, C. Wang, R. Qi, Z. Liu, Y. Chen, *Angew. Chem., Int. Ed.* **2020**, 59, 4793.
- [96] W. Lao-atiman, T. Julaphatachote, P. Boonmongkolras, S. Kheawhom, *J. Electrochem. Soc.* **2017**, 164, A859.
- [97] X. Zhu, H. Yang, Y. Cao, X. Ai, *Electrochim. Acta* **2004**, 49, 2533.
- [98] A. M. Gaikwad, G. L. Whiting, D. A. Steingart, A. C. Arias, *Adv. Mater.* **2011**, 23, 3251.
- [99] J. Liu, M. Hu, J. Wang, N. Nie, Y. Wang, Y. Wang, J. Zhang, Y. Huang, *Nano Energy* **2019**, 58, 338.
- [100] Y. Tang, X. Li, H. Lv, D. Xie, W. Wang, C. Zhi, H. Li, *Adv. Energy Mater.* **2020**, 10, 2000892.
- [101] F. Mo, Z. Chen, G. Liang, D. Wang, Y. Zhao, H. Li, B. Dong, C. Zhi, *Adv. Energy Mater.* **2020**, 10, 2000035.
- [102] J. D. Delgado, J. B. Schlenoff, *Macromolecules* **2017**, 50, 4454.
- [103] K. Leng, G. Li, J. Guo, X. Zhang, A. Wang, X. Liu, J. Luo, *Adv. Funct. Mater.* **2020**, 30, 2001317.
- [104] D. K. Nandakumar, S. K. Ravi, Y. Zhang, N. Guo, C. Zhang, S. C. Tan, *Energy Environ. Sci.* **2018**, 11, 2179.
- [105] Xanthan gum Price Market Analysis - Echemi, <https://www.echemi.com/productsInformation/pd20150901009-xanthan-gum.html> (accessed: November 2020).
- [106] Marketsandmarkets (2017), Xanthan Gum Market Growth Industrial Analysis Report: Xanthan Gum Market by Application (Food & Beverages, Oil & Gas, Pharmaceuticals), Function (Thickeners, Stabilizers, Gelling Agents, Fat Replacers, Coating Materials), Form (Dry, Liquid), and Region - Global Forecast to 2022. Press release (Feb. 2017).
- [107] Marketsandmarkets (2017), Guar Gum Market Growth Industrial Analysis Report: Guar Gum Market by Function (Thickening, Gelling, Binding, Friction Reducing), Application (Food & Beverages, Oil & Gas, Paper Manufacturing, Mining & Explosives, Pharmaceuticals & Cosmetics), Grade, and Region - Global Forecast to 2022. Press release (Jun. 2017).
- [108] Marketsandmarkets (2019), Gelatin Market Growth Industrial Analysis Report: Gelatin Market by Source (Porcine, Bovine Skin, Bovine Bone, Fish & Poultry), Application (Food, Pharmaceuticals & Healthcare), Type (Type A, Type B), Function (Stabilizing, Thickening, Gelling), and Region - Global Forecast to 2023. Press release (Feb. 2019).
- [109] Grand View Research (2020), Alginate Market Size Worth \$1.02 Billion By 2027 | CAGR: 4.7%. Press release (Sep. 2020).
- [110] Grand View Research (2017), Agar Agar Gum Market Size, Share, Global Industry Report, 2018–2025. Press release (Apr. 2017).
- [111] Market Data Forecast (2020), Carrageenan Market Growth and Forecast 2020–2025. Press release (Feb. 2020).
- [112] Research And Markets (2020), Sodium Carboxymethyl Cellulose Market - Forecast (2020–2025). Press release (Mar. 2020).
- [113] Grand View Research (2020), Chitosan Market Size Global Industry Analysis Report 2020–2027. Press release (Mar. 2020).
- [114] A. A. Mariod, *Functional Properties of Gum Arabic*, Elsevier, New York **2018**.
- [115] Wordpress (2018), Sudanese Gum Arabic Market. Press release (14 May 2018).
- [116] Grand View Research (2019), Gum Arabic Market Size & Share Industry Analysis Report 2019–2025. Press release (Aug. 2019).
- [117] Persistence Market Research (2018), Global Karaya Gum Market Research Report. Press release (16 Jan. 2018).
- [118] Marketsandmarkets (2016), Starch Market Research Report: Industrial Starch Market by Type (Native, Starch Derivatives & Sweeteners), Source (Corn, Wheat, Cassava, Potato), Application (Food, Feed, Paper Making & Corrugation, Pharmaceutical), Form (Dry, Liquid), and Region - Global Forecast to 2022. Press release (Nov. 2016).
- [119] J. H. Hamman, *Molecules* **2008**, 13, 1599.
- [120] Grand view research (2019), Global Aloe Vera Extract Market Size Report 2019–2025. Press release (May 2019).
- [121] Marketsandmarkets (2016), Polyacrylamide Market Research Report: Polyacrylamide Market by Type (Anionic, Cationic,

- Non-Ionic), Application (Water Treatment, Pulp & Paper, Enhanced Oil Recovery, Mineral Processing), Region - Global Forecast to 2021. Press release (Nov. 2016).
- [122] Polyacrylamide (PAM) Price Market Analysis - Echemi, <https://www.echemi.com/productsInformation/pd20150901064-polyacrylamide.html> (accessed: December 2020).
- [123] 360 Research Reports (2020), Polyacrylic Acid Market Report 2020: Rising Impressive Business Opportunities Analysis with Top Countries Data Forecast By 2026. Press release (29 Nov. 2020).
- [124] Polyvinyl Alcohol (PVA) Price Market Analysis - Echemi, <https://www.echemi.com/productsInformation/pd20150901224-polyvinylalcohol.html> (accessed: December 2020).
- [125] 360 Research Reports (2020), Global Polyethylene Oxide (PEO) Market 2020–2026. Press release (7 Sep. 2020).
- [126] Polaris Market Research (2018), Polyacrylate Market Research Report: Polyacrylate Market Share, Size, Trends, Industry Analysis Report By Product Type (Poly-Methyl Acrylate, Poly-Ethyl Acrylate, Poly-Butyl Acrylate and Others); By Application (Paints & Coatings, Adhesives & Sealants, Textiles, Paper & Paperboard, and Others); By Regions, Segments & Forecast, 2018–2026. Press release (Oct. 2018).
- [127] S. S. Soni, K. B. Fadadu, A. Gibaud, *Langmuir* **2012**, *28*, 751.
- [128] X. Yan, Q. Chen, L. Zhu, H. Chen, D. Wei, F. Chen, Z. Tang, J. Yang, J. Zheng, *J. Mater. Chem. B* **2017**, *5*, 7683.
- [129] J. Zhu, M. Yao, S. Huang, J. Tian, Z. Niu, *Angew. Chem., Int. Ed.* **2020**, *59*, 16480.
- [130] Y. Zhang, Z. Chen, H. Qiu, W. Yang, Z. Zhao, J. Zhao, G. Cui, *NPG Asia Mater* **2020**, *12*, 4.
- [131] Z. Wang, Z. Wu, N. Bramnik, S. Mitra, *Adv. Mater.* **2014**, *26*, 970.
- [132] G. M. Wu, S. J. Lin, C. C. Yang, *J. Memb. Sci.* **2006**, *275*, 127.
- [133] M. Chen, W. Zhou, A. Wang, A. Huang, J. Chen, J. Xu, C. P. Wong, *J. Mater. Chem. A* **2020**, *8*, 6828.
- [134] W. Zhou, J. Chen, M. Chen, A. Wang, A. Huang, X. Xu, J. Xu, C. P. Wong, *J. Mater. Chem. A* **2020**, *8*, 8397.
- [135] Z. Liu, Y. Huang, Y. Huang, Q. Yang, X. Li, Z. Huang, C. Zhi, *Chem. Soc. Rev.* **2020**, *49*, 180.
- [136] B. Tang, L. Shan, S. Liang, J. Zhou, *Energy Environ. Sci.* **2019**, *12*, 3288.
- [137] S. Guo, L. Qin, T. Zhang, M. Zhou, J. Zhou, G. Fang, S. Liang, *Energy Storage Mater.* **2021**, *34*, 545.
- [138] S. P. Candhadai Murali, A. S. Samuel, *J. Appl. Polym. Sci.* **2019**, *136*, 47654.
- [139] L. Han, H. Huang, J. Li, X. Zhang, Z. Yang, M. Xu, L. Pan, *J. Mater. Chem. A* **2020**, *8*, 15042.
- [140] X. Guo, J. Zhou, C. Bai, X. Li, G. Fang, S. Liang, *Mater. Today Energy* **2020**, *16*, 100396.
- [141] N. Li, G. Li, C. Li, H. Yang, G. Qin, X. Sun, F. Li, H. M. Cheng, *ACS Appl. Mater. Interfaces* **2020**, *12*, 13790.
- [142] H. I. Kim, H. C. Shin, *J. Alloys Compd.* **2015**, *645*, 7.
- [143] H. Li, Z. Liu, G. Liang, Y. Huang, Y. Huang, M. Zhu, Z. Pei, Q. Xue, Z. Tang, Y. Wang, B. Li, C. Zhi, *ACS Nano* **2018**, *12*, 3140.
- [144] Y. Huang, W. S. Ip, Y. Y. Lau, J. Sun, J. Zeng, N. S. S. Yeung, W. S. Ng, H. Li, Z. Pei, Q. Xue, Y. Wang, J. Yu, H. Hu, C. Zhi, *ACS Nano* **2017**, *11*, 8953.
- [145] M. Li, J. Meng, Q. Li, M. Huang, X. Liu, K. A. Owusu, Z. Liu, L. Mai, *Adv. Funct. Mater.* **2018**, *28*, 1802016.
- [146] Y. Liu, M. Pharr, G. A. Salvatore, *ACS Nano* **2017**, *11*, 9614.
- [147] Y. Zhao, J. Guo, *InfoMat* **2020**, *2*, 866.
- [148] L. E. Asp, E. S. Greenhalgh, *Compos. Sci. Technol.* **2014**, *101*, 41.
- [149] International Data Corporation (2020), Market share of wearables unit shipments worldwide by vendor from 1Q 2014 to 3Q 2020. Press release (Dec. 2020).
- [150] J. J. Richardson, J. Cui, M. Björnalm, J. A. Braunger, H. Ejima, F. Caruso, *Chem. Rev.* **2016**, *116*, 14828.
- [151] X. Wang, S. Zheng, F. Zhou, J. Qin, X. Shi, S. Wang, C. Sun, X. Bao, Z. S. Wu, *Natl. Sci. Rev.* **2020**, *7*, 64.
- [152] D. Bender, J. Schuster, D. Heider, *Compos. Sci. Technol.* **2006**, *66*, 2265.
- [153] N. Shirshova, A. Bismarck, S. Carreyette, Q. P. V. Fontana, E. S. Greenhalgh, P. Jacobsson, P. Johansson, M. J. Marczewski, G. Kalinka, A. R. J. Kucernak, J. Scheers, M. S. P. Shaffer, J. H. G. Steinke, M. Wienrich, *J. Mater. Chem. A* **2013**, *1*, 15300.
- [154] K. Sun, T. S. Wei, B. Y. Ahn, J. Y. Seo, S. J. Dillon, J. A. Lewis, *Adv. Mater.* **2013**, *25*, 4539.
- [155] D. W. McOwen, S. Xu, Y. Gong, Y. Wen, G. L. Godbey, J. E. Gritton, T. R. Hamann, J. Dai, G. T. Hitz, L. Hu, E. D. Wachsman, *Adv. Mater.* **2018**, *30*, 1707132.
- [156] L. J. Deiner, T. L. Reitz, *Adv. Eng. Mater.* **2017**, *19*, 1600878.
- [157] C. C. Ho, K. Murata, D. a Steingart, J. W. Evans, P. K. Wright, *J. Micromech. Microeng.* **2008**, *19*, 094013.
- [158] M. Hilder, B. Winther-Jensen, N. B. Clark, *J. Power Sources* **2009**, *194*, 1135.
- [159] H. L. Liang, M. M. Bay, R. Vadrucchi, C. H. Barty-King, J. Peng, J. J. Baumberg, M. F. L. De Volder, S. Vignolini, *Nat. Commun.* **2018**, *9*, 4632.
- [160] W. Qiu, Y. Li, A. You, Z. Zhang, G. Li, X. Lu, Y. Tong, *J. Mater. Chem. A* **2017**, *5*, 14838.
- [161] K. Wang, X. Zhang, J. Han, X. Zhang, X. Sun, C. Li, W. Liu, Q. Li, Y. Ma, *ACS Appl. Mater. Interfaces* **2018**, *10*, 24573.
- [162] X. Dai, F. Wan, L. Zhang, H. Cao, Z. Niu, *Energy Storage Mater.* **2019**, *17*, 143.
- [163] H. Dong, J. Li, S. Zhao, F. Zhao, S. Xiong, D. J. L. Brett, G. He, I. P. Parkin, *J. Mater. Chem. A* **2020**, *8*, 22637.
- [164] F. Wang, O. Borodin, T. Gao, X. Fan, W. Sun, F. Han, A. Faraone, J. A. Dura, K. Xu, C. Wang, *Nat. Mater.* **2018**, *17*, 543.
- [165] C. W. Lee, K. Sathiyarayanan, S. W. Eom, H. S. Kim, M. S. Yun, *J. Power Sources* **2006**, *159*, 1474.
- [166] L. Cao, D. Li, T. Deng, Q. Li, C. Wang, *Angew. Chem., Int. Ed.* **2020**, *59*, 19292.
- [167] C. Zhong, B. Liu, J. Ding, X. Liu, Y. Zhong, Y. Li, C. Sun, X. Han, Y. Deng, N. Zhao, W. Hu, *Nat. Energy* **2020**, *5*, 440.
- [168] G. G. Yadav, D. Turney, J. Huang, X. Wei, S. Banerjee, *ACS Energy Lett.* **2019**, *4*, 2144.
- [169] D. Chao, W. Zhou, C. Ye, Q. Zhang, Y. Chen, L. Gu, K. Davey, S. Z. Qiao, *Angew. Chem., Int. Ed.* **2019**, *58*, 7823.
- [170] W. Fan, F. Liu, Y. Liu, Z. Wu, L. Wang, Y. Zhang, Q. Huang, L. Fu, Y. Wu, *Chem. Commun.* **2020**, *56*, 2039.
- [171] P. Peljo, H. H. Girault, *Energy Environ. Sci.* **2018**, *11*, 2306.
- [172] T. Zhang, Y. Tang, G. Fang, C. Zhang, H. Zhang, X. Guo, X. Cao, J. Zhou, A. Pan, S. Liang, *Adv. Funct. Mater.* **2020**, *30*, 2002711.
- [173] D. Kundu, S. Hosseini Vajargah, L. Wan, B. Adams, D. Prendergast, L. F. Nazar, *Energy Environ. Sci.* **2018**, *11*, 881.
- [174] T. Zhang, Y. Tang, S. Guo, X. Cao, A. Pan, G. Fang, J. Zhou, S. Liang, *Energy Environ. Sci.* **2020**, *13*, 4625.
- [175] Z. Yi, G. Chen, F. Hou, L. Wang, J. Liang, *Adv. Energy Mater.* **2020**, 2003065.
- [176] W. Du, E. H. Ang, Y. Yang, Y. Zhang, M. Ye, C. C. Li, *Energy Environ. Sci.* **2020**, *13*, 3330.
- [177] J. Cao, D. Zhang, X. Zhang, M. Sawangphruk, J. Qin, R. Liu, *J. Mater. Chem. A* **2020**, *8*, 9331.
- [178] B. S. Lee, S. Cui, X. Xing, H. Liu, X. Yue, V. Petrova, H. D. Lim, R. Chen, P. Liu, *ACS Appl. Mater. Interfaces* **2018**, *10*, 38928.
- [179] A. Nazarov, T. Prosek, D. Thierry, *Electrochim. Acta* **2008**, *53*, 7531.
- [180] Y. Huang, M. Zhong, F. Shi, X. Liu, Z. Tang, Y. Wang, Y. Huang, H. Hou, X. Xie, C. Zhi, *Angew. Chem., Int. Ed.* **2017**, *56*, 9141.
- [181] L. Mao, Q. Meng, A. Ahmad, Z. Wei, *Adv. Energy Mater.* **2017**, *7*, 1700535.

- [182] Z. Li, D. Chen, Y. An, C. Chen, L. Wu, Z. Chen, Y. Sun, X. Zhang, *Energy Storage Mater.* **2020**, *28*, 307.
- [183] L. Han, L. Yan, K. Wang, L. Fang, H. Zhang, Y. Tang, Y. Ding, L. T. Weng, J. Xu, J. Weng, Y. Liu, F. Ren, X. Lu, *NPG Asia Mater.* **2017**, *9*, e372.
- [184] A. Drach, B. Drach, I. Tsukrov, *Adv. Eng. Software* **2014**, *72*, 18.
- [185] S. Sharma, A. Anand, A. Shukla, A. Sharma, in *Zinc Batteries*, Wiley, New York **2020**, pp. 131.
- [186] L. Zhan, O. Li, Z. Wang, B. Xie, *ACS Sustainable Chem. Eng.* **2018**, *6*, 12104.
- [187] R. Farzana, K. Hassan, V. Sahajwalla, *Sci. Rep.* **2019**, *9*, 8982.



**Haobo Dong** received his M.Eng. degree in aeronautical engineering from Imperial College London, UK. He is now working toward his Ph.D. degree at University College London (UCL) under the supervision of Prof. Ivan P. Parkin and Dr. Guanjie He. His current research focuses on the investigations of flexible zinc ion batteries and its mechanism.



**Guanjie He** is a Senior Lecturer in Chemistry and Programme Leader for M.Sc. Battery Sciences, University of Lincoln, and an Honorary Lecturer at University College London (UCL). He received his Ph.D. degree from the Chemistry Department, UCL, under the supervision of Prof. Ivan P. Parkin. His research focuses on materials for electrochemical energy storage and conversion applications, especially electrode materials in aqueous electrolyte systems.



**Ivan P. Parkin** is a Professor of Materials Chemistry, Dean of Faculty of Maths and Physical Sciences at University College London. He is a selected Fellow of Royal Society of Chemistry and a member of Academia Europaea. His work focuses on the development of functional inorganic materials and thin films for energy storage application, photocatalysis and wetting.